

University of Alberta

Tapered air-core Bragg waveguide spectrometers for fluorescence detection in
lab-on-a-chip devices

by

Brian Andrew Drobot

A thesis submitted to the Faculty of Graduate Studies and Research
in partial fulfillment of requirements for degree of

Master of Science

in

Microsystems and Nanodevices

Department of Electrical and Computer Engineering

© Brian Andrew Drobot

Spring 2014

Edmonton, Alberta

Permission is hereby granted to the University of Alberta Libraries to reproduce single copies of this thesis and to lend or sell such copies for private, scholarly or scientific research purposes only. Where the thesis is converted to, or otherwise made available in digital form, the University of Alberta will advise potential users of the thesis of these terms.

The author reserves all other publication and other rights in association with the copyright in the thesis and, except as herein before provided, neither the thesis nor any substantial portion thereof may be printed or otherwise reproduced in any material form whatsoever without the author's prior written permission.

Abstract

This thesis describes a study on tapered air-core Bragg waveguides for use as integrated micro-spectrometers in lab-on-a-chip systems. Position-dependent cutoff of the leaky waveguide modes results in spatial dispersion of polychromatic input light. These devices may be viewed as side-coupled Fabry-Perot cavities of varying core thickness. Chip-scale spectrometers have a number of applications, including point-of-care diagnostics, biochemistry, and field-deployable threat detectors.

Bragg cladding mirrors with an omnidirectional band (for TE-polarized light) between ~ 490 nm and ~ 570 nm were deposited using both e-beam evaporation and reactive sputtering. Using these claddings, tapered hollow Bragg waveguides were assembled using two different methods: buckling self-assembly and a wafer-bonding process. The tapers exhibited resolutions ranging from ~ 2.2 nm to ~ 0.8 nm, for mode orders $m = 1$ to $m = 8$. Implementing the tapers in a prototype sensing system, the fluorescence spectra of individual fluorescent beads were successfully measured over the ~ 70 nm wide operating range of the device.

Acknowledgements

I would first like to thank my supervisor, Dr. Ray DeCorby, for his advice and support throughout my thesis. His constant guidance, which started back when I was an undergraduate summer student in his lab, has helped me to develop the skills and attributes necessary for professional success.

To all the members of our lab group, you have been great to work with. Thanks to Aaron Melnyk for fabricating the tapered waveguide chips with me. Those countless hours spent in the nanoFAB and CCIS went by a lot faster with your help. Thanks to Dr. Trevor Allen for helping with experiments and for giving helpful insight. I also extend thanks to Carson Zhang, Min Choi, and Clinton Potts.

My work would not have been possible without the support and hard work of all of the nanoFAB staff. Special thanks to Scott Munro and Les Schowalter, not only for training me on a variety of tools, but also for important discussions that helped my research to succeed.

I would be remiss not to mention the unwavering support I have received from my parents, family and friends throughout my thesis. They have displayed the utmost of patience, especially with the unusual hours I kept while writing.

This research was supported financially by the Natural Sciences and Engineering Research Council (NSERC), Alberta Innovates Technology Futures (AITF), and the University of Alberta.

Table of Contents

1	Introduction	1
1.1	Optofluidic lab-on-a-chip devices	1
1.2	Fluorescence spectroscopy in LOC devices	3
1.3	Integrated hollow waveguides	4
1.4	Applications of tapered Bragg waveguides	8
1.4.1	Linear variable filter-based micro-spectrometers	8
1.4.2	Photonic integrated circuit components	10
1.4.3	Tunable organic microcavity lasers	11
1.5	Summary of thesis	11
1.6	Works Cited.....	13
2	Theory.....	16
2.1	Introduction	16
2.2	Omnidirectional Bragg reflector waveguides	16
2.2.1	Leaky dielectric waveguides	16
2.2.2	Bragg reflectors	18
2.2.3	Omnidirectional Bragg reflectors	20
2.3	Tapered Bragg waveguides.....	21
2.3.1	Vertical Fabry-Perot cavity model	23
2.3.2	Effective-index transfer matrix model	24
2.4	Delamination buckles	27
2.5	Fluorescence	28
2.6	Works Cited.....	30

3	Fabrication of tapered hollow Bragg waveguides	32
3.1	Introduction	32
3.2	Electron beam evaporation of TiO ₂ /SiO ₂ Bragg mirrors.....	33
3.3	Sputter deposition of TiO ₂ /SiO ₂ Bragg Mirrors.....	37
3.4	Hollow waveguides formed by controlled buckling of TiO ₂ /SiO ₂ Bragg mirrors	43
3.5	Air-core slab Bragg waveguide tapers fabricated by wafer bonding	48
3.6	Conclusions	52
3.7	Works Cited.....	53
4	Integration of tapers with microfluidics	55
4.1	Introduction	55
4.2	PDMS microfluidics integrated on-chip with buckled waveguides	55
4.3	Microfluidic integration for slab waveguide tapers	61
4.3.1	PDMS reservoirs	61
4.3.2	Glass capillaries	63
4.3.3	Integrated platform for fluid insertion into taper	65
4.4	Conclusions	67
4.5	Works Cited.....	67
5	Visible band taper spectrometer	69
5.1	Introduction	69
5.2	Device concept and design	70
5.3	Taper Dispersion and Wavelength Resolution	74
5.4	Taper operating range	80
5.5	Conclusions	89

5.6 Works Cited.....	90
6 Fluorescence Experiments	92
6.1 Introduction	92
6.2 LVF fluorescence experiments.....	92
6.2.1 Fluorescence from a glass capillary.....	93
6.3.2 Fluorescence from a thin film of microspheres in solution	96
6.3 Waveguide coupled spectrometer	97
6.3.1 Fluorescence coupled from a glass capillary.....	98
6.3.2 Fluorescent microsphere insertion into taper cavity.....	105
6.4 Conclusions	113
6.5 Works Cited.....	114
7 Conclusions	115
7.1 Summary	115
7.1.1 Fabrication process for tapered air-core waveguides	115
7.1.2 Tapered air-core waveguide spectrometers for lab-on-a-chip devices.....	117
7.2 Future work	118
7.2.1 Improvements in operating range and taper fabrication processes	118
7.2.2 Fluorescence experiments	119
7.3 Works cited	120
Appendix A: MATLAB code	121
Appendix B: Electron beam evaporator procedure.....	134
Appendix C: Sputter System Procedure.....	137

List of Tables

3.1	Deposition parameters for TiO ₂ /SiO ₂ Bragg mirrors deposited in the e-beam evaporator.	35
3.2	Compressive stress and deposition rate of TiO ₂ monolayer, for different deposition parameters. Stress was measured using a Flexus film stress measurement system.	40
3.3	Deposition parameters for TiO ₂ /SiO ₂ Bragg mirrors deposited by reactive sputtering.....	40
3.4	Deposition parameters of fluorocarbon deposition recipe for an ICP-RIE tool. A slightly modified recipe for the passivation cycle of a Bosch recipe is used.	46
3.5	Recipe for patterning SU-8 posts of 5.9 μm and 2.1 μm height. The parameters work for a substrate with a TiO ₂ top layer. Posts with 2.1 μm height require longer bake times to improve adhesion and a hard bake to repair cracking due to extended bake times.	49
6.1	Fluorescein equivalents for yellow-green FluoSpheres of different sizes. Adapted from Ref. [1].	99

List of Figures

1.1	Experimental setup of a fluorescence detection system in PDMS. Adapted from Ref. [11].	2
1.2	Example of a chip-scale spectrometer used to measure the fluorescence spectrum of an analyte. Adapted from Ref. [12].	3
1.3	An example of a LOC for fluorescence detection, using an arrayed waveguide grating (AWG). Adapted from Ref. [13].	4
1.4	Liquid core waveguides using refractive index guiding. (a) Teflon AF cladding, (b) Air nano-pore cladding, (c) Liquid cladding, (d) Slot waveguide. Adapted from Ref. [14].	5
1.5	Example of an ARROW LOC device. Adapted from Ref. [15].	6
1.6	Schematic showing the process to fabricate hollow channel waveguides. Adapted from Ref. [16].	7
1.7	Example of a tapered Fabry-Perot cavity LVF. Adapted from Ref. [19].	9
1.8	Schematic of potential application of a hollow tapered waveguide as a multiplexer/demultiplexer. Adapted from Ref. [22].	10
1.9	Schematic of a wedge-shaped microcavity used in a tunable organic laser. Adapted from Ref. [23].	11
2.1	A schematic illustration of loss (due to material absorption) and leakage (due to imperfect mirrors) of a guided mode in a leaky waveguide.	17
2.2	Schematic of an air-core slab waveguide with periodic semi-infinite claddings (with refractive indices n_1 and n_2). The transverse field distribution of the fundamental mode is also shown. Adapted from Ref. [4].	18

2.3	A projected dispersion diagram showing the omnidirectional band gaps of a Bragg mirror. The Brewster angle is inaccessible by external plane waves. Adapted from Ref. [5].	20
2.4	Simulated mirror reflectance for a 5.5-period TiO ₂ /SiO ₂ mirror, with refractive indices of 2.42 and 1.50 for TiO ₂ and SiO ₂ , respectively. By relaxing the omnidirectional band to just TE-polarized light, an omnidirectional band of ~80 nm is achievable.	21
2.5	A ray-optics representation of light being guided in an air-core tapered Bragg waveguide. As light within the omnidirectional band of the cladding mirrors propagates towards the narrow end of the taper, it approaches cutoff, and is adiabatically transformed into a vertical cavity resonant mode. Adapted from Ref. [7].	22
2.6	A schematic illustration of the effective-index transfer matrix model. N_i is the complex modal effective index for corresponding mirror separation δ_i . Adapted from Ref. [7]	24
2.7	Simulation of radiated power of guided modes versus position, for a taper with a slope of 0.7 $\mu\text{m}/\text{mm}$ and TE-polarized light of mode order $m = 4$. Light reaches cutoff for wavelengths between ~500 nm and ~570 nm. Blue-cyan-green light is well-guided far fro cutoff, while orange-red light outside of the omnidirectional band is not well-guided in the taper.	25
2.8	Simulation of radiated power of guided modes versus position, for a taper with a slope of 2 $\mu\text{m}/\text{mm}$. The increased taper slope helps to increase the operating range, and also to even out the radiated power versus wavelength.	26
2.9	Geometry and buckling analysis of different types of buckles. Adapted from Ref. [9].	27
2.10	A Jablonski diagram, adapted from Ref. [10]	29

2.11	Absorption and emission spectra for yellow-green fluorescent microspheres (FluoSpheres, Invitrogen) [11].	30
3.1	Schematic of a typical electron beam evaporation system. A magnetic field guides an electron beam to a source material, which evaporates or sublimates upon heating. The material is deposited on the substrate above.....	33
3.2	Photo of control panel for e-beam evaporation system. (a) Ion gauge controller (KJL 4500), (b) deposition rate controllers (Sycon STM-100 and STC-2000A), (c) current sweep controller (MDC eVap Programmable X-Y sweep), (d) Voltage and current control.....	34
3.3	(a) Theoretical and experimental reflectance of evaporated TiO ₂ /SiO ₂ mirrors for TE-polarized light at a 20 degree incident angle. (b) Normal Incidence transmittance of the TiO ₂ /SiO ₂ mirrors. Data was fitted using a fixed +0.02 offset to the Kim dispersion formula [7] and layer thicknesses of 60 nm and 91.5 nm, resulting in refractive indices of ~2.33 and ~1.46 at 550 nm, for TiO ₂ and SiO ₂ , respectively.....	36
3.4	Schematic of a typical magnetron sputtering system. A co-sputtering configuration is shown, with substrate rotation. When a potential is applied, the substrate acts as the anode and the target acts as the cathode. Sputtered source material is deposited on the substrate.....	37
3.5	Image of control panel for sputtering system. (a) Pressure gauges (convectron, baratron, ion), (b) MKS mass flow controllers, (c) DC magnetron power supplies, (d) pulsed DC power supply.	39
3.6	(a) Theoretical and experimental reflectance of sputtered TiO ₂ /SiO ₂ mirrors for TE-polarized light at a 20 degree incident angle. (b) Normal incidence transmittance of the TiO ₂ /SiO ₂ mirrors. Data was fitted using a fixed +0.11 offset to the Kim dispersion formula [7] and layer thicknesses	

	of 59 nm and 90 nm, resulting in refractive indices of ~ 2.42 and ~ 1.50 at 550 nm, for TiO_2 and SiO_2 , respectively. Adapted from Ref. [11].	41
3.7	Refractive index of reactively sputtered SiO_2 compared to similarly deposited film in Ref. [2]. Data was extracted from VASE reflectance measurements of SiO_2 monolayer using a Cauchy fit.	42
3.8	Optical constants for reactively sputtered TiO_2 , determined by fitting R & T measurements of $\text{TiO}_2/\text{SiO}_2$ mirror. The transfer matrix simulation used the dispersion relation from Ref. [7] and a fixed +0.11 offset. (a) Refractive index of TiO_2 , compared to data from Ref. [2] (b) Extinction coefficient of TiO_2 compared to Ref. [2].	43
3.9	Process flow for buckling assembly of hollow Bragg waveguides. (a) Bragg reflector deposited on substrate, (b) fluorocarbon low adhesion layer deposited and patterned by liftoff, (c) second Bragg reflector deposited, (d) heating to induce buckling in lo-adhesion areas. Adapted from Ref. [1].	44
3.10	Image of patterned photoresist on Bragg mirror, defining locations for low-adhesion layer. Dome array and tapered waveguide patterns are visible.	45
3.11	Images of buckling results for $\text{TiO}_2/\text{SiO}_2$ hollow waveguides. (a)-(c) Partially buckled waveguides with thin layer of W on top to help increase compressive stress. Waveguides did not fully buckle and also broke off in some places. (d) Dome cavities either partially buckled or popped off completely.	47
3.12	Process flow for wafer-bonding assembly of air-core tapered slab Bragg waveguides. (a) Bragg mirror deposited on substrate, (b) SU-8 spun-cast and patterned onto mirror, (c) substrate diced along predefined lines, (d) a patterned and blank piece clamped and bonded with UV-curable epoxy.	49

3.13	(a) Schematic illustration of a tapered slab Bragg waveguide fabricated by bonding a glass substrate to a patterned Si substrate. (b) SEM image showing the end facet (wide end) of a taper. For scale reference, the spacing between adjacent SU-8 posts is 150 μm . Adapted from Ref. [5].	51
3.14	Images of manually assembled tapers with (a) glass and silicon substrates with mismatched length, (b) glass and silicon substrates with matched length, (c) quartz substrates with overhangs at front and back, and (d) quartz and silicon substrates with overhang at front.....	52
4.1	Schematic of a PDMS microfluidic platform for delivering fluid to a buckled waveguide chip. PDMS capillaries connect the inlet and outlet wells to the buckled waveguide channels. The waveguide chip is bonded face-down to the PDMS platform.	56
4.2	Photo of a PDMS microfluidic platform interfaced with a hollow waveguide chip. Fluid leakage is a major problem at the PDMS-silicon interface.	57
4.3	Schematic of metal post placement, defining the inlet and outlet wells of the PDMS fluidics. Crystalbond is used beneath the posts to prevent PDMS from leaking underneath during PDMS pouring.	58
4.4	Photo of hollow waveguide samples with PDMS wells fabricated on top. Partial delamination of non-essential areas is visible for samples 1.03, 1.06, and 1.07. The addition of an oxygen plasma step during fabrication eliminated this problem, shown in samples 1.01, 1.04, and 1.05.....	59
4.5	Fluid flow attempt for sample 1.05, in which a syringe was used to force fluid from one well to the other. Fluid has leaked between the silicon substrate and the PDMS layer, due to the pressure exerted at the interface.	60
4.6	Schematic of PDMS basins used to hold fluid at front of tapered waveguide. This configuration relies on the taper itself to form a quasi-seal for the	

	liquid sample. Capillary action draws a thin layer of fluid beneath the taper, limiting the practical benefits of the PDMS basin setup.	62
4.7	Photos of PDMS reservoirs. (a) PDMS microcapillaries are used to deliver fluid to the wide end of the taper chip. (b)-(c) Slab waveguide tapers are placed against the front edge of the PDMS basins to form a weak seal. The fluid analyte is temporarily confined to the small reservoir at the front.	63
4.8	Schematic illustration of a tapered waveguide in a conventional linear variable filter configuration. Sample fluorescence is spatially filtered into Fabry-Perot resonant modes. (b) Schematic illustration of ray guidance in a slowly tapered hollow Bragg waveguide. Fluorescence within the omnidirectional band of the mirrors is adiabatically transformed from a guided mode to a vertical Fabry-Perot mode at cutoff. Adapted from Ref. [8].	64
4.9	(a) Schematic of fluid insertion using integrated platform. The sample is placed at the wide end of the tapered slab waveguide. (b) A taper with quartz substrates and an overhang at both the wide and narrow ends of the taper. The overhang helps to limit stray fluorescence and facilitates fluid insertion at the wide end.	66
5.1	(a) Schematic illustration of ray guidance in a slowly tapered air-core Bragg waveguide. Light within the omnidirectional band of the mirrors is adiabatically transformed from a guided mode to a vertical Fabry-Perot mode at cutoff. (b) Predicted reflectance of evaporated $\text{TiO}_2/\text{SiO}_2$ mirrors (silicon substrate), for TE polarized light at incidence angles of 0, 20, and 75 degrees. Layer thicknesses were assumed to be 61 nm and 90 nm for TiO_2 and SiO_2 , respectively. The symbols are experimental data at 20 degrees.	71
5.2	Schematic illustration of how different wavelengths of light tend to behave in a tapered Bragg waveguide. (a) Light inside the omnidirectional	

reflection band of the mirrors radiates in a near-vertical direction at cutoff. (b) Blue light is well-guided at the wide end of the taper (far from cutoff) but, due to poor normal-incidence reflectance in this range, leaks more as cutoff is approached. Longer wavelengths outside of the omnidirectional band (orange and red light here) are not well-guided by the taper, leaking significantly so that very little light actually reaches cutoff. 73

5.3 (a) Microscope photograph showing a taper in its entirety, with white light coupled into the wide end of the taper, at the left side of the image. Approximately 20 partly overlapping rainbow bands are visible, each one associated with cutoff of a particular mode order (see text). The two lowest mode orders at the right appear dimmer because they are partly obscured by epoxy. (b) A higher magnification image of some 'rainbows' is shown. For sufficiently low mode orders on the right, the FSR is large enough such that the full range of colors (yellow, green, cyan-blue) within the cladding omnidirectional band is well resolved. 75

5.4 (a) Camera image of the light radiated from the taper with simultaneous input (at the left) of 532 nm and 543 nm wavelength laser light. Each pair of lines corresponds to the cutoff position of a particular mode order; mode order decreases towards the right. (b) Plot of the spacing (Δz) between cutoff positions of the two lasers, versus the mode order. 76

5.5 (a) Column-wise averaged pixel intensity versus z , for the $m = 6$ cutoff lines of the simultaneously launched 543 nm and 532 nm lasers (b) As in part (a), but for the $m = 7$ lines. 77

5.6 (a) Camera image of the light radiated from the taper, with waveguide-coupled input of 532 nm and 543 nm wavelength laser light from the left. Each pair of lines corresponds to the cutoff position of a particular mode order; mode order increases towards the right. (b) Plot of the resolution ($d\lambda$) versus mode order, determined by the FWHM and spacing of the laser

	lines for a particular mode order. Experimental resolution is lower than theoretical predictions, in part due to the use of a simple vertical Fabry-Perot cavity model in the derivation of Eq. (5.1).....	79
5.7	A tungsten halogen light source (HL-2000, Ocean Optics) was approximated as a blackbody source (color temperature $T = 2960$ K) to calibrate the spectral response of the spectrometer (USB4000, Ocean Optics). (a) The raw and corrected spectrum of the tungsten halogen source. (b) Approximate correction factor (normalized to a peak value of 1) for the spectral response of the spectrometer in the 400-800 nm wavelength range.	81
5.8	Quantum efficiency (QE) of the CCD in the camera (Coolsnap ES, Photometrics) when operating in 'normal' mode. The QE data was taken from the camera manual [12].....	82
5.9	(a) Super continuum white light source (SuperK Red, Koheras) spectrum obtained using a commercial spectrometer. (b) Spectrum of white light radiating from top of taper, contributed by mode orders $m = 2$ to $m = 5$. The light was collected using an optical fiber (core diameter of 1 mm and $NA = 0.22$) and delivered to the same commercial spectrometer.	83
5.10	Super continuum white light source coupled into wide end of taper using 20X objective lens. (a) Camera image of light radiating through top of taper. Mode orders $m = 2$ to $m = 5$ are shown, from left to right. (b)-(c) Extracted spectra of white light source for mode orders $m = 2$ and $m = 3$, respectively. These spectra compare well to the spectrum collected by the optical fiber, delivered to the commercial spectrometer.	84
5.11	Plot of the correction factor extracted for a particular taper, using light from a super continuum light source. Operating range is centered at ~ 520 nm, with a bandwidth of ~ 70 nm. Data is unreliable below 490 nm due to low signal.	86

5.12	A white LED (model # C503B-WAN-CBaDa231, Digikey) was used to estimate the correction function $C_T(\lambda)$ for mode orders $m = 2$ and $m = 3$ of a taper. Operating range is centered at ~ 520 nm, with a bandwidth of ~ 70 nm. Unlike the case with the super continuum light source, the ratio is reasonable for all wavelengths of interest.	87
5.13	Simulation of radiated power of guided modes versus position, for a taper with a slope of $1.5 \mu\text{m}/\text{mm}$ and TE-polarized light of mode order $m = 2$. Light reaches cutoff for wavelengths between ~ 490 nm and ~ 570 nm, with peak sensitivity at ~ 520 nm.	88
5.14	Plot of the correction function $C_T(\lambda)$ for a taper, estimated using the simulated relative power of light radiated at cutoff, for different wavelengths. Also plotted is the correction function obtained using the white LED data. There is good agreement between the experimental and simulated results, confirming the validity of the method for measuring the operating range of the tapers.	88
6.1	Schematic illustration of a tapered slab Bragg waveguide in a conventional linear variable filter configuration. The taper spatially filters polychromatic light into Fabry-Perot resonant modes. (a) Fluorescent microspheres positioned beneath the taper in a glass capillary. (b) Fluorescent microspheres placed in direct contact with the underside of the taper, forming a thin film between the taper and the PDMS basin.	93
6.2	(a) Camera image of spectrally-resolved fluorescence from Orange (540/560) FluoSpheres, for the case of a capillary placed below the taper. Mode orders $m = 1$ to $m = 4$ are shown. The discrete green lines are due to scattered light from the 532 nm excitation laser. (b) The extracted emission spectrum of the Orange FluoSpheres for mode order $m = 1$. Compared to the spectrum collected by a commercial spectrometer (USB4000, Ocean Optics), there is significant discrepancy at longer wavelengths.	94

6.3	Transfer-matrix simulations of the LVF cavity transmittance. The LVF is relatively transparent outside of the stop-band of the mirrors, and light in that range causes interference at the detector.....	95
6.4	(a) Camera image of fluorescence from a film of Orange (540/560) FluoSpheres placed directly in contact with the underside of the taper. Mode orders $m = 2$ to $m = 5$ are shown. (b) Emission spectrum of Orange FluoSpheres for mode order $m = 4$. Compared to the spectrum collected by a commercial spectrometer, there is significant discrepancy at higher wavelengths.....	97
6.5	Schematic illustration of ray guidance in a slowly tapered hollow Bragg waveguide. Light within the omnidirectional band of the mirrors is adiabatically transformed from a guided mode to a vertical Fabry-Perot mode at cutoff. (a) Capillary filled with microspheres aligned near wide end of the taper (b) Fluorescent microspheres inserted into the taper cavity.	98
6.6	(a) Spectrally-resolved fluorescence from a capillary filled with Yellow-Green (505/515) FluoSpheres, aligned near the wide end of a taper. Fluorescence associated with mode orders $m = 2$ to $m = 5$ are shown. (b) Extracted taper spectra for mode orders $m = 2$ to $m = 5$. Compared to a reference scan of the capillary, the extracted taper spectra are modified by the 'instrument response' of the taper.	100
6.7	Plot of the correction function $C_T(\lambda)$ for a taper, estimated using the simulated relative power of light radiated at cutoff, for different wavelengths. Also plotted is the correction function obtained using the white LED data.	101
6.8	Extracted taper spectra for mode orders $m = 2$ to $m = 5$ (see Fig. 6.6(a)). The reference scan of the capillary was divided by the correction function of the taper to help assess the validity of the results. The modified emission	

spectrum and experimental data agree well for the mode orders shown.
..... 102

6.9 Corrected taper spectra for mode orders $m = 2$ to $m = 5$ (see Fig. 6.6(a)). In this case, the raw taper spectra were multiplied by the experimentally determined correction function of the taper to obtain a more accurate representation of the fluorescence spectrum. Within the operating range of the taper, the extracted spectra agree relatively well with the spectrum measured by a commercial spectrometer. Near the edges of the operating range, decreased detection sensitivity leads to a less accurate representation of the spectra..... 103

6.10 Corrected taper spectra for mode orders $m = 2$ to $m = 5$ (see Fig. 6.6(a)). The raw taper spectra were multiplied by the theoretically determined correction function of the taper. In this case, the extracted spectra are in agreement with the commercial spectrometer measurement over a wider wavelength range compared to the results in Fig. 6.9. Nevertheless, decreased detection sensitivity near the edges of the operating range still hampers the ability to reproduce an accurate spectrum there. 104

6.11 A 0.5% solids (8.2×10^{13} particles/mL) solution of ~ 48 nm diameter Orange (540 Ex/560 Em) FluoSpheres was inserted into the wide end of the taper. A long strip of SU-8 and a row of rectangular Su-8 posts are visible on the right side of the image (i.e. the wide end of the taper). The image is filled with a yellow tinge due to stray fluorescence. The FluoSpheres were not confined to the wide end of the taper (as intended), instead collecting towards the narrow end. 105

6.12 A 0.5% solids solution of ~ 48 nm diameter Orange (540 Ex/560 Em) FluoSpheres was mixed with an UV-curable optical adhesive (NOA 61, Norland) instead of distilled water, then inserted into the wide end of a taper (at right). Clumping of the microspheres is made apparent by the

	presence of bright spots. As well, the microspheres infiltrated farther into the taper cavity than desired.....	107
6.13	A 0.5% solids solution of ~48 nm diameter Orange (540 Ex/560 Em) FluoSpheres mixed with optical adhesive, with the water evaporated, was inserted into the wide end of a taper (at right). The result is a much more uniform distribution of microspheres suspended in optical adhesive. The evaporation of the water also helped to increase the viscosity of the mixture, preventing the mixture from infiltrating too far into the taper cavity before being cured.	108
6.14	A single 4.1 μm Yellow-Green (505/515) FluoSphere that was lodged in a taper cavity. (a) The coupling point of the 374 nm laser (underneath the overhang), as well as the fluorescence from the microsphere are visible. (b) The fluorescence appears to be coupling into cutoff points for mode orders near where the microsphere is lodged.	109
6.15	Using a 20x objective lens, a 473 nm laser beam was coupled into the wide end of the taper. The laser was carefully focused onto a pair of closely-spaced 4.1 μm Yellow-Green FluoSpheres, causing them to fluoresce. (a) A 2-second exposure time causes the pair of FluoSpheres to appear as a single bright spot. The wide end of the taper is indicated by the illuminated SU-8 posts on the right side of the image. (b) An image of the pair of fluorescing FluoSpheres with a shorter exposure time. These two FluoSpheres are estimated to each contain at least 2.5×10^8 Fluorescein equivalents.....	110
6.16	Spectrally-resolved fluorescence from a pair of Yellow-Green (505/515) FluoSpheres of 4.1 μm diameter, lodged part-way into the taper cavity. Fluorescence associated with mode orders $m = 2$ to $m = 5$ is shown. Bright spots are likely due to scattering of stray light (b) Extracted raw taper spectra for mode orders $m = 2$ to $m = 5$	111

6.17 Corrected taper spectra for mode orders $m = 2$ to $m = 5$ (see Fig. 6.15(a)). The raw taper spectra were multiplied by the theoretically determined correction function of the taper. Decreased sensitivity on the edges of the operating range results in a poor reproduction of the fluorescence spectrum in there. As well, the correction process is hampered by a low signal-to-noise ratio and roughness in the measured spectra. 112

List of Symbols and Abbreviations

Symbols

a, b	Cladding layer thicknesses [m]
b	Half-width of a strip to be buckled [m] (Chapter 2.4)
c_0	Speed of light in vacuum [m/s]
C_{CCD}	Camera correction factor
C_s	Correction factor to be applied to raw spectrometer data
C_T	'Instrument response' correction factor for a taper
d	Core thickness [m]
d_{cm}	Cavity thickness for a mode m [m]
D_T	Spatial dispersion imparted by the taper
dz	FWHM of individual laser lines [m]
$d\lambda$	Wavelength resolution [m]
$d\lambda_E$	Experimental wavelength resolution [m]
E	Young's modulus [Pa]
h	Film thickness [m]
K	Phase-shift coefficient
k_0	Free-space wavenumber [m^{-1}]
k_x	Transverse component of the wave vector [m^{-1}]
k_z	Complex modal propagation constant
m	Integer
N	Integer

n_1, n_2	Refractive indices of the cladding layers
n_i	Refractive index of the incident medium
n_i	Sine of the incident angle ϕ for an effective index layer i (Chapter 2.3.2)
N_i	Effective index of a layer i
n_s	Refractive index of the substrate
R	Normal-incidence reflectance of the cladding mirrors
R_{QWS}	Peak reflectance at normal incidence for an $N \frac{1}{2}$ period QWS
r_T, r_B	Amplitude reflection coefficients of the top and bottom mirrors
R_T, R_B	Reflectances from the top and bottom mirrors
S_C	Corrected spectral response of a spectrometer or a reference spectrum
S_R	Raw (uncorrected) spectral response of a spectrometer
S_T	Absolute value of the taper slope
S_T	Raw spectrum obtained from plot of pixel intensity
z_p	Effective detector array pixel size [m]
α_i	Intensity attenuation factor for an effective index layer i [m^{-1}]
α_m	Intensity attenuation factor for the mode [m^{-1}]
β_m	Mode propagation constant
$\delta(y)$	Normal displacement function of the Euler buckling mode [m]
δ_c	Cutoff for a guided mode [m]
δ_i	Core height for an effective index layer i [m]
δ_{max}	Peak buckle height of Euler buckle [m]
Δz	Spacing between cutoff positions of two lasers [m]
$\Delta \lambda$	Wavelength difference of two lasers [m]
$\Delta \lambda_{0,1}$	Width of the fundamental stop band at normal incidence [m]

θ	Angle relative to normal
λ_0	Free space wavelength
$\lambda_{0,B}$	Free space Bragg wavelength [m]
ν	Poisson's ratio
σ_c	Critical compressive biaxial stress to induce buckling in a strip [Pa]
σ_o	Biaxial compressive stress in film [Pa]
Φ_T, Φ_B	Phase shift on reflection from top and bottom mirrors, respectively
ω	Angular frequency of mode [rad s ⁻¹]
$\delta\lambda_{FSR}$	Free spectral range in terms of wavelength [m]
ϕ_m	Angle of incidence for the mode

Abbreviations

μ APD	Micro-avalanche photodiode
Alq ₃	tris(8-hydroxyquinoline) aluminum
Ar	Argon
ARROW	Anti-resonant reflecting optical waveguide
a-Si	Amorphous silicon
AWG	Arrayed waveguide grating
CCD	Charge-coupled device
CD	Chromatic dispersion
CMOS	Complementary metal–oxide–semiconductor
Cy3	Indocarbocyanine
DC	Direct current

DCM	4-dicyanomethylene-2-methyl- 6-(p-dimethylaminostyryl)-4H-pyrane
e-beam	Electron beam
Ex,Em	Excitation and emission
FITC	Fluorescein Isothiocyanate
FSR	Free spectral range
FWHM	Full width at half maximum
GaP	Gallium phosphide
GD	Group delay
GFP	Green fluorescent protein
ICP-RIE	Inductively coupled plasma reactive ion etch
IPA	Isopropyl alcohol
LAL	Low adhesion layer
LCW	Liquid core waveguide
LED	Light-emitting diode
LOC	Lab-on-a-chip
LP	Long-pass
LVF	Linear variable filter
MEMS	Microelectromechanical systems
NA	Numerical aperture
PDMS	Polydimethylsiloxane
PVD	Physical vapour deposition
QE	Quantum efficiency
QWS	Quarter-wave stack
SEM	Scanning electron microscopy

Si	Silicon
SiO ₂	Silicon dioxide
SNR	Signal-to-noise ratio
TE	Transverse electric
TiO ₂	Titanium dioxide
TIR	Total internal reflection
UV	Ultraviolet
VASE	Variable angle spectroscopic ellipsometer
VCSEL	Vertical-cavity surface-emitting laser

1 Introduction

This thesis describes the design, fabrication, and characterization of tapered air-core Bragg waveguide spectrometers for lab-on-a-chip (LOC) applications. Results are reported for a prototype sensing system based on spectrally-resolved fluorescence detection. The present work stems from previous efforts of our research group, which were adapted here for applications in the visible band. The current chapter gives a basic introduction to optofluidic LOCs and applications of tapered Bragg waveguides, helping to frame the rest of the thesis in the context of the relevant literature.

1.1 Optofluidic lab-on-a-chip devices

Research on LOC devices has grown recently, with continued development of technologies that could make truly portable diagnostics systems possible. Besides the most obvious benefit of increased portability, LOCs offer a multitude of potential advantages over bulk laboratory systems, such as increased automation and reduced costs [1]. Ideally, a LOC device should be able to fully accomplish its task without the aid of external elements. This is not always possible, as it may be both costly and difficult to find an alternative to certain discrete components [2].

Optofluidic LOCs are an effort to combine microfluidic devices with optics to allow for on-chip imaging and spectroscopy. Optical detection methods are a natural choice for LOCs, as they are highly sensitive, usually non-invasive, and have high temporal and spatial resolution [3]. A wide variety of optical detection

schemes have been successfully implemented in LOC systems, including fluorescence detection [4]–[6], surface-enhanced Raman scattering detection [7], and absorption detection [8].

PDMS is a popular material for LOC devices, as it is easy to build complex systems of microfluidic channels and other components, such as PDMS micropumps [9]. However, there are some disadvantages to using PDMS in an optofluidic system. PDMS has a fluorescence response overlapping with fluorophores such as FITC, Cy3, and GFP [10]. In order to mitigate this problem, fluorophores with higher excitation wavelengths or a different substrate (such as glass or quartz) may be used.

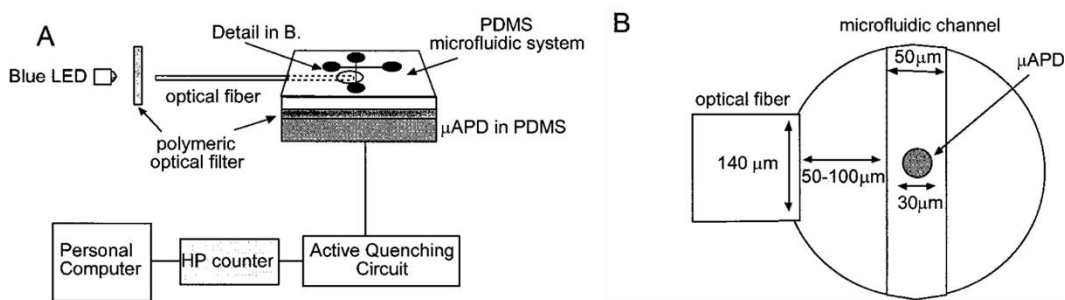


Figure 1.1 – Experimental setup of a fluorescence detection system in PDMS. Adapted from Ref. [11].

An example of a prototype fluorescence detection system, making use of PDMS microfluidics and a micro-avalanche photodiode (μ APD) array, is shown in Fig. 1.1. With this setup, the background photon count rate for an illuminated channel was as high as five times that of the dark count rate. Better filtering would help to reduce this problem, but an even better solution would be the use of a

laser excitation source paired with an appropriate filter to block the excitation light. This illustrates the common problem of maximizing the signal (fluorescence in this case) while also minimizing the noise (excitation light) at the detector.

1.2 Fluorescence spectroscopy in LOC devices

Many LOC systems still rely on external instrumentation for spectral analysis, often coupling to an external spectrometer. The implementation of a chip-scale spectrometer would allow for a more fully integrated and independent LOC. Figure 1.2 shows an example of a chip-scale spectrometer, utilizing a CMOS image sensor, filtered by a linear variable band-pass filter to map each pixel to a different wavelength. This spectrometer is aligned to a fluidic channel, in which the sample particles are continuously being induced to fluoresce. As the particle moves along the channel, each pixel is responsible for capturing a small portion of the fluorescence spectrum.

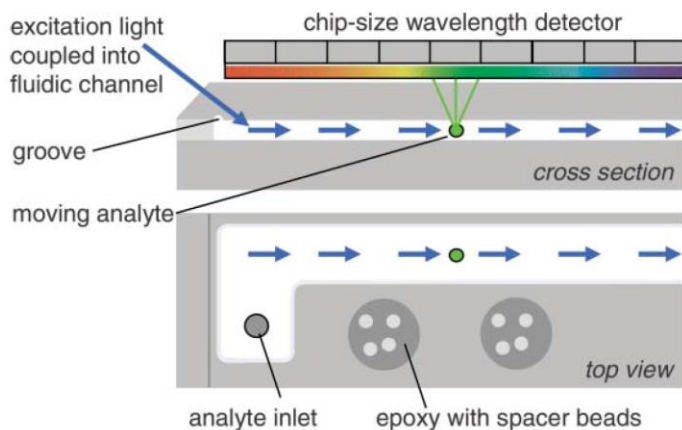


Figure 1.2 – Example of a chip-scale spectrometer used to measure the fluorescence spectrum of an analyte. Adapted from Ref. [12].

Figure 1.3 shows an example of another method for integrating a microspectrometer into a fluorescence based LOC system. Here, an arrayed waveguide grating (AWG) is used to spectrally resolve fluorescence. An array of waveguides is fabricated with linearly varied path lengths so that there is a phase shift between light exiting from the different waveguides [13]. The device was designed such that the output channels sample the spectrum at 10 nm intervals. In order to increase spectral resolution, a larger array of waveguides with closer spacing would need to be used. As reported, such a system should be sufficient to discriminate multiple fluorescent species, given a large enough separation between emission spectra.

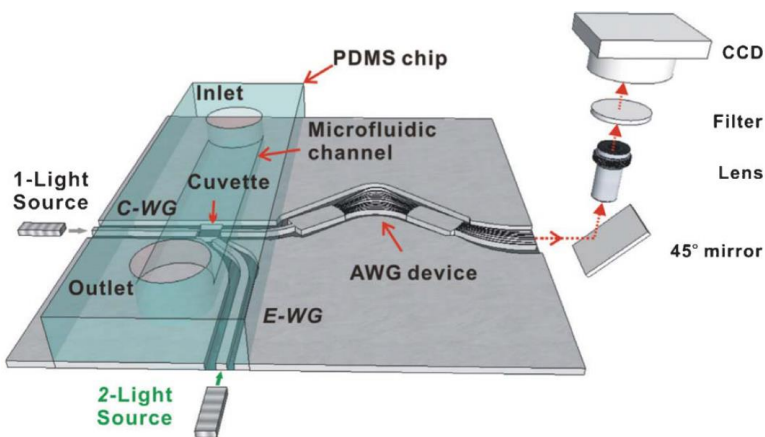


Figure 1.3 – An example of a LOC for fluorescence detection, using an arrayed waveguide grating (AWG). Adapted from Ref. [13].

1.3 Integrated hollow waveguides

Optical waveguides have traditionally been used for the singular purpose of guiding light from one location to another, relying on the principle of total internal reflection (TIR) to do so. Light is guided in a high refractive index core, surrounded

by low-index claddings. These dielectric waveguides can have extremely low loss and offer high confinement of light, but are limited to certain material systems. In particular, total internal reflection implies that light is guided within a high index core material. In LOCs, there are significant advantages to having a liquid (or air) core instead of a solid core. The most obvious advantage is the possibility to deliver excitation light to the sample within the waveguide itself, allowing for optimal light interaction between the light and the sample.

There are a number of ways to implement a liquid core waveguide (LCW), such as using TIR in a way that facilitates the use of a low index liquid core. For example, an even lower index cladding, such as Teflon AF ($n \sim 1.29$), may be used to satisfy the TIR condition in certain cases [14]. Figure 1.4(a) shows a schematic illustration of such a device. Another method is to add air pores (10 – 15 nm in diameter) to a high index cladding material, shown in Fig. 1.4(b). The pores lower the average refractive index of the cladding below that of the liquid core, so that TIR may occur.

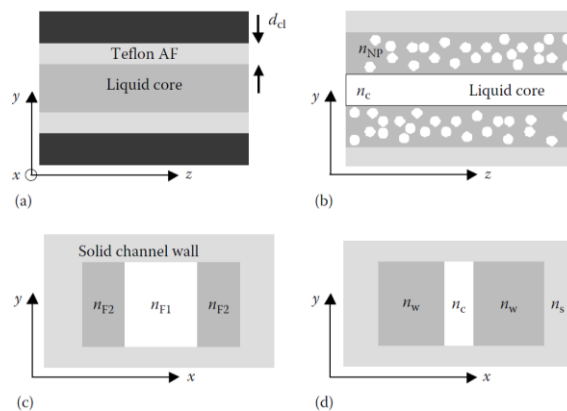


Figure 1.4 – Liquid core waveguides using refractive index guiding. (a) Teflon AF cladding, (b) Air nano-pore cladding, (c) Liquid cladding, (d) Slot waveguide. Adapted from Ref. [14].

Figure 1.4(c) shows a third method, in which the sample fluid core is flowed between two lower index liquid claddings within the fluidic channel. A drawback to this method is possible mixing of the core and cladding fluids, as well as increased complexity in fluid flow. The use of a slot waveguide (see Fig. 1.4(d)) is another promising index guiding method for liquid-core waveguides. Most of the light is confined to a nanometer-scale liquid-core slot, allowing for picoliter or even sub-picoliter sample volumes [14].

Another option for light confinement in a hollow core is the use of interference-based waveguides. One type of interference waveguide is the anti-resonant reflecting optical waveguide (ARROW), which relies on anti-resonance between the dielectric cladding layers for guiding. In this approach, periodicity is not necessarily required for low propagation loss [15].

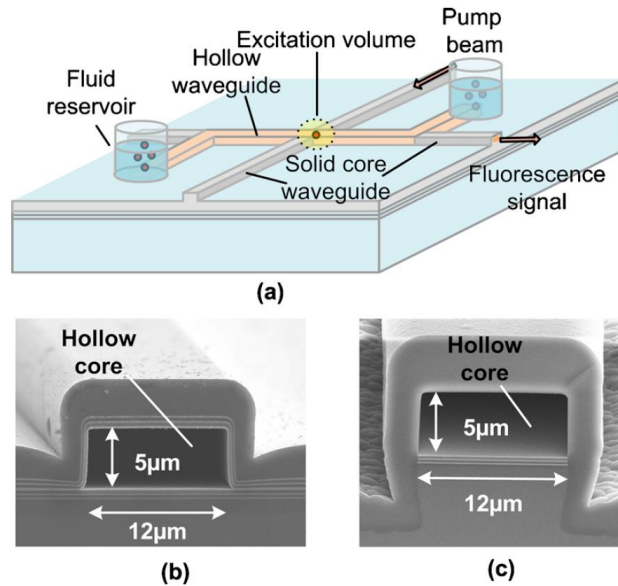


Figure 1.5 – Example of an ARROW LOC device. Adapted from Ref. [15].

Figure 1.5 shows an example of ARROW waveguides being used in an optofluidic sensing platform. A hollow ARROW waveguide is used to carry the sample fluid, and is coupled to solid core waveguides to facilitate easier coupling to external components. A noted advantage of ARROW waveguides is that they facilitate coupling of light between a hollow waveguide and a solid-core waveguide, as shown in Fig. 1.5 [15].

Another type of interference waveguide is the Bragg waveguide, which is the principle focus of this thesis. In a periodic structure with alternating high index and low index layers, the reflection from each interface will constructively interfere. This results in high reflectance over a range of wavelengths, called a stop-band. As with any air-core waveguide, loss is determined by the magnitude of the reflection at the boundaries. While ARROW waveguides tend to operate in a quasi-single mode regime [15], Bragg waveguides tend to support multiple guided modes.

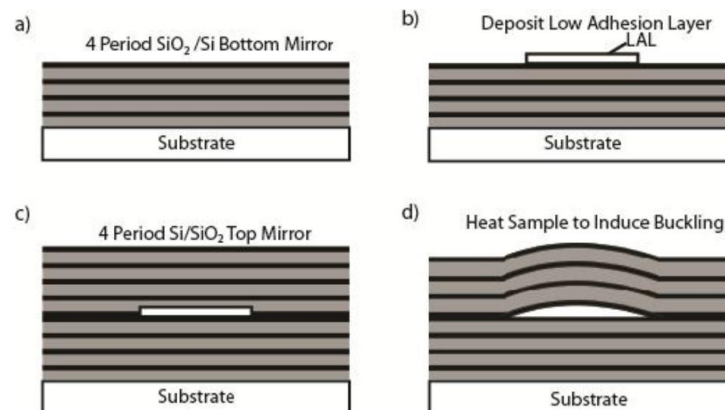


Figure 1.6 – Schematic showing the process to fabricate hollow channel waveguides. Adapted from Ref. [16].

Previously [16], our research group developed a buckling delamination process for SiO₂/Si hollow channel Bragg waveguides, shown in Fig. 1.6. These channel waveguides may potentially be used to guide light and simultaneously confine a sample fluid. More recently, our research group has fabricated tapered hollow slab Bragg waveguides using a wafer-bonding process [17]. Due to the slab geometry of these waveguides, taking advantage of the hollow core for fluid handling purposes is less straight-forward. Chapter 4 discusses the development of methods for fluid delivery into buckled hollow waveguides as well as into slab hollow waveguide tapers.

1.4 Applications of tapered Bragg waveguides

This thesis mainly focused on the implementation and application of tapered, air-core Bragg waveguides as spectroscopic instruments. There are, however, a number of other uses for tapered Bragg waveguides, some of which are also applicable to LOC devices. This section gives some alternative applications of tapered Bragg waveguides from the literature.

1.4.1 Linear variable filter-based micro-spectrometers

Perhaps the most apparent use for a tapered Bragg waveguide in LOCs is as a micro-spectrometer. The tapered waveguide may be viewed as a Fabry-Perot cavity, with linearly varying cavity thickness. In this setup, the taper acts as a linear variable filter (LVF), filtering light according to the cavity resonance satisfied at a given position along the taper. Due to the angular dependence of

the resonance condition, collimating optics must be used to suppress off-axis light. This type of setup is best suited for broad-area and uniform sources, although moving point sources may also be detected using alternative approaches [18].

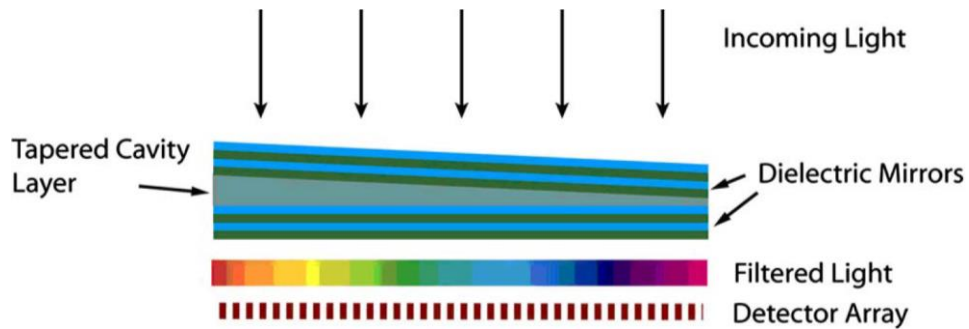


Figure 1.7 – Example of a tapered Fabry-Perot cavity LVF. Adapted from Ref. [19].

Figure 1.7 shows an example of a tapered Fabry-Perot cavity LVF. In this case, photoresist was reflowed to create the tapered cavity layer. A disadvantage of this fabrication method is that, unlike the hollow waveguides, the cavity here may not be used as a microfluidic channel. This somewhat limits the versatility of these devices for LOC applications.

Another drawback of using tapered Bragg waveguides as LVFs is that light outside the stop-band of the mirrors will leak through, decreasing the utility of the LVF. A significant advantage of side-coupled LVFs is that they do not suffer from this limitation [20]. Light outside of the omnidirectional band of the cladding mirrors is not well guided, and is therefore not expected to be significantly present in the measured signal. These details are discussed further in Chapter 2.

1.4.2 Photonic integrated circuit components

Tapered Bragg waveguides also have a variety of potential uses in integrated photonic circuits, including: tunable optical delay lines, interferometers, chromatic dispersion compensators, and dispersion slope compensators [21]. For many of these components, tunability is important. One way of accomplishing this is by using MEMS-based micro-mirrors as one or both claddings of the hollow waveguides [21]. By doing so, waveguide properties such as group delay (GD) and chromatic dispersion (CD) may be freely tuned and optimized for their prescribed purpose.

Because the cutoff position in a tapered waveguide is wavelength-dependent, a multiplexer/demultiplexer may also be realized [22]. A schematic of how this might be accomplished is shown in Fig. 1.8. The demultiplexer (i.e. using a photodiode array to collect vertically radiated light) is equivalent to a side-coupled LVF spectrometer with a CCD array to collect light. Relating to LOC detection systems, a multiplexer using vertical-cavity surface-emitting lasers (VCSELs) would be able to deliver excitation light of multiple wavelengths to a sample.

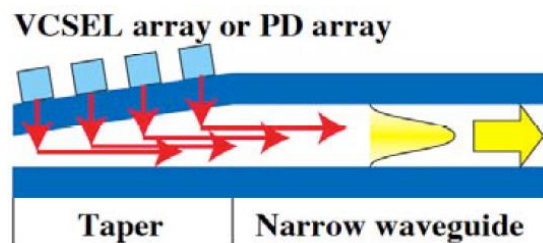


Figure 1.8 – Schematic of potential application of a hollow tapered waveguide as a multiplexer/demultiplexer. Adapted from Ref. [22].

1.4.3 Tunable organic microcavity lasers

Another potential application for tapered Bragg waveguides is in a tunable organic microcavity laser, an example of which is shown in Fig. 1.9. Here, a tapered active organic layer of Alq₃:DCM is embedded between two Bragg reflectors. The microcavity is pumped by a frequency doubled solid-state laser at 532 nm. Depending on the position along the taper to which the pump-beam is focused, the wavelength of the radiated light will change. In this way, the organic laser may be tuned over a range of wavelengths within the stop-band of the Bragg reflectors. Microcavity lasers have potential for use in LOCs as excitation sources, as well as in optical communications and integrated optical circuits [23].

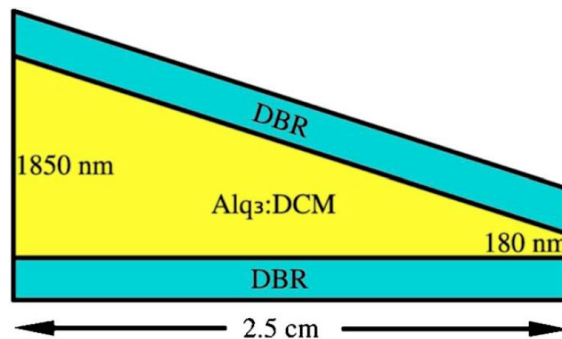


Figure 1.9 – Schematic of a wedge-shaped microcavity used in a tunable organic laser. Adapted from Ref. [23].

1.5 Summary of thesis

This goal of this thesis was to develop a prototype fluorescence LOC device by integrating tapered air-core spectrometers with microfluidics. The chapters are summarized below:

Chapter 2 discusses background theory pertaining to tapered omnidirectional Bragg reflector waveguides, delamination buckles, and fluorescence. These concepts help lay the foundation for the remaining chapters.

Chapter 3 describes the development of fabrication processes for tapered hollow Bragg waveguides operating in the visible range. Cladding mirrors were deposited using reactive sputtering as well as electron beam evaporation. The deposition parameters were adjusted to optimize film stress while maintaining good optical quality. Tapers were assembled using two different methods: buckling self-assembly and a wafer-bonding process.

Chapter 4 details a variety of methods employed to interface microfluidics with the tapered waveguide spectrometers. Methods were developed (with varying success) to deliver fluorescent samples to buckled channel waveguides as well as to slab waveguides.

Chapter 5 describes experiments done to evaluate the performance of the slab Bragg waveguide tapers as spectrometers. Lasers of various wavelengths were used to assess dispersion and resolution. As well, white light sources were used to estimate the operating range of the tapers. Simulations of radiated power versus position were used to corroborate the experimental results.

Chapter 6 describes the results of fluorescence experiments using the tapered slab Bragg waveguides. The tapers were used in a conventional LVF configuration as well as in a side-coupled LVF configuration.

Chapter 7 offers some thoughts regarding the work as a whole, as well as the direction that future work should take.

1.6 Works Cited

- [1] C. Monat, P. Domachuk, and B. J. Eggleton, “Integrated optofluidics: A new river of light,” *Nat. Photonics*, vol. 1, no. 2, pp. 106–114, Feb. 2007.
- [2] F. B. Myers and L. P. Lee, “Innovations in optical microfluidic technologies for point-of-care diagnostics,” *Lab Chip*, vol. 8, no. 12, p. 2015, 2008.
- [3] P. S. Dittrich and A. Manz, “Single-molecule fluorescence detection in microfluidic channels--the Holy Grail in muTAS?,” *Anal. Bioanal. Chem.*, vol. 382, no. 8, pp. 1771–82, Aug. 2005.
- [4] D. Yin, E. J. Lunt, a Barman, a R. Hawkins, and H. Schmidt, “Microphotonic control of single molecule fluorescence correlation spectroscopy using planar optofluidics.,” *Opt. Express*, vol. 15, no. 12, pp. 7290–5, Jun. 2007.
- [5] C. Vannahme and S. Klinkhammer, “Plastic lab-on-a-chip for fluorescence excitation with integrated organic semiconductor lasers,” *Opt. Express*, vol. 19, no. 9, pp. 8179–8186, Apr. 2011.
- [6] J. A. Wahl, J. S. Van Delden, and S. Tiwari, “Multiple-fluorophore-specie detection with a tapered Fabry-Perot fluorescence spectrometer.,” *Appl. Opt.*, vol. 44, no. 25, pp. 5190–7, Sep. 2005.
- [7] P. Measor, L. Seballos, D. Yin, J. Z. Zhang, E. J. Lunt, A. R. Hawkins, and H. Schmidt, “On-chip surface-enhanced Raman scattering detection using integrated liquid-core waveguides,” *Appl. Phys. Lett.*, vol. 90, no. 21, p. 211107, 2007.
- [8] M. L. Adams, M. Enzelberger, S. Quake, and A. Scherer, “Microfluidic integration on detector arrays for absorption and fluorescence microspectrometers,” *Sensors Actuators A Phys.*, vol. 104, no. 1, pp. 25–31, Mar. 2003.
- [9] J. Ni, F. Huang, B. Wang, B. Li, and Q. Lin, “A planar PDMS micropump using in-contact minimized-leakage check valves,” *J. Micromechanics Microengineering*, vol. 20, no. 9, p. 095033, Sep. 2010.
- [10] S. Pennathur and D. K. Fygenson, “Improving fluorescence detection in lab on chip devices.,” *Lab Chip*, vol. 8, no. 5, pp. 649–52, May 2008.

- [11] M. Chabinyc and D. Chiu, "An integrated fluorescence detection system in poly (dimethylsiloxane) for microfluidic applications," *Anal. Chem.*, vol. 73, no. 18, pp. 4491–4498, 2001.
- [12] O. Schmidt, M. Bassler, P. Kiesel, C. Knollenberg, and N. Johnson, "Fluorescence spectrometer-on-a-fluidic-chip.," *Lab Chip*, vol. 7, no. 5, pp. 626–9, May 2007.
- [13] Z. Hu, A. Glidle, C. N. Ironside, M. Sorel, M. J. Strain, J. Cooper, and H. Yin, "Integrated microspectrometer for fluorescence based analysis in a microfluidic format.," *Lab Chip*, vol. 12, no. 16, pp. 2850–7, Aug. 2012.
- [14] H. Schmidt, "Integrated Optofluidic Waveguides," CRC Press, 2010, pp. 16–28.
- [15] Y. Zhao, M. Jenkins, P. Measor, K. Leake, S. Liu, H. Schmidt, and a R. Hawkins, "Hollow waveguides with low intrinsic photoluminescence fabricated with Ta(2)O(5) and SiO(2) films.," *Appl. Phys. Lett.*, vol. 98, no. 9, p. 91104, Feb. 2011.
- [16] E. Epp, N. Ponnampalam, W. Newman, B. Drobot, J. N. McMullin, A. F. Meldrum, and R. G. DeCorby, "Hollow Bragg waveguides fabricated by controlled buckling of Si/SiO₂ multilayers," *Opt. Express*, vol. 18, no. 24, pp. 24917–24925, Nov. 2010.
- [17] B. Drobot, A. Melnyk, M. Zhang, T. W. Allen, and R. G. DeCorby, "Visible-band dispersion by a tapered air-core Bragg waveguide," *Opt. Express*, vol. 20, no. 21, pp. 23906–23911, Oct. 2012.
- [18] O. Schmidt, P. Kiesel, and M. Bassler, "Performance of chip-size wavelength detectors.," *Opt. Express*, vol. 15, no. 15, pp. 9701–6, Jul. 2007.
- [19] A. Emadi, H. Wu, G. de Graaf, P. Enoksson, J. H. Correia, and R. Wolffenbuttel, "Linear variable optical filter-based ultraviolet microspectrometer.," *Appl. Opt.*, vol. 51, no. 19, pp. 4308–15, Jul. 2012.
- [20] R. G. DeCorby, N. Ponnampalam, E. Epp, T. Allen, and J. N. McMullin, "Chip-scale spectrometry based on tapered hollow Bragg waveguides," *Opt. Express*, vol. 17, no. 19, pp. 16632–16645, Sep. 2009.
- [21] Y. Sakurai and F. Koyama, "Control of Group Delay and Chromatic Dispersion in Tunable Hollow Waveguide with Highly Reflective Mirrors," *Jpn. J. Appl. Phys.*, vol. 43, no. 8B, pp. 5828–5831, Aug. 2004.

- [22] T. Miura, Y. Yokota, and F. Koyama, "Proposal of tunable demultiplexer based on tapered hollow waveguide with highly reflective multilayer mirrors," *2005 IEEE LEOS Conf. Proc.*, pp. 272–273, Oct. 2005.
- [23] B. Schütte, H. Gothe, S. I. Hintschich, M. Sudzius, H. Fröb, V. G. Lyssenko, and K. Leo, "Continuously tunable laser emission from a wedge-shaped organic microcavity," *Appl. Phys. Lett.*, vol. 92, no. 16, p. 163309, 2008.

2 Theory

2.1 Introduction

This chapter discusses background theory pertaining to tapered omnidirectional Bragg reflector waveguides, delamination buckles, and fluorescence. These concepts lay the foundation for topics discussed in Chapters 3, 4, 5, and 6.

2.2 Omnidirectional Bragg reflector waveguides

2.2.1 Leaky dielectric waveguides

To support lossless modes, a waveguide must have perfectly reflecting mirrors. Theoretically, this may be accomplished by using total internal reflection (TIR), a perfectly conducting metal, or a lossless photonic crystal. In reality, mirror reflectance is always less than unity because of material absorption and interface roughness. Therefore, power in a guided mode will decay as it propagates in any real waveguide. Figure 2.1 shows a schematic illustration of loss (due to material absorption) and leakage (due to imperfect mirrors) of a guided mode in a leaky waveguide.

For the case of an air-core waveguide with perfectly reflecting mirrors, non-leaky modes are solved using the transverse resonance condition [1]:

$$2 \cdot k_x \cdot d - \Phi_T - \Phi_B = m \cdot 2\pi \quad , \quad (2.1)$$

where Φ_T and Φ_B are the phase shifts on reflection from the top and bottom mirrors, respectively, k_x is the transverse component of the wave vector in the core, and m is an integer ($m=0,1,2,\dots$).

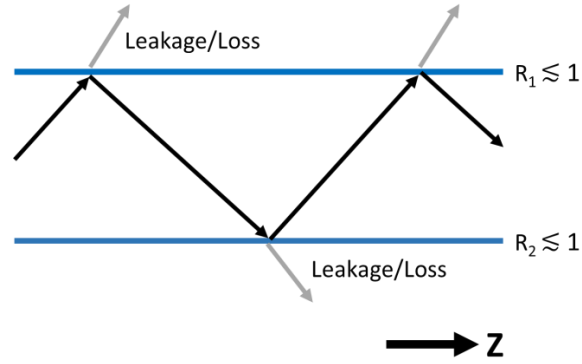


Figure 2.1 – A schematic illustration of loss (due to material absorption) and leakage (due to imperfect mirrors) of a guided mode in a leaky waveguide.

For leaky guided modes, a self-consistent field must satisfy a more general transverse resonance condition [2]:

$$r_T r_B \exp(-j \cdot 2 \cdot k_x \cdot d) = 1 \quad , \quad (2.2)$$

where r_T and r_B are the amplitude reflection coefficients of the top and bottom mirrors, for a given ray incident angle, and k_x is a complex-valued transverse propagation constant. By solving (2.2), complex modal propagation constants are obtained [1]:

$$k_z = \sqrt{k_0^2 - k_x^2} = \beta_m - j \cdot \frac{\alpha_m}{2} \quad , \quad (2.3)$$

where k_0 is the free-space wavenumber, β_m is the mode propagation constant, and α_m is the intensity attenuation factor for the mode.

The attenuation factor α_m for a leaky slab waveguide can be approximated using a ray-optics model [3]:

$$\alpha_m = \frac{-\ln(R_T R_B)}{2 \cdot d \cdot \tan \phi_m} , \quad (2.4)$$

where ϕ_m is the angle of incidence, R_T and R_B are the reflectances from the top and bottom mirrors, and d is the core thickness. In a tapered waveguide, the bounce angle will decrease as the ray propagates towards the narrow end of the taper. This causes the attenuation factor to increase until, at normal-incidence, the guided mode reaches cutoff and the power is radiated vertically from the waveguide.

2.2.2 Bragg reflectors

Consider an air-core slab waveguide with periodic semi-infinite claddings (with refractive indices n_1 and n_2). Figure 2.2 shows a schematic of such a structure, as well as the transverse field distribution of the fundamental mode [4].

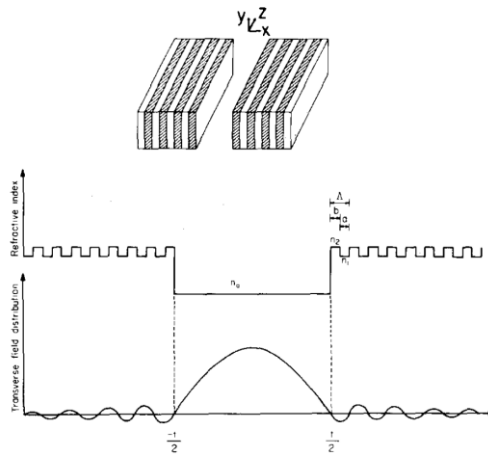


Figure 2.2 – Schematic of an air-core slab waveguide with periodic semi-infinite claddings (with refractive indices n_1 and n_2). The transverse field distribution of the fundamental mode is also shown. Adapted from Ref. [4].

Incident light is partially reflected at each boundary within the periodic cladding. Constructive interference of light within the stop band of the Bragg reflector results in complete reflection. The normal-incidence fundamental stop band is centered at the free space Bragg wavelength [5]:

$$\lambda_{0,B} = 2(n_1a + n_2b) \quad , \quad (2.5)$$

where $\lambda_{0,B}$ is the free space Bragg wavelength and a and b are the cladding layer thicknesses for layers with refractive indices of n_1 and n_2 , respectively. A special case satisfying this condition is the quarter-wave stack (QWS):

$$a = \frac{\lambda_{0,B}}{4n_1} \quad b = \frac{\lambda_{0,B}}{4n_2} \quad , \quad (2.6)$$

This condition results in the widest and ‘strongest’ stop band for a pair of materials. For a QWS, the width of the fundamental stop band at normal incidence is given by [6]:

$$\Delta\lambda_{0,1} = \lambda_{0,B} \cdot \frac{4}{\pi} \sin^{-1} \left| \frac{n_2 - n_1}{n_2 + n_1} \right| \quad , \quad (2.7)$$

This equation indicates that a sufficiently large index contrast is crucial for obtaining a wide stop band. For an $N \frac{1}{2}$ period QWS, the peak reflectance at normal incidence is given by [6]:

$$R_{QWS} = \left(\frac{1 - \left(\frac{n_2}{n_i}\right)\left(\frac{n_2}{n_s}\right)\left(\frac{n_2}{n_1}\right)^{2N}}{1 + \left(\frac{n_2}{n_i}\right)\left(\frac{n_2}{n_s}\right)\left(\frac{n_2}{n_1}\right)^{2N}} \right)^2 \quad , \quad (2.8)$$

where n_2 and n_1 are the layer indices, n_i is the refractive index of the incident medium, and n_s is the refractive index of the substrate (i.e. exit medium). The peak reflectance scales quickly with the number of periods N , and again a higher index contrast between materials is beneficial.

2.2.3 Omnidirectional Bragg reflectors

The stop band of a Bragg reflector is dependent on both the polarization and the incident angle of light. It is useful to make an omnidirectional band, for which any polarization or angle is reflected. This may be achieved with sufficient index contrasts for (n_2/n_1) and (n_1/n_i) . Because the stop band vanishes at the Brewster angle between n_2 and n_1 , the strategy is to ensure that this angle is not accessible by external plane waves. A projected dispersion diagram, shown in Fig. 2.3, illustrates this concept.

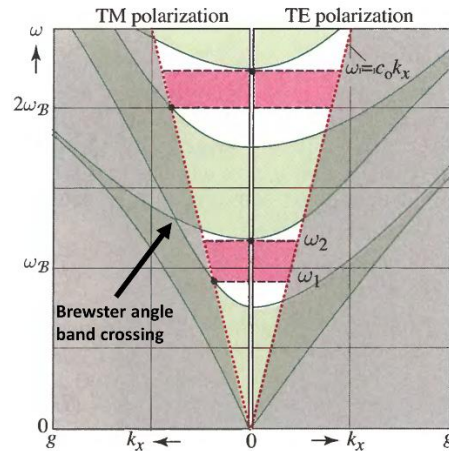


Figure 2.3 – A projected dispersion diagram showing the omnidirectional band gaps of a Bragg mirror. The Brewster angle is inaccessible by external plane waves. Adapted from Ref. [5].

Light entering from the external medium can only access the ω - k_x region that lies above the light line $\omega=c_0k_x$ (shown as red dashed lines). Since the Brewster angle is not accessible in this case, the band gap from ω_1 to ω_2 is omnidirectional. Due to the index-contrast requirements, sometimes it is not possible to achieve a true omnidirectional band. It is, however, much easier to make an omnidirectional band for TE-polarized light only. Figure 2.4 shows the simulated reflectance for a 5.5-period $\text{TiO}_2/\text{SiO}_2$ mirror, with refractive indices of 2.42 and 1.50 for TiO_2 and SiO_2 , respectively. By relaxing the omnidirectional band to just TE-polarized light, an omnidirectional band of ~ 80 nm is achievable using readily available materials.

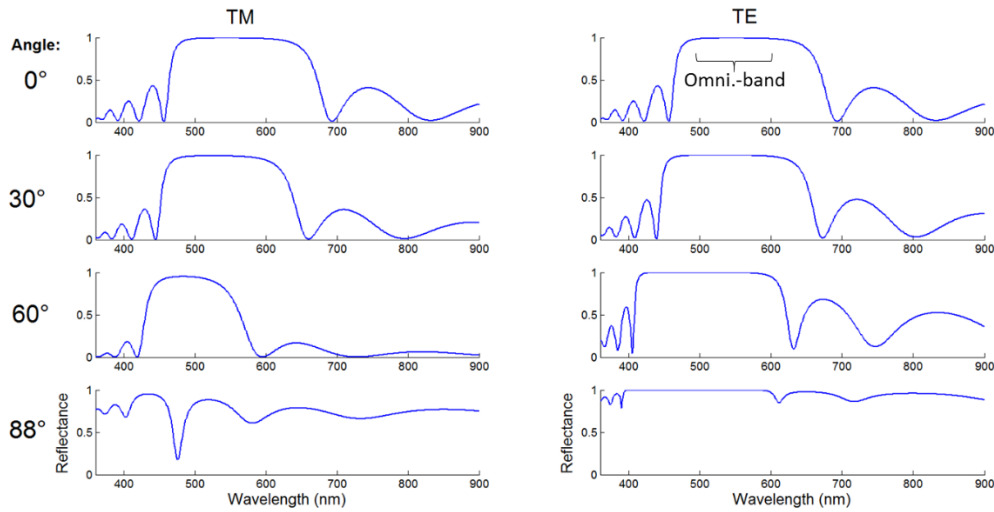


Figure 2.4 – Simulated mirror reflectance for a 5.5-period $\text{TiO}_2/\text{SiO}_2$ mirror, with refractive indices of 2.42 and 1.50 for TiO_2 and SiO_2 , respectively. By relaxing the omnidirectional band to just TE-polarized light, an omnidirectional band of ~ 80 nm is achievable.

2.3 Tapered Bragg waveguides

Figure 2.5 shows a ray-optics representation of light being guided in an air-core tapered Bragg waveguide. As light within the omnidirectional band of the cladding mirrors propagates towards the narrow end of the taper, it approaches cutoff, and

is adiabatically transformed into a vertical cavity resonant mode [1]. Neglecting penetration into the mirrors, cutoff for a guided mode occurs at a core thickness:

$$\delta_c = m\lambda_0/2 \quad , \quad (2.9)$$

where m is integer mode order ($m=1,2,3\dots$) and λ_0 is the free space wavelength. This condition is identical to the Fabry-Perot modal condition, as the waveguide may be viewed as a Fabry-Perot cavity of varying thickness. This condition may be used to map the spatial dispersion of polychromatic light radiated from the taper.

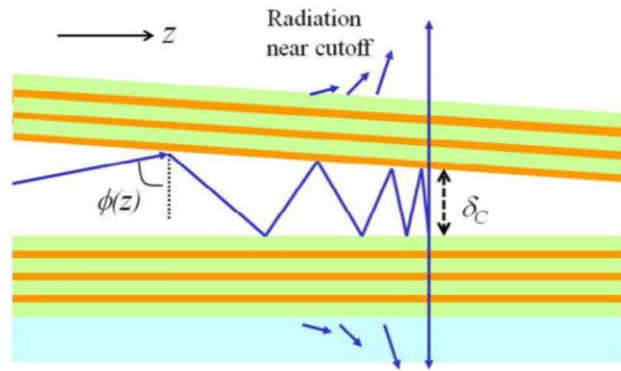


Figure 2.5 – A ray-optics representation of light being guided in an air-core tapered Bragg waveguide. As light within the omnidirectional band of the cladding mirrors propagates towards the narrow end of the taper, it approaches cutoff, and is adiabatically transformed into a vertical cavity resonant mode. Adapted from Ref. [7].

Something the ray-optics perspective neglects is that the mode propagation constant (see Eq. (2.3)) varies rapidly as cutoff is approached, resulting in strong back-reflection of guided light, and causing a standing wave to form [1]. In order to implement a high-resolution spectrometer with these tapers, near-vertically radiated light should be selectively collected to the detector. This is achieved by placing a low-NA optic between the taper and the sensor.

2.3.1 Vertical Fabry-Perot cavity model

Neglecting back-reflection and standing-wave effects, the wavelength resolution of the taper spectrometer can be approximated as [7]:

$$d\lambda \approx \frac{z_p}{D_T} + \frac{\lambda}{m\pi(\sqrt{R}/(1-R))} , \quad (2.10)$$

where m is the vertical mode order ($m=1,2,3 \dots$), z_p is the effective detector array pixel size (accounting for magnification), R is the normal-incidence reflectance of the cladding mirrors, and the spatial dispersion imparted by the taper is given by:

$$D_T = \frac{\Delta z}{\Delta \lambda} = \frac{\Delta z}{\Delta \delta} \frac{\Delta \delta}{\Delta \lambda} \approx \left(1/S_T \right) \left(K + m/2 \right) , \quad (2.11)$$

where S_T is the absolute value of the taper slope, δ is the air-core thickness, and K is a phase-shift coefficient [8] accounting for field penetration into the cladding mirrors at normal incidence.

Using a hard-mirror approximation, the free spectral range (FSR) in terms of wavelength can be expressed as $\delta\lambda_{FSR} \sim \lambda/(m+1)$. Therefore, higher-order modes have higher spatial dispersion and resolution, but at the expense of reduced FSR. Since the omnidirectional bandwidth of the cladding mirrors is already a limiting factor for the operating range, it is sufficient that the FSR exceeds the omnidirectional bandwidth.

2.3.2 Effective-index transfer matrix model

The vertical Fabry-Perot cavity model gives a good approximation of some key taper aspects; however, it neglects aspects such as back-reflection and standing waves. Using an effective-index transfer matrix model takes these details into account. By applying a transfer-matrix model to the cladding layers, the complex refractive index is estimated for a given mode and range of core heights. A core height δ_i gives an effective index [7]:

$$N_i = n_i - \alpha_i \left(\frac{\lambda_0}{4\pi} \right) , \quad (2.12)$$

where $n_i = \sin \phi$ (see Fig. 2.5) and α_i is the intensity attenuation factor.

The tapered slab waveguide is replaced by a stack of effective index layers in the z-direction, as illustrated in Fig. 2.6. For each layer, the core thickness and complex mode index of that layer are used to determine the effective index for that layer.

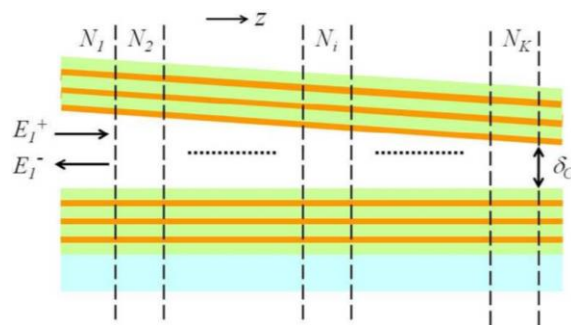


Figure 2.6 – A schematic illustration of the effective-index transfer matrix model. N_i is the complex modal effective index for corresponding mirror separation δ_i . Adapted from Ref. [7]

The input medium is given an effective index of 1, while the output medium is given the imaginary part from the layer just before cutoff. Transfer-matrices are used to determine forward and reverse field amplitudes along the waveguide axis. The step size of the layers along z are chosen to be relatively coarse near the wide end of the taper, and made smaller near cutoff to resolve the standing-wave features [7].

The model from reference [7] was adapted for the tapers studied here, and example code is provided in Appendix A. Figure 2.7 shows a simulation of radiated power of guided modes versus position, for TE-polarized light of mode order $m = 2$. The taper employs 5.5-period $\text{TiO}_2/\text{SiO}_2$ QWS Bragg reflectors centred at 550 nm and has a $0.7 \mu\text{m}/\text{mm}$ taper slope.

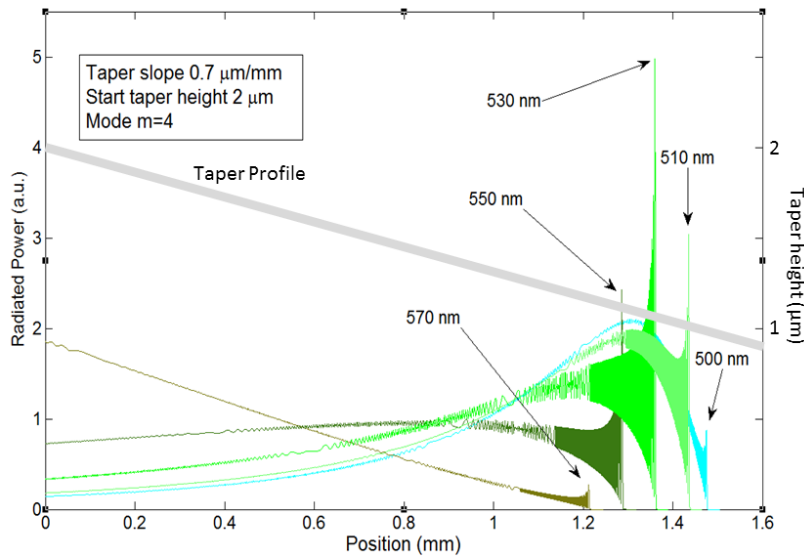


Figure 2.7 – Simulation of radiated power of guided modes versus position, for a taper with a slope of $0.7 \mu\text{m}/\text{mm}$ and TE-polarized light of mode order $m = 4$. Light reaches cutoff for wavelengths between $\sim 500 \text{ nm}$ and $\sim 570 \text{ nm}$. Blue-cyan-green light is well-guided far from cutoff, while orange-red light outside of the omnidirectional band is not well-guided in the taper.

Light with wavelengths between ~ 500 nm and ~ 570 nm is subject to the omnidirectional cutoff mechanism described above. Blue-cyan-green light (i.e. wavelengths just below ~ 500 nm) is well-guided at the wide end of the taper, where guided rays are far from cutoff and have high incident angles on the mirrors. However, low normal-incidence mirror reflectance at these wavelengths causes the light to gradually leak as cutoff is approached. In contrast, orange-red light outside of the omnidirectional band (i.e. wavelengths above ~ 570 nm, see Fig. 2.4) is not well guided, even at the wide end of the taper.

Increasing the taper slope is beneficial to maximizing the operating range of the device, and also helps to even out the radiated power versus wavelength. Figure 2.8 shows the radiated power of guided mode versus position, this time for a device with a $2 \mu\text{m}/\text{mm}$ taper slope.

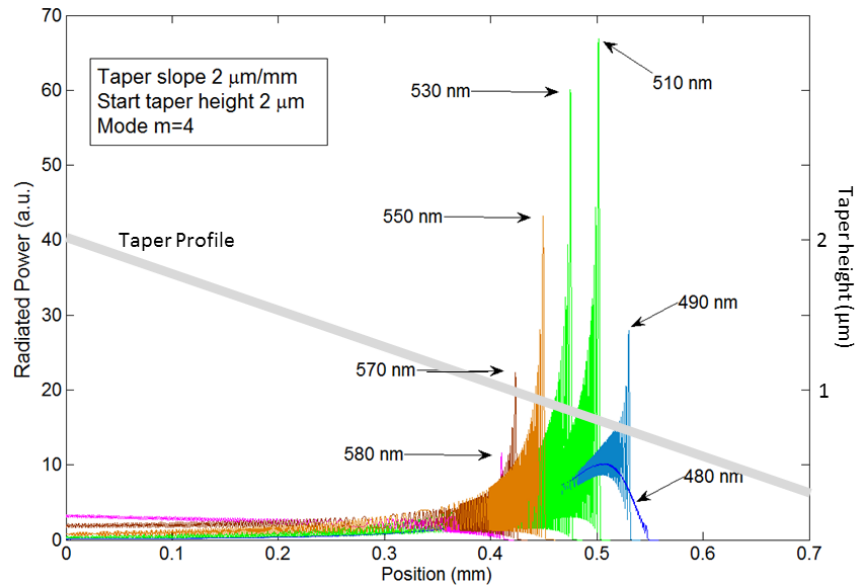


Figure 2.8 – Simulation of radiated power of guided modes versus position, for a taper with a slope of $2 \mu\text{m}/\text{mm}$. The increased taper slope helps to increase the operating range, and also to even out the radiated power versus wavelength.

The increase in taper slope has increased the operating range to ~ 490 nm to ~ 580 nm (i.e. approximately the omnidirectional band), as well as improving the leakage of blue-cyan-green light approaching cutoff. Of course, the cost of a higher taper slope is lower spatial dispersion (and therefore lower wavelength resolution).

2.4 Delamination buckles

In order to help understand the experimental buckling results in Chapter 3, a brief overview of buckling delamination theory is provided here. For the case where a patterned low-adhesion layer defines the width of the buckle and the film is under equi-biaxial compression, the behaviour is usually modeled as a plate that is fully clamped at its edges [9]. The different types of possible buckles are shown in Fig. 2.9. The Euler mode is dominant at the start of buckling.

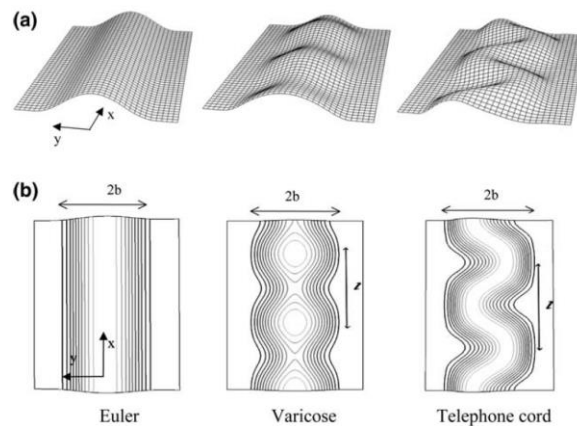


Figure 2.9 – Geometry and buckling analysis of different types of buckles. Adapted from Ref. [9].

The critical compressive biaxial stress σ_c to induce buckling in a strip of width $2b$ is given by [9]:

$$\sigma_c = \frac{\pi^2 E}{12(1-\nu^2)} \left(\frac{h}{b}\right)^2, \quad (2.13)$$

where E is Young's modulus, ν is Poisson's ratio, h is the film thickness, and b is the half-width of the plate. The normal displacement of the Euler buckling mode is given by:

$$\delta(y) = \frac{\delta_{max}}{2} \left(1 + \cos\left(\frac{\pi y}{b}\right)\right), \quad (2.14)$$

where the y -axis is centred on the buckle and the peak buckle height δ_{max} is given by:

$$\delta_{max} = h \sqrt{\frac{4}{3} \left(\frac{\sigma_o}{\sigma_c} - 1\right)}, \quad (2.15)$$

where σ_o is the biaxial compressive stress in the film. Therefore, for compressive film stress $\sigma_o \gg \sigma_c$, the peak buckle height is approximately proportional to the buckle width. This means that the tapered hollow channels have an approximately linear taper for both width and height [1].

2.5 Fluorescence

To help facilitate the discussion of fluorescence pertaining to experimental results in Chapter 6, a short introduction to fluorescence theory is included here. Fluorescence, a form of luminescence, is the emission of light by a substance that

has absorbed light. A Jablonski diagram (shown in Fig. 2.10) is a useful tool for describing the absorption and emission process.

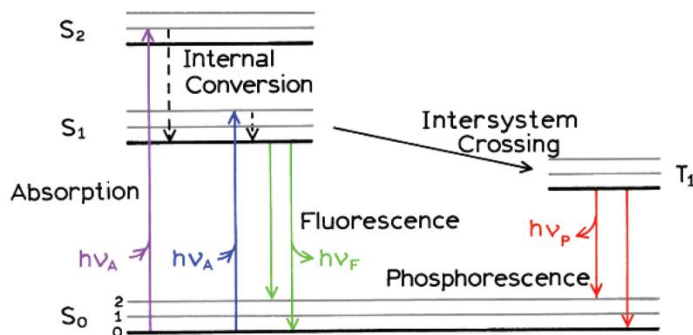


Figure 2.10 – A Jablonski diagram, adapted from Ref. [10]

After light absorption, a fluorophore is excited to either the S₁ or S₂ vibrational state. This is followed by a rapid relaxation to the lowest vibrational level of S₁. Because of this, fluorescence emission is usually from the lowest energy vibrational state of S₁ [10]. As a result, the fluorescence emission spectrum is independent of excitation energy.

Upon emission, the fluorophore typically returns to a higher excited vibrational ground state. This, in addition to internal conversion and other effects, causes the energy of the emission to be less than that of the absorption. The difference between the maxima of the absorption and emission spectra is referred to as the Stokes shift. Figure 2.11 shows the absorption and emission spectra of yellow-green (505 nm Ex/515 nm Em) fluorescent microspheres (FluoSpheres, Invitrogen). The ~10 nm difference between the peak absorption of ~505 nm and the peak emission of ~515 nm is the Stokes shift for these particular fluorophores.

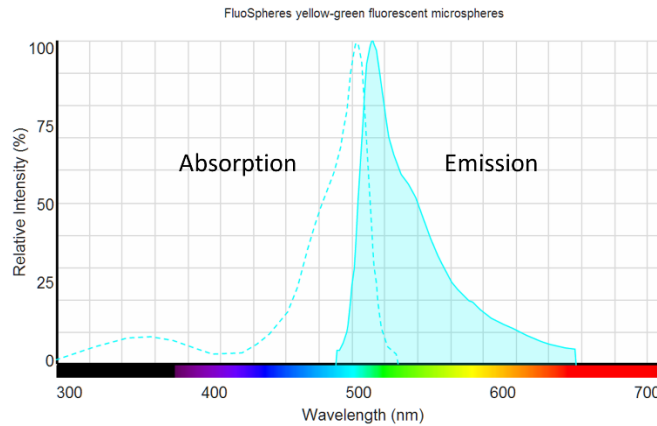


Figure 2.11 – Absorption and emission spectra for yellow-green fluorescent microspheres (FluoSpheres, Invitrogen) [11].

The emission spectrum of the FluoSpheres is a near mirror-image to that of the absorption spectrum. This comes from the fact that, for many fluorophores, the vibrational structure of the ground and excited states are very similar. As a result, similar transitions are favoured in both the absorption and emission of light.

2.6 Works Cited

- [1] N. Ponnampalam and R. G. DeCorby, “Out-of-plane coupling at mode cutoff in tapered hollow waveguides with omnidirectional reflector claddings.,” *Opt. Express*, vol. 16, no. 5, pp. 2894–908, Mar. 2008.
- [2] T. Tamir, “Leaky waves in planar optical waveguides,” *Nouv. Rev. d’Optique*, vol. 273, 1975.
- [3] A. Yariv and P. Yeh, *Optical Waves in Crystals: Propagation and Control of Laser Radiation (Wiley Series in Pure and Applied Optics)*. Wiley-Interscience, 2002, p. 604.
- [4] P. Yeh and A. Yariv, “Bragg reflection waveguides,” *Opt. Commun.*, vol. 19, no. 3, pp. 427–430, Dec. 1976.
- [5] B. E. A. Saleh and M. C. Teich, *Fundamentals of Photonics (Wiley Series in Pure and Applied Optics)*. Wiley-Interscience, 2007, p. 1200.

- [6] P. Yeh, *Optical Waves in Layered Media (Wiley Series in Pure and Applied Optics)*. Wiley-Interscience, 2005, p. 416.
- [7] R. G. DeCorby, N. Ponnampalam, E. Epp, T. Allen, and J. N. McMullin, “Chip-scale spectrometry based on tapered hollow Bragg waveguides,” *Opt. Express*, vol. 17, no. 19, pp. 16632–16645, Sep. 2009.
- [8] S. Weidong, L. Xiangdong, H. Biqin, Z. Yong, L. Xu, and G. Peifu, “Analysis on the tunable optical properties of MOEMS filter based on Fabry–Perot Cavity,” *Opt. Commun.*, vol. 239, no. 1–3, pp. 153–160, Sep. 2004.
- [9] M.-W. Moon, K.-R. Lee, K. H. Oh, and J. W. Hutchinson, “Buckle delamination on patterned substrates,” *Acta Mater.*, vol. 52, no. 10, pp. 3151–3159, Jun. 2004.
- [10] J. Lakowicz, “Introduction to fluorescence,” *Princ. Fluoresc. Spectrosc.*, pp. 1–26, 1999.
- [11] “FluoSpheres® Carboxylate-Modified Microspheres, 0.04 μm , Yellow-Green Fluorescent (505/515), 5% solids - azide free,” 2013. [Online]. Available: <http://www.lifetechnologies.com/order/catalog/product/F8795>. [Accessed: 02-Dec-2013].

3 Fabrication of tapered hollow Bragg waveguides

3.1 Introduction

This chapter focuses on the development of fabrication processes for tapered hollow Bragg waveguides operating in the visible range. Previously, our group employed a-Si/SiO₂ Bragg cladding mirrors for operation in the near-infrared range [1]. Due to low absorption for wavelengths longer than approximately 300 nm and relatively high refractive index contrast [2], SiO₂ and TiO₂ were chosen to form Bragg claddings in the visible band. It should be noted that the material choice here is one of practicality, with SiO₂ and TiO₂ being the best choices readily available. An alternative material pairing, such as SiO₂ and GaP, has a higher index contrast [3] and could potentially create an operational band spanning nearly the entire visible range. The TiO₂/SiO₂ multilayers were deposited using either electron beam (e-beam) evaporation or sputter deposition.

Tapers were assembled using two different techniques: buckling self-assembly and a wafer-bonding process. Previously, our group developed a buckling self-assembly process for hollow waveguides on a chalcogenide glass platform, using commercially available polymers [4].

More recently, we translated this process to a silicon-based platform, utilizing a-Si/SiO₂ multilayers [1]. The focus of the present research was on the extension of the buckling technique to TiO₂/SiO₂ multilayers.

In addition to the buckling self-assembly process, tapers were also fabricated using a wafer-bonding process. Recently, we described the development of visible-band tapered waveguides using this wafer-bonding technique [5]. The development of this wafer-bonding process will also be discussed in this chapter.

3.2 Electron beam evaporation of $\text{TiO}_2/\text{SiO}_2$ Bragg mirrors

The mechanism for e-beam evaporation is the evaporation or sublimation of a source material by heating from a beam of electrons. A schematic of a typical e-beam evaporation system is shown in Fig. 3.1.

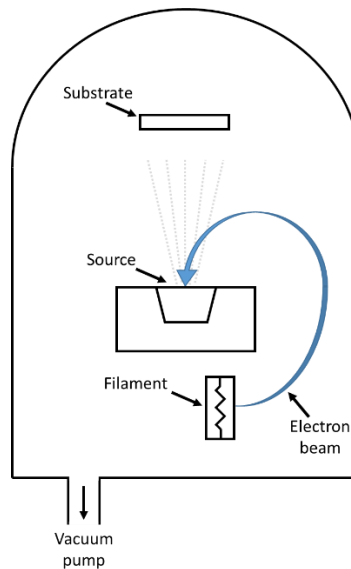


Figure 3.1 – Schematic of a typical electron beam evaporation system. A magnetic field guides an electron beam to a source material, which evaporates or sublimates upon heating. The material is deposited on the substrate above.

The source material is typically held in a crucible liner (such as copper or tungsten), which is then placed in a water-cooled copper hearth. A hot filament

thermionically emits a stream of electrons, which is then guided by the magnetic field of a permanent magnetic, and subsequently hits the source material. Once sufficiently heated, the source material either evaporates or sublimates into vapour phase, condensing on the substrate above.

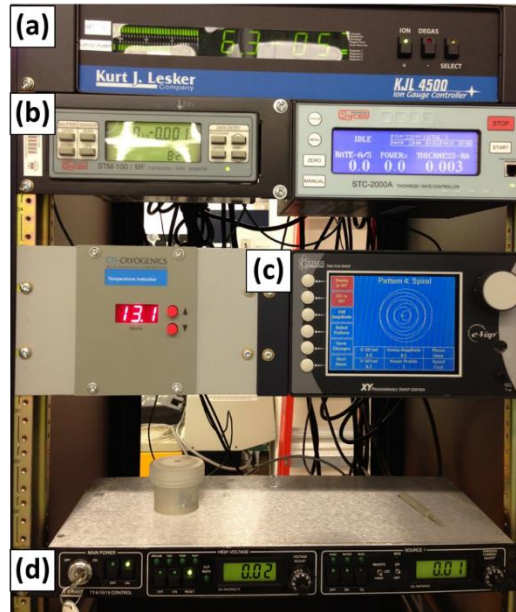


Figure 3.2 – Photo of control panel for e-beam evaporation system. (a) Ion gauge controller (KJL 4500), (b) deposition rate controllers (Sycon STM-100 and STC-2000A), (c) current sweep controller (MDC eVap Programmable X-Y sweep), (d) Voltage and current control.

A six pocket e-beam evaporator system was used to deposit $\text{TiO}_2/\text{SiO}_2$ multilayer films. Two copper crucibles filled with SiO_2 and a tungsten crucible filled with TiO_2 were used as sources. Before deposition, the system is roughed to ~ 100 mTorr by a scroll pump, and then pumped further with a cryopump to a base pressure of $\sim 5 \times 10^{-7}$ Torr. Figure 3.2 shows a photo of the control panel for the e-beam evaporator. An ion gauge is used to monitor the system pressure during deposition. In order to ensure stoichiometry, TiO_2 layers were deposited in an

oxygen rich environment at $\sim 5 \times 10^{-5}$ Torr. Two quartz crystal microbalances are positioned near the substrate within the chamber, allowing for real-time thickness monitoring using thickness controllers (Sycon STM-100 and STC-2000A). During deposition, a programmable current sweep controller (MDC eVap Programmable X-Y sweep) was used to change the position or motion of the electron beam over the source material. This prevents the e-beam from drilling a hole into the source, which is especially important for SiO_2 , as it is sublimated rather than evaporated.

The controlled buckling process (see section 3.4) relies on the top mirror being compressively stressed. Typically, it is difficult to evaporate TiO_2 films with high compressive stress [6]. Reactive sputtering is a more promising method for creating high compressive stress and was therefore chosen for depositing mirrors for buckling self-assembly. Bragg mirrors deposited in the e-beam evaporator, on the other hand, were used for manually assembled slab waveguide tapers (see section 3.5). Deposition parameters for $\text{TiO}_2/\text{SiO}_2$ Bragg mirrors deposited in the e-beam evaporator are listed in Table 3.1.

Table 3.1 – Deposition parameters for $\text{TiO}_2/\text{SiO}_2$ Bragg mirrors deposited in the e-beam evaporator.

	Dep. Rate ($\text{\AA}/\text{s}$)	Pressure (μTorr)	Source Current (A)	Target Layer Thickness (nm)
TiO_2	0.6	50	0.13	61
SiO_2	3	1 – 2	0.05	93
<ul style="list-style-type: none"> • O_2 gas flow during TiO_2 deposition • Base Pressure: $0.5 \mu\text{Torr}$ 				

A variable angle spectroscopic ellipsometer (VASE, J.A. Woollam) was used to measure the reflectance of TiO₂/SiO₂ multilayers deposited in the e-beam evaporator. The measured and theoretical reflectance (using transfer-matrix theory) of a 6.5-period TiO₂/SiO₂ Bragg mirror at 20° incident angle and for TE-polarization is shown in Fig. 3.3(a). Also, a spectrophotometer (Lambda 900, Perkin Elmer) was used to measure the transmittance of a 6.5-period TiO₂/SiO₂ mirror on a glass substrate. Figure 3.3(b) shows the measured and theoretical transmittance at normal incidence. Data was fitted using a fixed +0.02 offset to the Kim dispersion formula [7], with assumed layer thicknesses of 60 nm and 91.5 nm and refractive indices of ~2.33 and ~1.46 for TiO₂ and SiO₂, respectively. These thicknesses and refractive indices are consistent with the expected layer thicknesses and indices. Additionally, a contact profilometer was used to measure the total thickness of the multilayer stack to be ~980 nm, in good agreement with the target thickness of 985 nm and the fitted thickness of 969 nm.

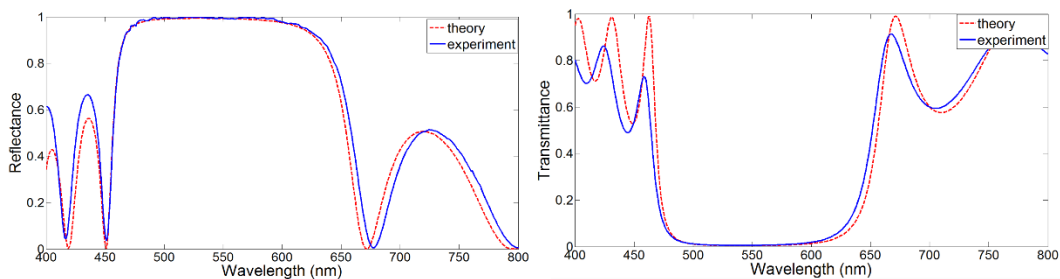


Figure 3.3 – (a) Theoretical and experimental reflectance of evaporated TiO₂/SiO₂ mirrors for TE-polarized light at a 20 degree incident angle. (b) Normal Incidence transmittance of the TiO₂/SiO₂ mirrors. Data was fitted using a fixed +0.02 offset to the Kim dispersion formula [7] and layer thicknesses of 60 nm and 91.5 nm, resulting in refractive indices of ~2.33 and ~1.46 at 550 nm, for TiO₂ and SiO₂, respectively.

3.3 Sputter deposition of TiO₂/SiO₂ Bragg Mirrors

Sputter deposition is an alternative physical vapour deposition (PVD) technique to e-beam evaporation, offering greater flexibility in both material choice as well as film composition. Sputtering occurs when energetic particles collide with a source material (or target), causing atoms to be ejected from its surface. In sputter deposition, ionized gas atoms (typically Argon) are used for bombardment of the target.

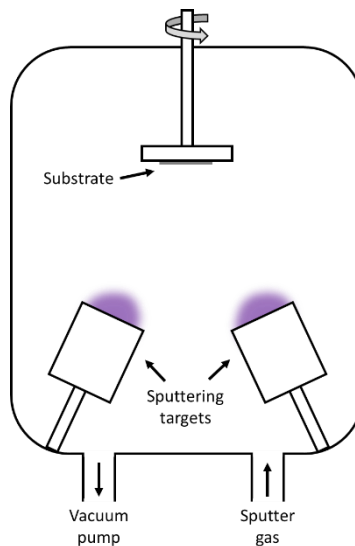


Figure 3.4 – Schematic of a typical magnetron sputtering system. A co-sputtering configuration is shown, with substrate rotation. When a potential is applied, the substrate acts as the anode and the target acts as the cathode. Sputtered source material is deposited on the substrate.

Figure 3.4 shows a schematic of a typical magnetron sputtering system. A voltage is applied, such that the target becomes the cathode and the substrate becomes the anode. The collision of a high-energy electron with an Argon atom leads to electron impact ionization, forming two low-energy electrons and an Argon ion. Argon ions are accelerated towards the target, causing sputtering at

the target surface. Occasionally, the collision of an Argon ion will lead to secondary electron emission, resulting in a secondary electron being accelerated away from the cathode. These secondary electrons help to sustain the glow-discharge created by inelastic collisions between particles. For magnetron sputtering, a strong magnetic field is used to confine these electrons near the target, increasing the occurrence of electron impact ionization events. This enables deposition at lower pressures as well as high deposition rates [8].

The system used for sputter deposition was a commercial planar magnetron sputtering system (Kurt J. Lesker) with three sources and co-sputtering capabilities. For a $\text{TiO}_2/\text{SiO}_2$ multilayer film, an n-doped silicon target and a titanium target are mounted onto 3" diameter sputtering guns. A mechanical roughing pump evacuates the chamber to a pressure of ~ 300 mTorr, after which a cryopump takes over, pumping the system to a base pressure of $\sim 2 \times 10^{-6}$ Torr. A substrate heater heats the substrate to ~ 170 °C and, additionally, the substrate is rotated during deposition to improve film uniformity.

Shown in Fig. 3.5 is an image of the control panel for the sputtering system. A multi-gauge controller (Kurt J. Lesker) monitors pressure readings from a convectron gauge (Torr range), baratron gauge (mTorr range), and ion gauge (μTorr range). A multigas mass flow controller (MKS 647C) was used to supply 50 sccm of Ar, as well as 4.0 sccm and 3.5 sccm of O_2 for TiO_2 and SiO_2 layers, respectively.

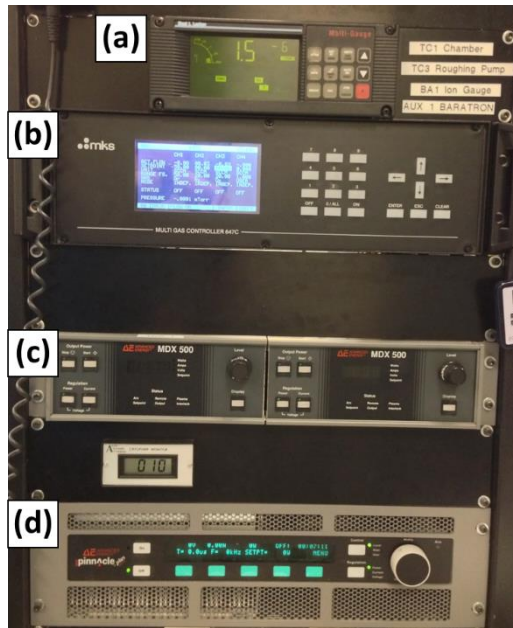


Figure 3.5 – Image of control panel for sputtering system. (a) Pressure gauges (convectron, baratron, ion), (b) MKS mass flow controllers, (c) DC magnetron power supplies, (d) pulsed DC power supply.

Oxygen flow must be sufficiently high to ensure stoichiometry of the oxide layer, while being low enough such that the target is not ‘poisoned’ [9] by the formation of an oxide on its surface. The use of a pulsed DC power supply (AE Pinnacle Plus+) helps to eliminate charge build-up on the target by periodically reversing the potential across the target for a short time. During this ‘off-time’ the target attracts the opposite charge, neutralizing charge build-up at the surface [10].

Careful choice of deposition parameters—especially frequency, off-time, pressure, and oxygen flow rate—is necessary to get high quality optical films, sufficient stress, and to maintain a reasonable deposition rate. Table 3.2 summarizes the progression of the TiO₂ sputtering recipe, illustrating the effect of

changing certain parameters. The final recipe achieved an improved deposition rate and film stress, while maintaining good optical quality. The complete sputter deposition parameters used for the TiO₂/SiO₂ multilayers are summarized in Table 3.3. The tensile stress in the TiO₂ layers is not ideal, as it reduces the overall stress of the multilayer film. However, the relatively high compressive stress of the SiO₂ layers helps to compensate. A SiO₂ monolayer of ~750 nm was measured to have a compressive stress of ~-229 MPa.

Table 3.2 – Compressive stress and deposition rate of TiO₂ monolayer, for different deposition parameters. Stress was measured using a Flexus film stress measurement system.

Dep. Rate (nm/min)	Pressure (mTorr)	Temp. (°C)	O ₂ Flow (sccm)	Power (W)	Pulse Freq. (kHz)	Off-time (μs)	Stress (MPa)
1.3	4	150	5	300	150	2.9	~207
1.9	4	150	4	300	150	2.9	~185
3.4	3	150	4	300	150	2.9	~167
2.6	4	150	4	300	60	5	~314
7.5	3	150	4	300	60	5	~103
7.4	2.7	150	4	300	60	5	~80
2.6	2.7	150	4	300	60	3	~115
4.4	2.6	150	4	300	60	3.5	~65
6.0	2.6	170	4	300	60	3.5	~50

Table 3.3 – Deposition parameters for TiO₂/SiO₂ Bragg mirrors deposited by reactive sputtering.

	Dep. Rate (nm/min)	Pressure (mTorr)	O ₂ Flow (sccm)	Burn-in time (min)	Power (W)	Pulse Freq. (kHz)	Off-time (μs)	Bias (V)
TiO ₂	6	2.6	4.0	4	300	60	3.5	~325
SiO ₂	16.7	4.5	3.5	5	200	150	0.8	~470
• Base Pressure: 2 μTorr			• Argon flow: 50 sccm			• Temp: 170 °C		

A 5.5-period $\text{TiO}_2/\text{SiO}_2$ Bragg mirror with stop band centered at 550 nm was sputtered onto a quartz substrate. For modeling, standard dispersion models were used for SiO_2 and a slightly modified version of the dispersion relation from Ref. [7] for TiO_2 . The validity of these models was verified using VASE reflectance and spectrophotometer transmittance measurements. Figure 3.6(a) shows the experimental and fitted reflectance of the mirror, for a 20° incident angle and TE-polarization. Similarly, Fig 3.6(b) gives the normal-incidence transmittance of the mirror. Using assumed layer thicknesses of 59 nm and 90 nm, the refractive index for a 550 nm wavelength was estimated to be ~ 2.42 and ~ 1.50 for TiO_2 and SiO_2 , respectively.

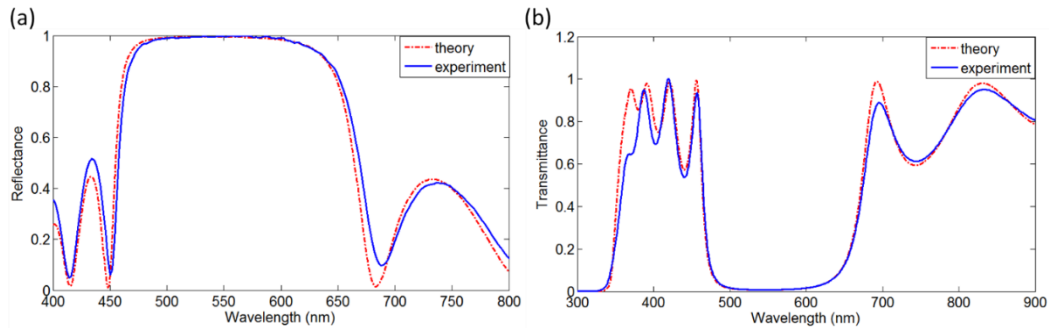


Figure 3.6 – (a) Theoretical and experimental reflectance of sputtered $\text{TiO}_2/\text{SiO}_2$ mirrors for TE-polarized light at a 20 degree incident angle. (b) Normal incidence transmittance of the $\text{TiO}_2/\text{SiO}_2$ mirrors. Data was fitted using a fixed +0.11 offset to the Kim dispersion formula [7] and layer thicknesses of 59 nm and 90 nm, resulting in refractive indices of ~ 2.42 and ~ 1.50 at 550 nm, for TiO_2 and SiO_2 , respectively. Adapted from Ref. [11].

Using a contact profilometer, the total multilayer thickness near the centre of the wafer was measured to be ~ 792 nm. The total thickness used in the model is 804 nm, a discrepancy of 1.5%. The main cause of this is likely due to a difference in film thickness between the spot used for the VASE measurement and the spot

used for the profilometer measurement. Slight errors in modeled layer thickness and refractive index also contribute to the disagreement in thickness.

The refractive index of a reactively sputtered SiO₂ monolayer was extracted from VASE reflectance data using a Cauchy fit. A graph comparing the refractive index of our sputtered film to a similar film from the literature [2] is shown in Fig. 3.7. The films both have refractive indices slightly higher than typical SiO₂, which is due to the choice of sputtering parameters. Some previously sputtered SiO₂ monolayers exhibited slightly better optical properties, but at the expense of process stability due to increased arcing events during deposition.

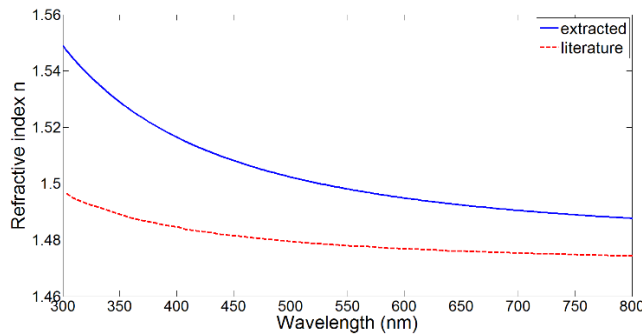


Figure 3.7 – Refractive index of reactively sputtered SiO₂ compared to similarly deposited film in Ref. [2]. Data was extracted from VASE reflectance measurements of SiO₂ monolayer using a Cauchy fit.

The refractive index of reactively sputtered TiO₂ was extracted from the fit in Fig. 3.6. The Kim dispersion relation [7] with a fixed +0.11 offset, was used to model the optical constants of our TiO₂ films, as shown in Fig. 3.8. Their optical properties compare well to similar films found in the literature [2].

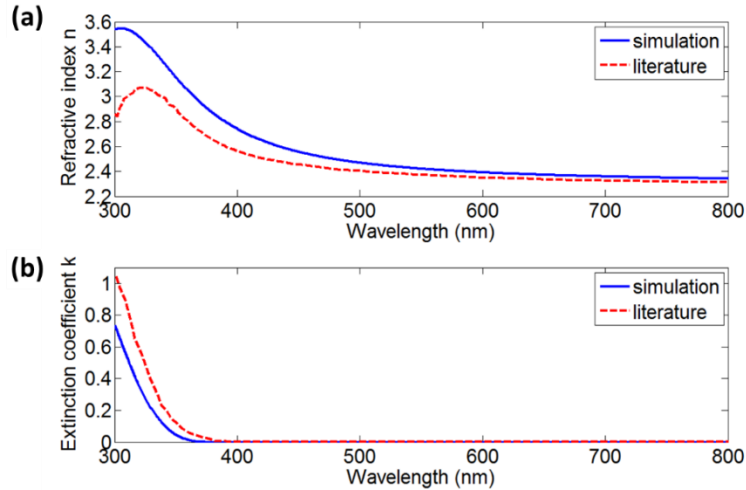


Figure 3.8 – Optical constants for reactively sputtered TiO_2 , determined by fitting R & T measurements of $\text{TiO}_2/\text{SiO}_2$ mirror. The transfer matrix simulation used the dispersion relation from Ref. [7] and a fixed +0.11 offset. (a) Refractive index of TiO_2 , compared to data from Ref. [2] (b) Extinction coefficient of TiO_2 compared to Ref. [2].

Using a Flexus film stress measurement system, the stress of the 5.5-period $\text{TiO}_2/\text{SiO}_2$ mirror on Si was measured to be compressively stressed at ~ -157 MPa. This film was used as the bottom mirror of a buckled waveguide sample (see Section 3.4). The stress in the top mirror is what determines the buckling behaviour of the waveguide sample, however. This stress was measured to be ~ -127 MPa, lower than that of the bottom mirror. This may be due to slightly different sputtering conditions or from interaction with the bottom mirror.

3.4 Hollow waveguides formed by controlled buckling of $\text{TiO}_2/\text{SiO}_2$ Bragg mirrors

In order to adapt the procedure we developed [1] for controlled buckling of a-Si/ SiO_2 multilayers to a $\text{TiO}_2/\text{SiO}_2$ buckling process, it was necessary to carefully consider each process step. For example, piranha cleaning of the Si/ SiO_2 multilayer

was an effective method for cleaning any dirt or debris from the mirror surface. However, since the piranha solution contains sulfuric acid, it will attack the TiO_2 layers and destroy the $\text{TiO}_2/\text{SiO}_2$ film. A simple solution to this problem was to remove the piranha clean step, instead using acetone and isopropyl alcohol (IPA) to remove organics and debris. Fortunately, the rest of the process flow remains relatively unchanged between the buckling of SiO_2/Si and $\text{TiO}_2/\text{SiO}_2$ multilayers.

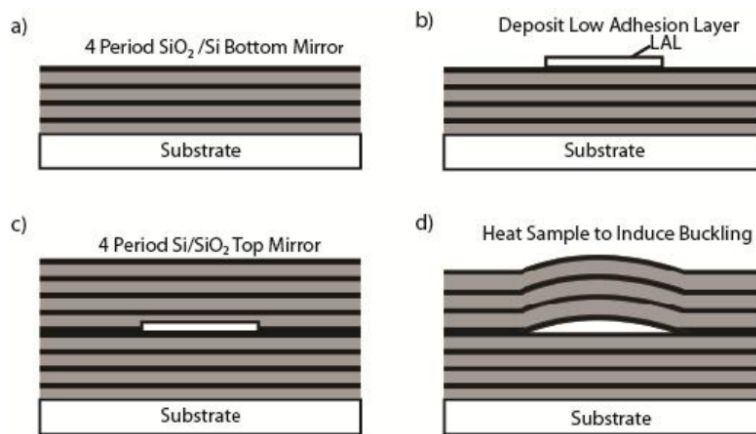


Figure 3.9 – Process flow for buckling assembly of hollow Bragg waveguides. (a) Bragg reflector deposited on substrate, (b) fluorocarbon low adhesion layer deposited and patterned by liftoff, (c) second Bragg reflector deposited, (d) heating to induce buckling in low-adhesion areas. Adapted from Ref. [1].

Figure 3.9 shows the general process flow for buckling assembly of hollow Bragg waveguides. The first step is deposition of the bottom mirror, as described in Section 3.3. Next is the deposition of a low adhesion layer (LAL), which is patterned to define buckling locations. Here, we use fluorocarbon for the LAL. Finally, a compressively stressed top mirror is deposited. By heating the sample, delamination occurs where the LAL is patterned and buckling is induced.

Photolithography with HPR 504 photoresist was used to define the pattern for the LAL. Figure 3.10 shows an image of a Bragg mirror with patterned photoresist features. Arrays of circles and lines define locations for hollow domes and waveguides, respectively. Once patterned with photoresist, the sample was placed in an inductively coupled plasma reactive ion etch (ICP-RIE). A standard conditioning recipe was run for 25 cycles to prepare the chamber for processing.

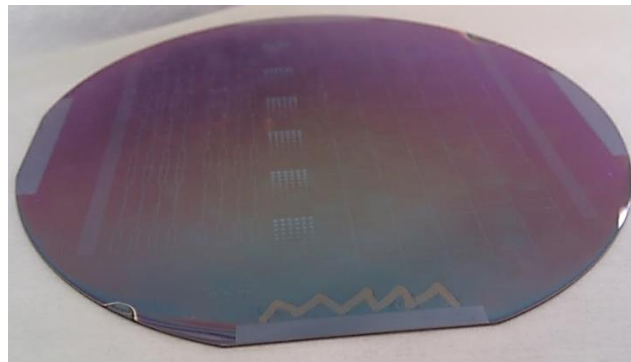


Figure 3.10 – Image of patterned photoresist on Bragg mirror, defining locations for low-adhesion layer. Dome array and tapered waveguide patterns are visible.

The passivation cycle of a Bosch etch recipe was run for 10 seconds, depositing a fluorocarbon layer of $\sim 20\text{-}30$ nm. The fluorocarbon was first deposited onto a blank wafer, which was then scratched to test adhesion. Processing the test wafers appears to further condition the chamber for proper fluorocarbon deposition. Once a test wafer passed the scratch test, the fluorocarbon layer was deposited on the actual sample. Table 3.4 summarizes the key parameters for the fluorocarbon deposition recipe. The liftoff of excess fluorocarbon was accomplished by sonication in acetone for ~ 30 min. In an effort

to improve smoothness of the fluorocarbon layer, the sample was annealed on a hotplate at 100 °C for 1 hour. Finally, the top mirror was deposited by sputtering.

Table 3.4 – Deposition parameters of fluorocarbon deposition recipe for an ICP-RIE tool. A slightly modified recipe for the passivation cycle of a Bosch recipe is used.

Time (s):		R.F. mode: simultaneous 13.56 MHz Generator connected to coil	Platen generator connected to 13.56 MHz: Power ON
Pumpdown	20	Power=300 W (50% tol.)	Electrode 13.56 MHz
Stabilization	10	Matching: Auto	Range: 0-30W (50% tol.)
Process	10	Load=55.7%, Tune=24.4%	Matching: Auto
• Base Pressure: 0.5 mTorr		• C ₄ F ₈ flow: 60 sccm (50% tol.)	• Back cooling enabled

A sample was fabricated with 6-period SiO₂/TiO₂ bottom and top mirrors. By cleaving the wafer into quarters, multiple heating trials were conducted in an attempt to induce buckling in low-adhesion areas. Quarters 1 and 3 were placed on a hotplate and ramped to ~430 °C over 5 minutes. After a total of 10 minutes, the samples were removed from heat. The only result here was a small bubble forming in the alignment window of Quarter 1 after 4 minutes. Quarter 2 was then placed on the hotplate at ~430 °C, at which point all of the domes either popped off or partially buckled, as shown in Fig. 3.11 (d).

In an effort to increase the overall compressive stress of the top mirror, a thin layer of ~59 nm of tungsten was sputtered on top of Quarters 1 and 4. For comparison, a sputtered tungsten monolayer ~400 nm thick was measured to be compressively stressed at ~-2.26 to -2.59 GPa. Therefore, a thin W layer should help to increase compressive stress in the sample. Quarter 1 was again ramped from room temperature to ~400 °C, over 6 minutes. Very minor buckling occurred

while ramping. Additionally, the silver colour of the W film changed to a rainbow hue during heating. Quarter 4 was placed on the hotplate at ~ 420 °C, causing immediate buckling and damage to the waveguides. After 20 seconds, Quarter 4 was removed from heat. The result of this trial is shown in Fig. 3.11 (a)-(c).

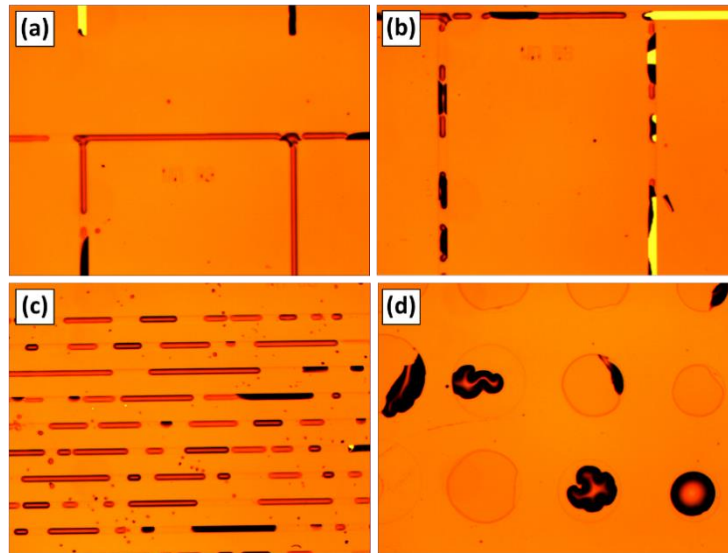


Figure 3.11 – Images of buckling results for $\text{TiO}_2/\text{SiO}_2$ hollow waveguides. (a)-(c) Partially buckled waveguides with thin layer of W on top to help increase compressive stress. Waveguides did not fully buckle and also broke off in some places. (d) Dome cavities either partially buckled or popped off completely.

The waveguides have begun to buckle in many places, but not consistently enough to form fully buckled and functional waveguides. In addition, the sudden thermal shock of the hotplate caused partial delamination of the waveguides in some spots.

From the buckling results above, some conclusions may be drawn. The compressive stress in the $\text{TiO}_2/\text{SiO}_2$ top mirror, while adequate for dome cavities, is insufficient for straight and tapered waveguide features to buckle. The addition

of a thin W layer on top of the TiO₂/SiO₂ mirror is a promising approach. Although the quarter that was already heated did not benefit from a W layer, most of the stress was likely already baked out of the film. The other quarter partially buckled, with damage to features, likely due to the choice of thermal shock rather than ramping. Future work should focus on improving the compressive stress in the TiO₂/SiO₂ films, as well as experimenting further with low-adhesion material choice. Heating procedures should also be refined to improve buckled waveguide yield.

3.5 Air-core slab Bragg waveguide tapers fabricated by wafer bonding

Waveguide tapers were assembled using a wafer-bonding technique, as outlined by the process flow in Fig. 3.12. The TiO₂/SiO₂ mirrors were either sputtered or evaporated onto the substrate: a glass slide, quartz wafer, or a Si wafer. Next, photoresist (SU-8, 2010, Microchem) was diluted with cyclopentanone solvent, allowing for possible thicknesses from 2 μm to 20 μm. The recipes used for fabricating 5.9 μm and 2.1 μm posts are shown in Table 3.5. SU-8 was spun-cast onto the mirror surface of the substrate and patterned to leave rectangular posts (100 μm x 50 μm) and scribe lines at pre-defined locations. A protective layer of HPR 504 was spun-cast onto the substrate prior to dicing. Then, the substrate was diced along these lines into ~3 to 6 mm long pieces. The substrate was diced such that there was a linear array of posts along one of the edges. The posts were

aligned lengthwise and spaced $\sim 150\ \mu\text{m}$ apart. After dicing, acetone and IPA were used to remove the protective photoresist layer.

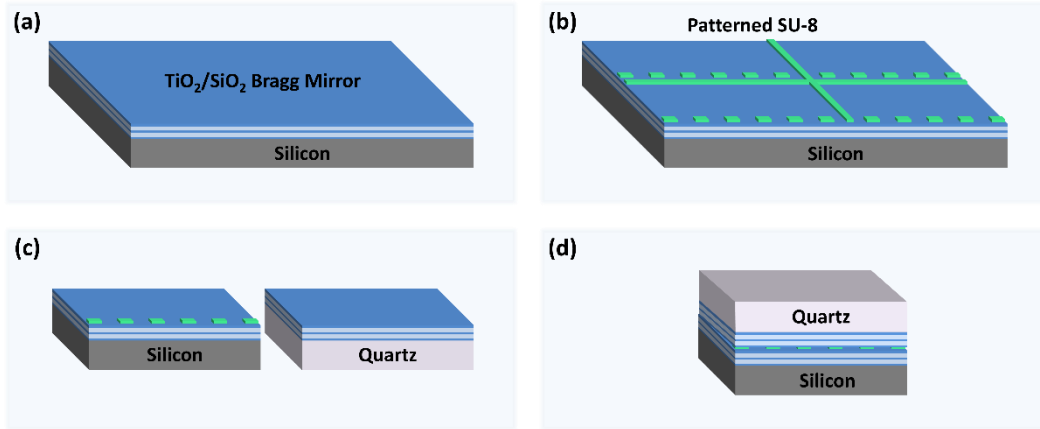


Figure 3.12 – Process flow for wafer-bonding assembly of air-core tapered slab Bragg waveguides. (a) Bragg mirror deposited on substrate, (b) SU-8 spun-cast and patterned onto mirror, (c) substrate diced along predefined lines, (d) a patterned and blank piece clamped and bonded with UV-curable epoxy.

Table 3.5 – Recipe for patterning SU-8 posts of $5.9\ \mu\text{m}$ and $2.1\ \mu\text{m}$ height. The parameters work for a substrate with a TiO₂ top layer. Posts with $2.1\ \mu\text{m}$ height require longer bake times to improve adhesion and a hard bake to repair cracking due to extended bake times.

	(a) $5.9\ \mu\text{m}$ Posts	(b) $2.1\ \mu\text{m}$ Posts
Photoresist	Diluted SU-8 2010 (36% solids)	SU-8 2002
1) Dehydrate wafer:	200 °C – 5 min	
2) SU-8 spinning: (RPM/Ramp/Hold)	500/5s/5s 1100/2s/30s	500/5s/5s 1000/2s/30s
3) Soft bake	95 °C – 2 min	65 °C – 5 min 95 °C – 2 min
4) Exposure	105 mJ/cm ²	90 mJ/cm ²
5) Post-exposure bake	95 °C – 3 min	65 °C – 4 min 95 °C – 10 min 65 °C – 1 min
6) SU-8 development	Time=90s	Time=60s
7) Rinse with IPA	Time=25s	Time=60s
8) Hard bake	–	200 °C – 5 min

Only one of the two pieces in a wafer-bonded taper requires SU-8 posts. The other piece is diced from an unpatterned mirror. For the fabrication of glass-silicon and quartz-silicon tapers, the silicon substrate was chosen for SU-8 patterning. This is because the silicon dicing saw (Disco DAD 321) has a cut width of $\sim 50 \mu\text{m}$, compared to $\sim 325 \mu\text{m}$ for the dicing saw (Diamond Touch) used for glass and quartz. The narrower width allows for greater accuracy when aligning the dicing saw beside a line of SU-8 posts. This prevents possible damage to the post array, as well as providing a smoother, more uniform edge. In the case of quartz-quartz tapers, one quartz substrate is spun-cast, while only half is exposed under a mask aligner.

Finally, a patterned piece and an unpatterned piece were aligned, mirror coatings facing inward, so that the patterned edge was flush with the edge of the other piece. This ensures that the unpatterned piece is propped up by the SU-8 posts along one side, since the glass and Si dicing saws have a cut width mismatch. Plastic tweezers were used to clamp the two pieces together. Using an UV-curable epoxy (NOA-61, Norland) and a needle for application, the two pieces were bonded together along the narrow end of the slab taper.

Figure 3.13(a) shows a schematic illustration of a taper assembled using the wafer-bonding technique. Slab waveguide tapers formed this way were analyzed using optical and scanning electron microscopy (SEM). An SEM image of the end facet (wide end) of a taper is shown in Fig. 3.13(b).

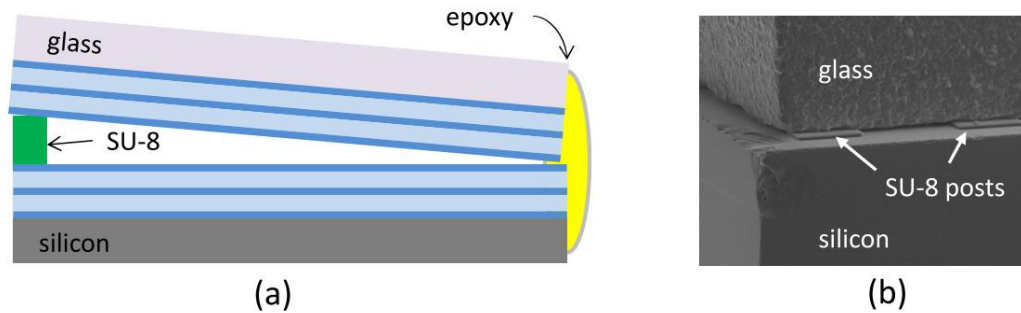


Figure 3.13 – (a) Schematic illustration of a tapered slab Bragg waveguide fabricated by bonding a glass substrate to a patterned Si substrate. (b) SEM image showing the end facet (wide end) of a taper. For scale reference, the spacing between adjacent SU-8 posts is 150 μm . Adapted from Ref. [5].

Wafer-bonded tapers were assembled in a variety of ways. Initially, tapers were fabricated using Si wafers and glass slides as substrates, as shown in Fig. 3.14(a) and 3.14(b). The rigidity of these substrates ensures a highly linear taper slope. However, inclusions in the glass create difficulties in optical experiments, because they cause light to scatter. Alternatively, tapers were fabricated entirely using quartz pieces, as shown in Fig. 3.14(c). The superior optical quality of the quartz compared to the glass helps to reduce light scattering due to inclusions.

One drawback in an all-quartz taper design is that the taper slope is slightly nonlinear, due to the relatively flexible quartz substrates. The taper slope was still approximately linear over the length of an individual mode, however. Tapers were also made using Si and quartz pieces, as shown in Fig. 3.14(d). By replacing one of the flexible quartz pieces with a rigid Si piece, the taper slope becomes much more linear.

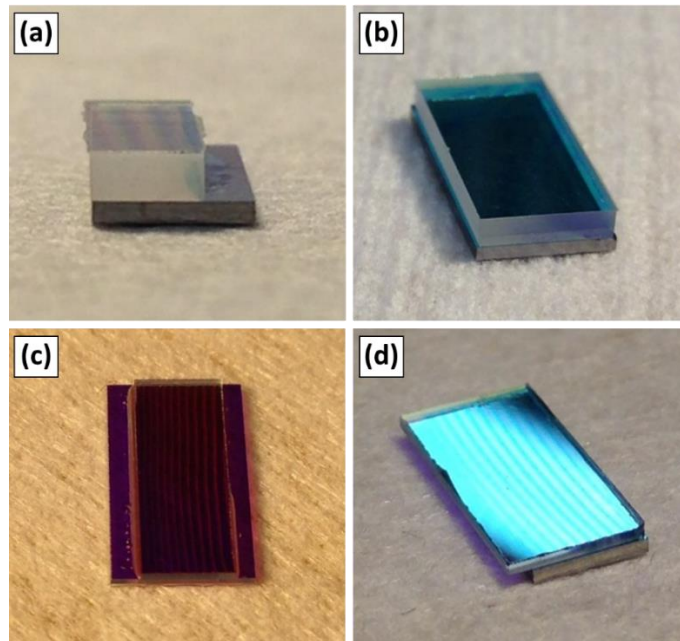


Figure 3.14 – Images of manually assembled tapers with (a) glass and silicon substrates with mismatched length, (b) glass and silicon substrates with matched length, (c) quartz substrates with overhangs at front and back, and (d) quartz and silicon substrates with overhang at front.

Some tapers were fabricated using pieces with a length mismatch, such as a 4 mm long Si piece and a 6 mm quartz piece. This leads to an overhang of the quartz, at one or both ends. One benefit of this configuration is that any scattered light at the end facets is blocked from reaching a camera positioned above the taper. Additionally, this overhang offers functionality as an insertion point for an analyte species into the taper.

3.6 Conclusions

Tapered waveguides were fabricated for operation in the visible range. $\text{TiO}_2/\text{SiO}_2$ mirrors were deposited using both e-beam evaporation and reactive sputter deposition. While both deposition methods produced Bragg mirrors of good

optical quality, sputter deposition is better suited for fabricating buckled hollow waveguides. Initial buckling experiments with TiO₂/SiO₂ films resulted in only minor buckling in the waveguides, indicating that compressive stress in the TiO₂ films may need to be increased further.

We also developed a taper fabrication process by manually assembling slab Bragg waveguide tapers by wafer-bonding. This process has proven to be more reliable and versatile than the buckling self-assembly process. Mirrors may either be evaporated or sputtered onto glass, quartz, or silicon substrates. The taper dimensions are also easy to change, allowed for tailoring to the wavelength range of the mirrors.

3.7 Works Cited

- [1] E. Epp, N. Ponnampalam, W. Newman, B. Drobot, J. N. McMullin, A. F. Meldrum, and R. G. DeCorby, "Hollow Bragg waveguides fabricated by controlled buckling of Si/SiO₂ multilayers," *Opt. Express*, vol. 18, no. 24, pp. 24917–24925, Nov. 2010.
- [2] P. R. Sagdeo, D. D. Shinde, J. S. Misal, N. M. Kamble, R. B. Tokas, a Biswas, a K. Poswal, S. Thakur, D. Bhattacharyya, N. K. Sahoo, and S. C. Sabharwal, "Deposition and characterization of titania–silica optical multilayers by asymmetric bipolar pulsed dc sputtering of oxide targets," *J. Phys. D. Appl. Phys.*, vol. 43, no. 4, p. 045302, Feb. 2010.
- [3] J. Gao, A. M. Sarangan, and Q. Zhan, "Experimental confirmation of strong fluorescence enhancement using one-dimensional GaP/SiO₂ photonic band gap structure," *Opt. Mater. Express*, vol. 1, no. 7, p. 1216, Oct. 2011.
- [4] R. G. Decorby, N. Ponnampalam, H. T. Nguyen, M. M. Pai, and T. J. Clement, "Guided self-assembly of integrated hollow Bragg waveguides.," *Opt. Express*, vol. 15, no. 7, pp. 3902–15, Apr. 2007.

- [5] B. Drobot, A. Melnyk, M. Zhang, T. W. Allen, and R. G. DeCorby, "Visible-band dispersion by a tapered air-core Bragg waveguide," *Opt. Express*, vol. 20, no. 21, pp. 23906–23911, Oct. 2012.
- [6] H.-C. Chen, K.-S. Lee, and C.-C. Lee, "Annealing dependence of residual stress and optical properties of TiO₂ thin film deposited by different deposition methods.," *Appl. Opt.*, vol. 47, no. 13, pp. C284–7, May 2008.
- [7] S. Y. Kim, "Simultaneous determination of refractive index, extinction coefficient, and void distribution of titanium dioxide thin film by optical methods.," *Appl. Opt.*, vol. 35, no. 34, pp. 6703–7, Dec. 1996.
- [8] G. Bräuer, B. Szyszka, M. Vergöhl, and R. Bandorf, "Magnetron sputtering – Milestones of 30 years," *Vacuum*, vol. 84, no. 12, pp. 1354–1359, Jun. 2010.
- [9] J. Sellers, "Asymmetric bipolar pulsed DC: the enabling technology for reactive PVD," *Surf. Coatings Technol.*, vol. 98, no. 1–3, pp. 1245–1250, Jan. 1998.
- [10] W. D. Sproul, D. J. Christie, and D. C. Carter, "Control of reactive sputtering processes," *Thin Solid Films*, vol. 491, no. 1–2, pp. 1–17, Nov. 2005.
- [11] B. A. Drobot, A. D. Melnyk, T. W. Allen, and R. G. DeCorby, "Tapered air-core Bragg waveguide spectrometers for lab-on-a-chip applications," *Proc. SPIE*, vol. 8726, p. 87260V–87260V–7, May 2013.

4 Integration of tapers with microfluidics

4.1 Introduction

Optofluidic LOC systems require the implementation of fluidics to deliver an analyte species to the device. There are a variety of ways to accomplish this, such as PDMS platforms and microfluidic channels [1],[2], buckle delamination [3], or hollow waveguides [4], to name a few. It is desirable to create a high level of integration between the optical and fluidic elements, which often increases the coupling efficiency of the analyte signal. Additionally, on-chip integration of optical elements and fluidic elements in a LOC device helps to reduce the overall size and cost of the device platform [5].

In order to carry out fluorescence experiments with the slab waveguide tapers, several fluidic interfacing methods were explored: PDMS reservoirs, glass capillaries, and direct insertion of fluid into the taper. As well, attempts were made to create a PDMS microfluidic platform directly on buckled hollow waveguide chips.

4.2 PDMS microfluidics integrated on-chip with buckled waveguides

Initial microfluidics efforts focused on creating a separate PDMS microfluidic platform, to which a buckled waveguide chip could be bonded. The PDMS platform consisted of two open wells, each with a microfluidic channel leading to the PDMS-Silicon interface. The buckled waveguide chip is aligned face-down on

the PDMS, such that the end facets of two hollow waveguides line up with the PDMS capillaries. A microscope is used, allowing for relatively simple alignment of the buckled waveguides with the PDMS capillaries. A schematic of the PDMS microfluidic platform is shown in Fig. 4.1.

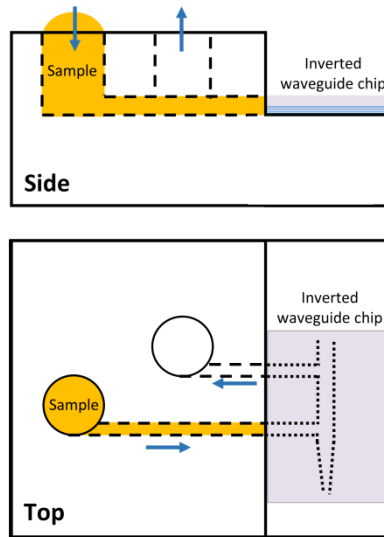


Figure 4.1 – Schematic of a PDMS microfluidic platform for delivering fluid to a buckled waveguide chip. PDMS capillaries connect the inlet and outlet wells to the buckled waveguide channels. The waveguide chip is bonded face-down to the PDMS platform.

The PDMS platform and the hollow waveguide chip are bonded by exposing the PDMS surface to an oxygen plasma, then clamping the platform and chip together once aligned. However, repeated fluid flow trials revealed that the PDMS-Silicon interface of the microfluidics platform is prone to significant leakage. Figure 4.2 shows an image of an attempt to deliver blue fluid from a PDMS well into the buckled waveguides. Leaked fluid is clearly visible near the top-left of the silicon chip. Optical adhesive (NOA 61) was used to try to form a better

seal between the PDMS and the silicon. It proved difficult to avoid plugging the waveguide channels and PDMS capillaries while also forming a complete seal.

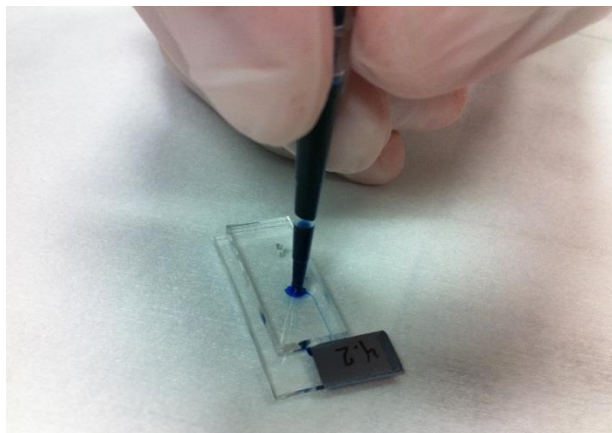


Figure 4.2 – Photo of a PDMS microfluidic platform interfaced with a hollow waveguide chip. Fluid leakage is a major problem at the PDMS-silicon interface.

In an attempt to alleviate the PDMS-silicon leakage problem, the PDMS platform was redesigned to be fabricated directly on top of the silicon waveguide chip. Here, the inlet and outlet wells are positioned at either end of a buckled waveguide, removing the need for PDMS capillaries. Small brass posts of ~ 1.64 mm diameter and ~ 4 mm height were used to define the wells. The bottoms of the posts were dipped in melted Crystalbond 555 and positioned on the waveguide chip before cooling. The Crystalbond prevents the posts from being knocked over during processing in addition to stopping the PDMS from flowing beneath the posts during fabrication. A schematic showing typical placement of posts on a buckled waveguide chip is shown in Fig. 4.3. The posts need to be placed a few millimetres apart so that the PDMS barrier between wells is robust enough to withstand fluid flow trials and handling.

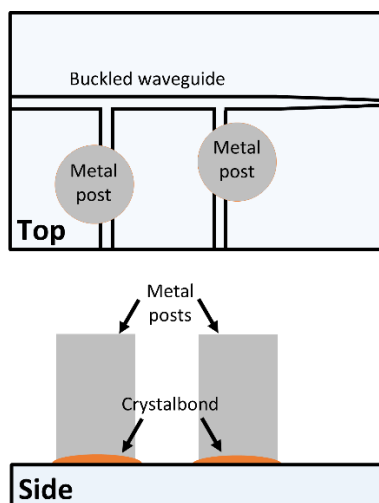


Figure 4.3 – Schematic of metal post placement, defining the inlet and outlet wells of the PDMS fluidics. Crystalbond is used beneath the posts to prevent PDMS from leaking underneath during PDMS pouring.

For the PDMS process, a silanized silicon wafer is put in a PDMS pouring mount. Up to three waveguide chips are placed on the wafer, spaced evenly apart. In some cases, it was beneficial to use Crystalbond to attach the waveguide chips to larger pieces of silicon. The larger surface area helps to prevent delamination of PDMS from the sample and is also easier to handle. The optimal PDMS thickness for connecting syringes and tubing to the wells was obtained using ~20 g of PDMS. After curing the PDMS, the metal posts are carefully removed before the Crystalbond re-solidifies. A razor is used to cut the samples out. Figure 4.4 shows a photo of buckled waveguide chips with PDMS wells integrated on-chip. Partial delamination of the PDMS is visible in non-essential areas for samples 1.03, 1.06, and 1.07.



Figure 4.4 – Photo of hollow waveguide samples with PDMS wells fabricated on top. Partial delamination of non-essential areas is visible for samples 1.03, 1.06, and 1.07. The addition of an oxygen plasma step during fabrication eliminated this problem, shown in samples 1.01, 1.04, and 1.05.

To encourage adhesion, later samples (1.01, 1.04, and 1.05) were exposed to an oxygen plasma just prior to pouring the PDMS. An unforeseen result of this added step was increased adhesion to the posts, making it difficult to remove them without damaging the PDMS. A possible fix to this problem would simply be to expose the sample just before placing the posts.

A variety of fluid flow tests of the on-chip PDMS hollow waveguide samples were performed. For these tests a syringe is connected to a well, either directly with a syringe tip or via tubing. The syringe is then used to attempt to force water into the other well. The results for this vary significantly between samples. In some cases, even high amounts of pressure did not result in fluid reaching the other well. This indicates that the hollow waveguides in these samples may be blocked at some point, perhaps due to a collapse or PDMS blockage. For other samples,

fluid was found to travel from one well to another, at least partially via the hollow waveguides. Repeated fluid flow attempts with food colouring revealed that liquid would sometimes leak under the PDMS when subjected to a high enough fluid pressure. There are also inherent problems with manually exerting the fluid pressure using a syringe. Figure 4.5 is a photograph of a sample with liquid that has leaked under the PDMS between the two wells. For this sample, pressure was gradually increased until fluid appeared in the second well. As pressure was increased further, leakage became visible. The use of Crystalbond during processing results in a slight PDMS overhang in the well. This makes it difficult to confirm whether the initial fluid flow came from the waveguide or was also from leakage.

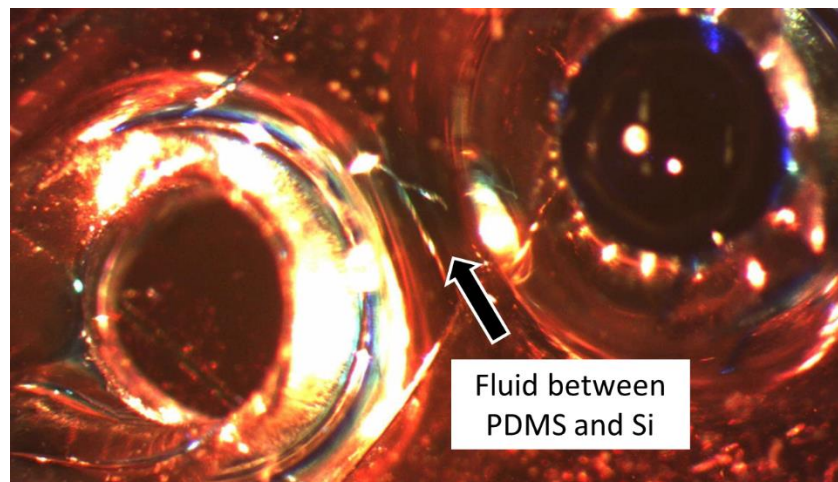


Figure 4.5 – Fluid flow attempt for sample 1.05, in which a syringe was used to force fluid from one well to the other. Fluid has leaked between the silicon substrate and the PDMS layer, due to the pressure exerted at the interface.

Alternatively, some fluid flow trials involved placing a drop of liquid in one well, while using a syringe to create a vacuum in the other. In this case, the

likelihood of fluid leaking under the PDMS is significantly reduced. Almost every sample yielded no result for this test. However, once the syringe was removed from sample 1.05, a small amount of liquid was visible at the end of the hollow waveguide. This result indicates that fluid will flow within the hollow waveguides, however it requires relatively large pressures to do so.

Future work with the on-chip PDMS platform should focus on reducing the force required to pump fluid through the hollow waveguides. This would also reduce the occurrence of fluid leaking under the PDMS. The method for defining the wells has room for improvement. For example, the small posts are difficult to manipulate and place accurately, resulting in a less reliable fabrication process. An alternative fabrication process could involve using photolithography to define the locations of the inlet and outlet ports [6].

4.3 Microfluidic integration for slab waveguide tapers

4.3.1 PDMS reservoirs

PDMS reservoirs were designed for the slab waveguide tapers. A schematic of this design is shown in Figure 4.6. The taper is placed in the PDMS holder, with the wide end pressed against the PDMS wall to form a seal. Ideally, this will restrict the sample fluid to the small reservoir and the inside of the taper. The PDMS reservoirs are fabricated using a similar method to that in Section 4.2. Two rectangular pieces of glass are placed together on a silanized wafer, defining the shape for the PDMS reservoir. Once the PDMS is cured, the glass pieces are

removed and the shape cut out, along with a blank piece of equal size. The two pieces are then exposed to an oxygen plasma and held together under weight for a few hours, forming a permanent bond. Fabrication of PDMS basins is easily customizable, allowing for different basin shapes as well as the incorporation of PDMS microfluidic capillaries.

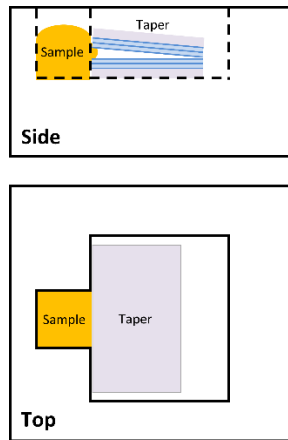


Figure 4.6 – Schematic of PDMS basins used to hold fluid at front of tapered waveguide. This configuration relies on the taper itself to form a quasi-seal for the liquid sample. Capillary action draws a thin layer of fluid beneath the taper, limiting the practical benefits of the PDMS basin setup.

Photographs of fabricated PDMS basins are shown in Fig. 4.7. A different style is shown in Fig. 4.7(a), where PDMS microfluidic capillaries were used instead of a small reservoir for fluid at the front. Figures 4.7(b) shows a slab waveguide taper in its PDMS holder, while Fig. 4.7(c) also shows a similar sample but with a fluorescent dye in its reservoir and under laser illumination. These PDMS reservoirs are significantly easier to fabricate than the on-chip PDMS samples discussed in Section 4.2. There are drawbacks though, similar to those for the microfluidic PDMS platform (Fig. 4.1). As intended, the fluid is initially contained

to the small reservoir and inside the taper. However, over the course of a few minutes the fluid is slowly drawn beneath the taper, forming a thin film of fluid. If the taper has two quartz substrates, it will act as a linear variable filter for this thin analyte film. In order to avoid this, a taper with a silicon substrate should be used.

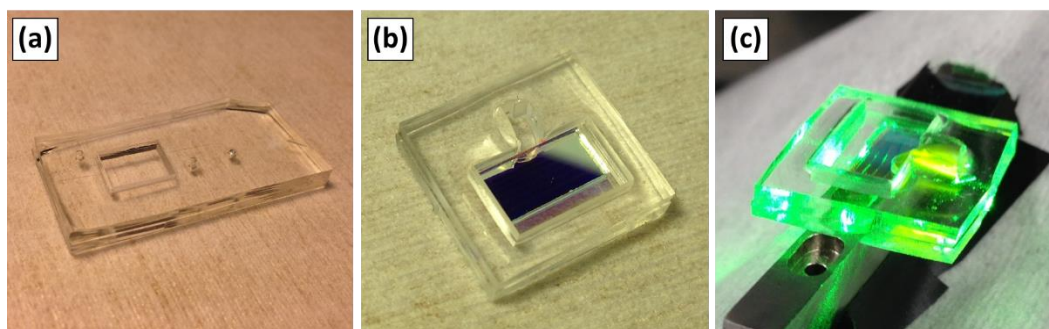


Figure 4.7 – Photos of PDMS reservoirs. (a) PDMS microcapillaries are used to deliver fluid to the wide end of the taper chip. (b)-(c) Slab waveguide tapers are placed against the front edge of the PDMS basins to form a weak seal. The fluid analyte is temporarily confined to the small reservoir at the front.

Another practical drawback of the PDMS reservoirs is that they hold far more fluorescent analyte than is required, contributing additional signal noise. In addition, the reservoirs and tapers are usually permanently contaminated by the analyte. This is especially problematic since the analyte tends to leak beneath the taper. Glass capillaries and integrated fluid platforms are promising alternatives, offering solutions to some of these problems.

4.3.2 Glass capillaries

Glass capillaries were used to hold the sample analytes in some fluorescence experiments. Using capillaries has several advantages compared to the other fluid handling methods covered in this chapter. For example, confining the sample to a

capillary prevents the tapered waveguide from becoming contaminated. This increases the taper's reusability. Glass microcapillaries (Drummond Microcap 10 μL) were cut into ~ 1 cm lengths. The capillaries were then filled with dilutions of fluorescent microspheres and sealed at both ends with an UV-curable epoxy (NOA-61, Norland) to prevent the solutions from evaporating. A capillary is positioned either beneath or along the wide end of a taper, as the schematics in Fig. 4.8 illustrate. With the capillary placed beneath the taper, the taper acts as a conventional linear variable filter. Fluorescence from the taper is spatially filtered into Fabry-Perot resonant modes. Alternatively, the capillary may be placed along the wide end of the taper. In this case, fluorescence within the omnidirectional band of the mirrors is adiabatically transformed from a guided mode to a vertical Fabry-Perot mode at cutoff [7].

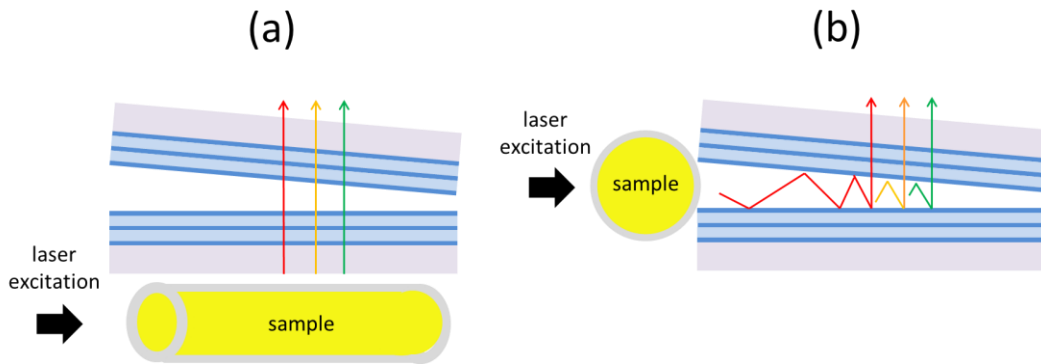


Figure 4.8 – Schematic illustration of a tapered waveguide in a conventional linear variable filter configuration. Sample fluorescence is spatially filtered into Fabry-Perot resonant modes. (b) Schematic illustration of ray guidance in a slowly tapered hollow Bragg waveguide. Fluorescence within the omnidirectional band of the mirrors is adiabatically transformed from a guided mode to a vertical Fabry-Perot mode at cutoff. Adapted from Ref. [8].

The glass microcapillaries offer a simple and effective fluid handling system for fluorescence experiments; however, there are some drawbacks. For example, the optical adhesive used to seal the capillaries exhibits minor fluorescence when under direct laser excitation. This is remedied by ensuring that excitation laser light is focused away from the ends of the capillary. The biggest problem associated with using glass capillaries is that the glass walls are relatively thick, leaving a significant gap between the fluorescent microspheres and the taper end facet. As well, there is an inherent spatial mismatch between the ~ 0.7 mm inner diameter capillary and the ~ 6 μm tall taper opening. This leads to very high signal loss, with only a very small fraction of fluorescence entering guided modes of the tapered waveguide.

4.3.3 Integrated platform for fluid insertion into taper

Instead of using external microfluidics, fluid may be inserted directly into the tapered waveguide itself. One advantage of this is the highly integrated and simplified nature of this setup, as shown in Fig. 4.9. By including an overhang at the wide end of the taper, the application of a fluid sample is simplified, and the amount of stray fluorescence reaching the CCD is reduced. Since the fluorescent microspheres are physically inside the taper cavity, a high fraction of fluorescence enters guided modes of the waveguide. This leads to much higher efficiency compared to when PDMS reservoirs or glass microcapillaries are used.

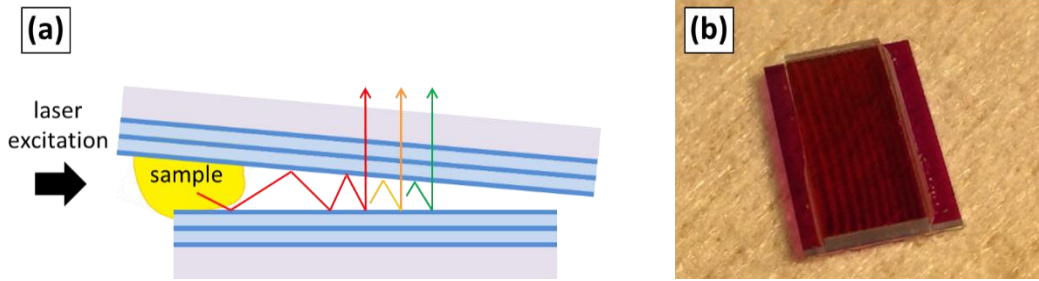


Figure 4.9 – (a) Schematic of fluid insertion using integrated platform. The sample is placed at the wide end of the tapered slab waveguide. (b) A taper with quartz substrates and an overhang at both the wide and narrow ends of the taper. The overhang helps to limit stray fluorescence and facilitates fluid insertion at the wide end.

The fluid is naturally drawn inside the taper towards the narrow end. It is desirable to contain the fluorescent microspheres to the front of the taper, so that vertical cavity modes come exclusively from adiabatically transformed guided modes of the taper. One way to achieve this is to use microspheres with a diameter large enough to prevent infiltration more than part-way into the taper. FluoSpheres with a 4 μm diameter were inserted into the wide end of a taper with starting height of $\sim 5.9 \mu\text{m}$. Here, the FluoSpheres are restricted to the first third of the taper cavity.

In an attempt to restrict smaller microspheres ($\sim 40 \text{ nm}$ diameter) to the wide end of the taper, a long strip of SU-8 was used as a barrier. This was done by leaving the SU-8 dicing line beside the SU-8 posts intact during fabrication of the tapers. Due to defects in the SU-8 line, however, this barrier was insufficient in blocking these smaller microspheres. Therefore, using larger microspheres is a more reliable and practical method for confining the microspheres to the wide end of the taper.

4.4 Conclusions

A variety of microfluidics schemes were investigated for use with buckled waveguides as well as with tapered slab waveguides. For the buckled waveguides, a separate PDMS microfluidics platform and on-chip PDMS fluidics were investigated. Both of these setups suffered from fluid leaking at PDMS-silicon interfaces, and have plenty of room for future refinement. PDMS reservoirs were found to be less than optimal for fluid containment at the front of the taper. They did, however, provide unforeseen functionality for LVF experiments, creating a thin uniform film of analyte on the underside of the tapered waveguides. Glass microcapillaries are a simple and convenient method for containing an analyte solution, preventing taper contamination and sample evaporation. Still, the most promising setup for the slab tapers is direct fluid insertion into the taper cavity. The collection efficiency of fluorescence here is greatly improved over other methods.

4.5 Works Cited

- [1] M. L. Chabinyk, D. T. Chiu, J. C. McDonald, A. D. Stroock, J. F. Christian, A. M. Karger, and G. M. Whitesides, "An Integrated Fluorescence Detection System in Poly(dimethylsiloxane) for Microfluidic Applications," *Anal. Chem.*, vol. 73, no. 18, pp. 4491–4498, 2001.
- [2] A. Chandrasekaran and M. Packirisamy, "Integrated microfluidic biophotonic chip for laser induced fluorescence detection," *Biomed. Microdevices*, Jun. 2010.
- [3] M.-W. Moon, S. Chung, K.-R. Lee, K. H. Oh, H. A. Stone, and J. W. Hutchinson, "Directed assembly of fluidic networks by buckle delamination

of films on patterned substrates," *Int. J. Mater. Res.*, vol. 98, no. 12, pp. 1203–1208, Dec. 2007.

- [4] D. Yin, E. J. Lunt, a Barman, a R. Hawkins, and H. Schmidt, "Microphotonic control of single molecule fluorescence correlation spectroscopy using planar optofluidics.," *Opt. Express*, vol. 15, no. 12, pp. 7290–5, Jun. 2007.
- [5] C. Monat, P. Domachuk, and B. J. Eggleton, "Integrated optofluidics: A new river of light," *Nat. Photonics*, vol. 1, no. 2, pp. 106–114, Feb. 2007.
- [6] D. J. Thurmer, C. Deneke, Y. Mei, and O. G. Schmidt, "Process integration of microtubes for fluidic applications," *Appl. Phys. Lett.*, vol. 89, no. 22, p. 223507, 2006.
- [7] N. Ponnampalam and R. G. DeCorby, "Out-of-plane coupling at mode cutoff in tapered hollow waveguides with omnidirectional reflector claddings.," *Opt. Express*, vol. 16, no. 5, pp. 2894–908, Mar. 2008.
- [8] B. A. Drobot, A. D. Melnyk, T. W. Allen, and R. G. DeCorby, "Tapered air-core Bragg waveguide spectrometers for lab-on-a-chip applications," *Proc. SPIE*, vol. 8726, p. 87260V–87260V–7, May 2013.

5 Visible band taper spectrometer¹

5.1 Introduction

Lab-on-a-chip (LOC) devices have attracted much interest, with a multitude of potential applications such as point-of-care diagnostics, environmental monitoring, and industrial process control. Optical detection methods are particularly useful as they are highly sensitive, are typically non-destructive, and can produce nearly real-time results. However, LOC and optofluidic micro-systems often rely on bulky off-chip optical components such as lenses and spectrometers for detection. There is therefore a growing demand for compact microspectrometers that can be integrated on-chip, to increase portability and potentially reduce the cost and complexity of these systems. Portability is especially important in applications such as point-of-care diagnostics and field-deployable threat detectors. On-chip spectrometers are also advantageous because they are aligned on-chip, eliminating the need to align the optical components before each measurement.

Fabry-Perot filters are a compelling choice for LOC applications, with nanometer resolution achievable over a wide operating range [1]. The choice of a linear variable filter (LVF) coupled with simple optics allows for the direct imaging of spatially dispersed wavelengths onto a CCD array [2]. One drawback of such a system is the angular dependence of the filtered wavelengths of light [3],

¹Portions of this chapter were published as a paper in *Optics Express*, vol. 20, pp. 23906-23911, 2012. Other portions were published in Proc. SPIE 8726, Next-Generation Spectroscopic Technologies VI, 87260V, 2013.

necessitating the use of a low-NA optic. Furthermore, higher resolution is correlated with lower throughput of light reaching the detector [4]. Perhaps most limiting, a traditional LVF spectrometer requires illumination by a broad-area and uniform source, although alternative strategies for moving point sources have also been described [4].

We have previously reported chip-scale micro-spectrometers based on tapered air-core Bragg waveguides with omnidirectional Bragg claddings [5]. Position-dependent cutoff results in spatial dispersion of a polychromatic signal. By tailoring the Bragg cladding materials, we have fabricated prototype devices operating in the visible range, exhibiting operational bandwidths of ~ 70 nm and resolution on the order of 1 nm. These microspectrometers may be viewed as side-coupled LVF filters [5]. This input coupling strategy addresses some of the issues already mentioned, in addition to providing unique functionality. Here, we describe the characteristics of these air-core waveguide spectrometers, with regard to application in a sensing system based on spectrally-resolved fluorescence detection.

5.2 Device concept and design

A schematic illustration of an air-core, slab Bragg waveguide taper is shown in Fig. 5.1(a), including a ray-optics depiction of light guidance for wavelengths within the omnidirectional band of the cladding mirrors. As a guided mode propagates towards the narrow end of the taper, it is adiabatically transformed into a vertical

cavity resonant mode at cutoff [6], [7]. For integer mode ordering ($m = 1, 2, 3, \dots$) and neglecting field penetration into the dielectric mirrors, cutoff occurs at core thickness $d_{cm} = m\lambda/2$, where λ is the free-space wavelength. Thus, polychromatic light is dispersed by the taper, and its spectrum can be extracted from the spatial distribution of the light radiated at cutoff. As discussed in detail elsewhere [5], the guided mode is subject to back-reflection, so that a standing wave radiation pattern is observed on the input side of the cutoff point. However, a high-resolution spectrometer can be implemented by placing a low-NA optic in front of the detector, in order to preferentially detect the near-vertically radiated light associated with the cutoff point.

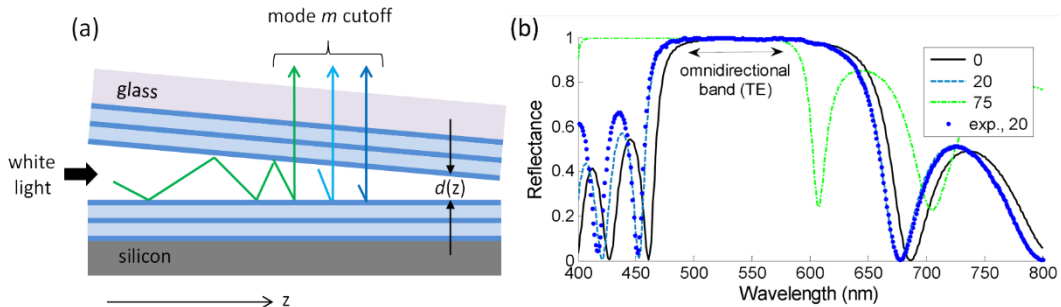


Figure 5.1 – (a) Schematic illustration of ray guidance in a slowly tapered air-core Bragg waveguide. Light within the omnidirectional band of the mirrors is adiabatically transformed from a guided mode to a vertical Fabry-Perot mode at cutoff. (b) Predicted reflectance of evaporated $\text{TiO}_2/\text{SiO}_2$ mirrors (silicon substrate), for TE polarized light at incidence angles of 0, 20, and 75 degrees. Layer thicknesses were assumed to be 61 nm and 90 nm for TiO_2 and SiO_2 , respectively. The symbols are experimental data at 20 degrees.

Owing to the limited index contrast available from transparent materials in the visible range, it is a practical challenge to fabricate Bragg mirrors possessing a truly omnidirectional reflection band [8]. As discussed in Chapter 2, however, an omnidirectional band for TE-polarized light is more easily realized. Initially, we

employed 6.5-period $\text{TiO}_2/\text{SiO}_2$ Bragg mirrors (starting and ending with TiO_2) deposited by electron beam evaporation onto glass and silicon substrates. Subsequently, we used 5.5-period $\text{TiO}_2/\text{SiO}_2$ Bragg mirrors deposited by sputtering onto quartz substrates. Details on the deposition of these mirrors can be found in Chapter 3. For modeling purposes we used standard dispersion models for SiO_2 and the dispersion relation from Kim [9] for TiO_2 . Optical constants extracted from variable angle spectroscopic ellipsometry (VASE) measurements confirmed the validity of these models. For the evaporated films, the refractive index at 550 nm wavelength was estimated to be ~ 1.46 and ~ 2.35 for SiO_2 and TiO_2 , respectively. Similarly, the sputtered films were estimated to have refractive indices of ~ 1.50 and ~ 2.42 for SiO_2 and TiO_2 , respectively. The target layer thicknesses were accordingly chosen to produce a normal-incidence stop-band centered at this same wavelength.

As shown in Fig. 5.1(b), these mirrors provide an omnidirectional reflection band for TE polarized light, spanning the wavelength range from ~ 490 nm to ~ 570 nm (using a $>98\%$ -reflectance criterion). Thus, visible wavelengths in the cyan, green, and yellow ranges are expected (for TE-polarized modes) to be subject to the vertical out-coupling mechanism described above. Bluer (i.e. shorter wavelength) light is well-guided at the wide end of the tapers, where guided rays are far from cutoff and have high incidence angles on the cladding mirrors. Since the mirrors are not highly reflective for normal-incidence in this range, blue light will leak out more gradually and radiate less vertically as cutoff positions are

approached. On the other hand, longer wavelengths outside the omnidirectional band (e.g. in the orange and red range here) are not expected to be well-guided, nor significantly present in the mode cutoff radiation of interest. Figure 5.2 shows a schematic to illustrate this concept.

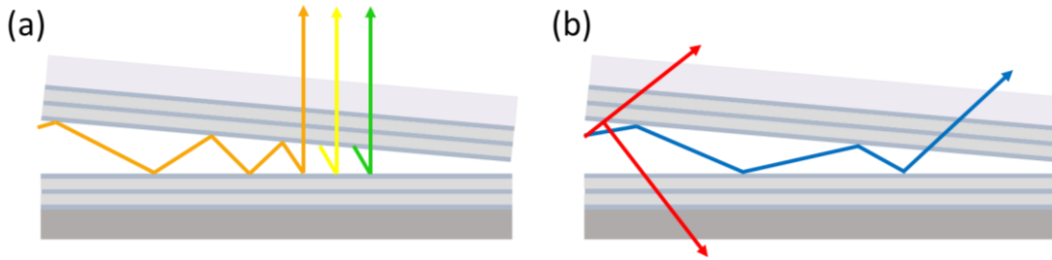


Figure 5.2 – Schematic illustration of how different wavelengths of light tend to behave in a tapered Bragg waveguide. (a) Light inside the omnidirectional reflection band of the mirrors radiates in a near-vertical direction at cutoff. (b) Bluer light is well-guided at the wide end of the taper (far from cutoff) but, due to poor normal-incidence reflectance in this range, leaks more as cutoff is approached. Longer wavelengths outside the omnidirectional band (orange and red light here) are not well-guided by the taper, leaking significantly so that very little light actually reaches cutoff.

If the standing-wave radiation pattern is mitigated as described above, then the wavelength resolution of the taper spectrometer can be approximated as [5]:

$$d\lambda \approx \frac{z_p}{D_T} + \frac{\lambda}{m\pi(\sqrt{R}/(1-R))} \quad , \quad (5.1)$$

where m is the vertical mode order ($m=1,2,3 \dots$), z_p is the effective detector array pixel size (accounting for magnification), R is the normal-incidence reflectance of the cladding mirrors, and the spatial dispersion imparted by the taper is given by:

$$D_T = \frac{\Delta z}{\Delta \lambda} = \frac{\Delta z}{\Delta d} \frac{\Delta d}{\Delta \lambda} \approx \left(\frac{1}{S_T} \right) \left(K + \frac{m}{2} \right) \quad , \quad (5.2)$$

where S_7 is the absolute value of the taper slope, and K is a phase-shift coefficient [10] accounting for field penetration into the cladding mirrors at normal incidence. Here, we are implicitly assuming that the reflectance and phase shift are approximately equal for the upper and lower mirrors. Typically, K is slightly less than 1, and for our mirrors $K \sim 0.9$ [10]. Finally, the free spectral range (FSR) in terms of wavelength can be expressed $\delta\lambda_{FSR} \sim \lambda/(m+1)$. Thus, completely analogous to the well-known properties of a diffraction grating, higher-order modes provide higher spatial dispersion and resolution, but at the expense of reduced FSR. In any case, the omnidirectional bandwidth of the cladding mirrors ultimately limits the operating range. Thus, it is sufficient that the FSR exceeds the omnidirectional bandwidth. For these tapers and assuming TE-polarized modes, the omnidirectional bandwidth is ~ 80 nm centered near 530 nm; the lowest 5 mode orders are expected to have FSR that exceeds this bandwidth.

5.3 Taper Dispersion and Wavelength Resolution

Various laser sources and a broadband super-continuum source (Koheras SuperK Red) were used to test the devices. Light was coupled into the wide end of the tapers, either as a collimated free-space beam or via an optical fiber. Light radiated from the top surface (i.e. through the glass substrate) was collected by an objective lens (5x, with NA = 0.12) and delivered to a silicon camera (Thorlabs model DCC1645C-HQ). As mentioned, use of a low-NA objective lens suppresses the standing-wave radiation leading up to the cutoff point, thereby improving resolution.

To illustrate the spatial dispersion provided by the taper, Fig. 5.3 shows camera images captured with white light coupled into the taper. As evident from Fig. 5.3(a), and in agreement with the discussion above, ~ 20 ‘rainbow’ bands of radiation are observed. The position of particular mode orders was established using the green lasers described below. Near the left (i.e. wide end), the bands overlap due to the smaller FSR of the higher mode orders. Nearer the right (i.e. small end) of the taper, the bands become clearly resolved, as shown for example in Fig. 5.3(b). Bands associated with the lowest ~ 5 mode orders are free of overlap from adjacent orders, and contain yellow (somewhat), green (especially), and cyan-blue light. These facts are entirely consistent with the theoretical description in Section 5.2. Note that the bright spots of scattered light in Fig. 5.3 are primarily due to inclusions in the glass slide used as the transparent substrate for this sample.

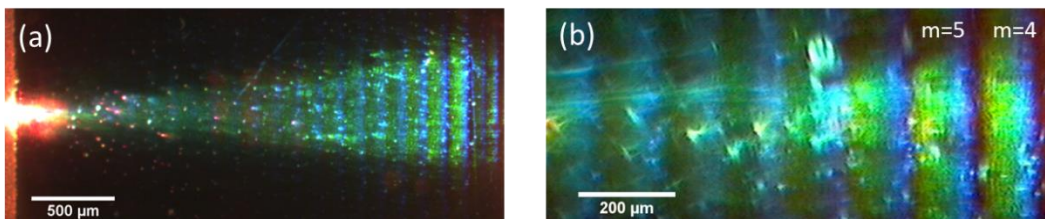


Figure 5.3 – (a) Microscope photograph showing a taper in its entirety, with white light coupled into the wide end of the taper, at the left side of the image. Approximately 20 partly overlapping rainbow bands are visible, each one associated with cutoff of a particular mode order (see text). The two lowest mode orders at the right appear dimmer because they are partly obscured by epoxy. (b) A higher magnification image of some ‘rainbows’ is shown. For sufficiently low mode orders on the right, the FSR is large enough such that the full range of colors (yellow, green, cyan-blue) within the cladding omnidirectional band is well resolved.

To assess the resolution of these tapers (which were assembled from mirrors evaporated on glass and Si), we employed a pair of green lasers with peak wavelengths of ~ 532 and ~ 543 nm, respectively. These lasers were simultaneously launched using a free-space coupling method, with a slight angle between the beams. Figure 5.4(a) shows the cutoff radiation associated with ~ 20 mode orders along the entire taper length. From Eq. (5.2), the spacing between the cutoff positions for the two lasers is expected to scale with the mode order. This was experimentally verified and is illustrated in the plot of Fig. 5.4(b). Fixing $\Delta\lambda = 11$ nm, this plot provides an estimate of the average taper slope, $S_T \sim 1.1$ $\mu\text{m}/\text{mm}$, in good agreement with the value predicted from the taper dimensions.

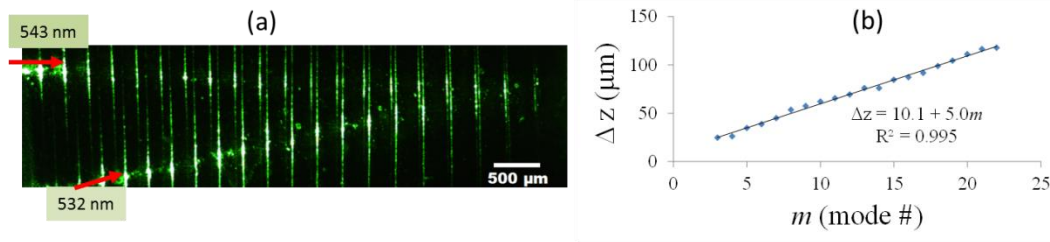


Figure 5.4 – (a) Camera image of the light radiated from the taper with simultaneous input (at the left) of 532 nm and 543 nm wavelength laser light. Each pair of lines corresponds to the cutoff position of a particular mode order; mode order decreases towards the right. (b) Plot of the spacing (Δz) between cutoff positions of the two lasers, versus the mode order.

Figure 5.5 shows representative plots of pixel intensity versus distance, extracted from images similar to that shown in Fig. 5.4(a). Column-wise averaging of pixels was used to reduce noise. The camera images were scaled using photolithographic features of known dimension, enabling a mapping between pixel number and spatial coordinate z . The experimental resolution can be

approximated from the FWHM of the individual laser lines (see the labels in the plot of Fig. 5.5(a)), as $d\lambda_E \sim dz / (\Delta z / \Delta\lambda)$, where $\Delta\lambda = 11$ nm is the known wavelength difference of the two lasers. For the plots in Fig. 5.5, we estimate an experimental wavelength resolution $d\lambda_E \sim 2.1$ nm and ~ 2.3 nm for modes 6 and 7, respectively. Similar resolution (typically within ± 0.5 nm) was estimated for most of the mode orders. Note that a complete spectrum spanning the entire omnidirectional band is available from the cutoff radiation for a single low-order mode. Consistent with Eq. (5.2), the results show that spectral content can be extracted, with ~ 2 nm resolution over ~ 80 nm operating bandwidth, by imaging a section of the waveguide only ~ 100 μm in length (e.g. For cutoff of the $m = 6$ mode).

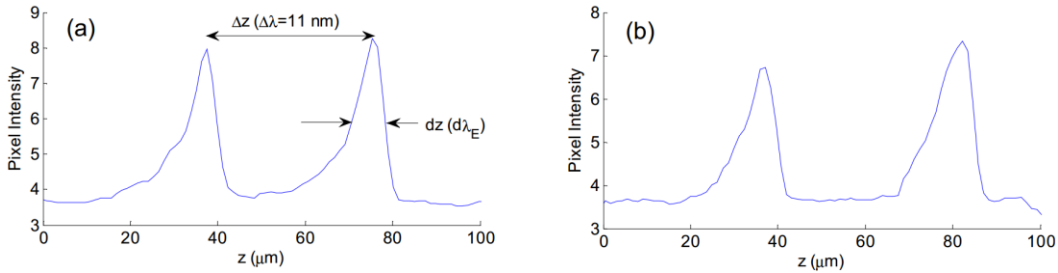


Figure 5.5 – (a) Column-wise averaged pixel intensity versus z , for the $m = 6$ cutoff lines of the simultaneously launched 543 nm and 532 nm lasers (b) As in part (a), but for the $m = 7$ lines.

For the evaporated mirrors used here (see Fig. 5.1), the predicted normal-incidence reflectance is $R \sim 0.992$ and ~ 0.996 for the Si and glass substrates, respectively. The effective pixel size for our detection system is $z_p \sim 1.2$ μm (the actual pixel size is 3.6 μm , and the collection optics have net magnification $\sim 3\times$). Using an average $R \sim 0.994$ and $S_T \sim 1$ $\mu\text{m}/\text{nm}$, Eq. (5.1) predicts $d\lambda \sim 2$ nm for $m = 1$

(in good agreement with the experimental values), but also predicts that resolution increases with mode order. For example, $d\lambda < 1$ nm is predicted for $m = 6$.

Several factors likely contribute to these discrepancies between theory and experiment. First, it should be noted that Eq. (5.2) is an approximate model only, and does not account for standing-wave effects that effectively broaden the radiation region near cutoff [5]. This is reflected by the asymmetry in the line-shapes from Fig. 5.5. Second, it is probable that the mirrors have lower-than-expected reflectance, due to absorption and scattering. Third, camera non-idealities such as pixel cross-talk might also play a role in reducing the experimental resolution. Finally, the relative insensitivity of the experimental resolution with respect to mode order suggests that the collection optics play a limiting role. Notably, the relatively thick glass substrates introduce scattering and distortion, making it difficult to focus reliably on light radiating from the air core of the waveguides. We expect the results could be improved by the use of higher quality quartz substrates, or by implementation of channel tapers using buckling self-assembly [5].

Using the method described above, we also assessed the resolution of the tapers made from films sputtered on quartz substrates. Figure 5.6(a) shows the cutoff radiation associated with the first ~ 8 mode orders along a taper ~ 5 mm in length. Pixel intensity information was extracted from images such as shown in Fig. 5.6(a), and this data was used to estimate the experimental resolution. From

Eq. (5.1), the resolution is expected to increase with mode order. For the quartz tapers case, this trend was experimentally verified and is illustrated in the plot of Fig. 5.6(b).

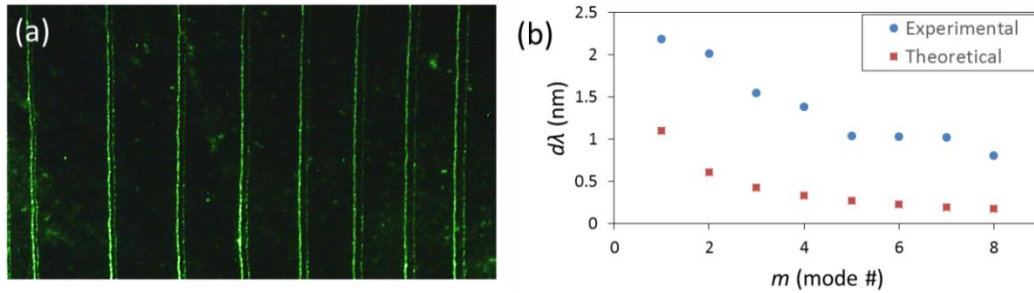


Figure 5.6 – (a) Camera image of the light radiated from the taper, with waveguide-coupled input of 532 nm and 543 nm wavelength laser light from the left. Each pair of lines corresponds to the cutoff position of a particular mode order; mode order increases towards the right. (b) Plot of the resolution ($d\lambda$) versus mode order, determined by the FWHM and spacing of the laser lines for a particular mode order. Experimental resolution is lower than theoretical predictions, in part due to the use of a simple vertical Fabry-Perot cavity model in the derivation of Eq. (5.1).

Although the general trend of the experimental results agrees well with the theoretical resolutions, the measured resolution is on average ~ 1 nm lower than that of theory. For example, Eq. (5.1) predicts $d\lambda \sim 1.1$ nm and ~ 0.2 nm for modes 1 and 8, respectively. In contrast, the experimental resolutions for modes 1 and 8 were found to be ~ 2.2 nm and ~ 0.8 nm, respectively. This discrepancy may be attributed to a combination of factors, most important of which is uncertainty in the mirror reflectance. The theoretical data points in Fig. 5.6(b) assume a best-case reflectance of 0.995, in turn estimated from the material indices and neglecting residual absorption and scattering loss. As is well-known, experimental verification of near-unity reflectance is challenging. We hope to explore this in greater detail in future work.

As with the evaporated mirror tapers, standing-wave effects, pixel noise and pixel cross-talk are also possible contributing factors to the discrepancy between the theoretically predicted and measured wavelength resolution.

Due to the highly multimodal nature of the tapers, we did not attempt to experimentally assess the light throughput efficiency. However, based on our previously reported analyses [5], we anticipate throughput as high as ~ 0.05 is possible with optimal input coupling.

5.4 Taper operating range

To assess the operating range of the tapers, light radiated from the top of a taper was compared to the spectrum collected using a commercial spectrometer (USB4000, Ocean Optics). This commercial spectrometer requires calibration to normalize the spectral response of its CCD array and the spectral efficiency of its diffraction grating and associated optics. As per the instructions provided by the manufacturer [11], this was accomplished by approximating the output of a tungsten halogen light source (HL-2000, Ocean Optics) as a blackbody source with a colour temperature of 2960 K.

Figure 5.7(a) shows the raw spectrum and the corrected spectrum for the halogen light source. Taking the ratio of the corrected spectrum to the raw spectrum gives an approximate correction factor for the spectrometer:

$$C_S(\lambda) = S_C(\lambda)/S_R(\lambda) \quad (5.3)$$

where S_R is the raw (uncorrected) spectral response, S_C is the corrected spectral response, and C_S is the correction factor to be applied to raw spectrometer data as shown in Fig. 5.7(b). This correction is necessary because the grating and detector array inside the commercial spectrometer have peak efficiency near 550 nm wavelength, while the efficiency falls off away from that wavelength. As shown below, the tapered waveguide spectrometer exhibits an analogous spectrally-dependent ‘instrument response’ function.

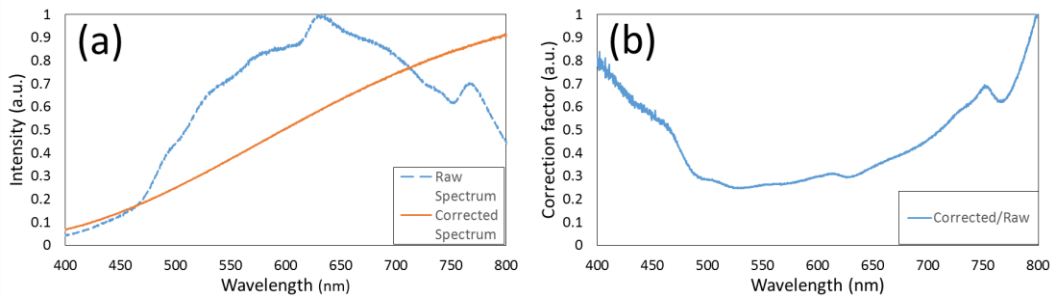


Figure 5.7 – A tungsten halogen light source (HL-2000, Ocean Optics) was approximated as a blackbody source (color temperature $T = 2960$ K) to calibrate the spectral response of the spectrometer (USB4000, Ocean Optics). (a) The raw and corrected spectrum of the tungsten halogen source. (b) Approximate correction factor (normalized to a peak value of 1) for the spectral response of the spectrometer in the 400-800 nm wavelength range.

Now, consider the extraction of spectral response from the images of light radiated at cutoff from the tapered waveguides. As with the commercial spectrometer, a correction factor is needed to account for the spectrally dependent quantum efficiency (QE) of the CCD array in the camera and also to account for the spectral efficiency of the dispersive element (which in this case is the tapered waveguide, instead of the diffraction grating). First, consider the response of the primary camera (Coolsnap ES, Photometrics) employed in the

measurements that follow below. The spectral dependence of the camera is almost entirely attributable to the wavelength-dependent QE of the detector elements, so that we can define a camera correction factor as follows:

$$C_{CCD} = 1/QE \quad (5.4)$$

Figure 5.8 shows the QE of the CCD when the camera is operating in ‘normal’ mode [12]. Since the QE is relatively flat over the wavelength range of interest for the tapers discussed below (i.e. ~490-560 nm), the camera correction factor has only a minor impact on the shape of the spectra extracted from camera images. Note that the quantum efficiency of the detectors is taken into account by the calibration and correction procedure described for the taper spectrometer below, as part of the overall ‘instrument response’.

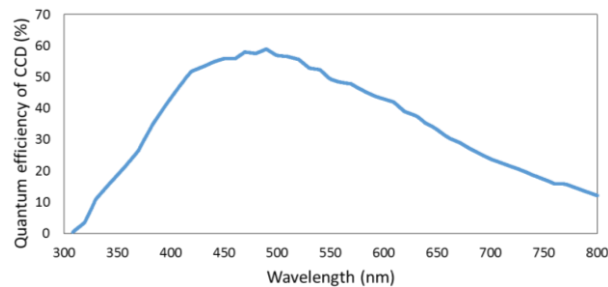


Figure 5.8 – Quantum efficiency (QE) of the CCD in the camera (Coolsnap ES, Photometrics) when operating in ‘normal’ mode. The QE data was taken from the camera manual [12].

The commercial spectrometer was used to measure the spectrum of a super continuum white light source (SuperK Red, Koheras), and the result is shown in Fig. 5.9(a). The spectrum shown was corrected using the instrument response function discussed above (see Fig. 5.7(b)). Using a 20X objective lens, the same

white light source was then coupled into the wide end of a taper. The taper (sample H4.2) had a starting core height of $\sim 5.9 \mu\text{m}$ and a taper slope of $\sim 1.5 \mu\text{m}/\text{mm}$. A sputtered mirror on a $\sim 4.7 \text{ mm}$ long quartz substrate and an evaporated mirror on a $\sim 4 \text{ mm}$ long Si substrate were used to fabricate the taper. In this case, an optical fiber (core diameter of 1 mm , $\text{NA} = 0.22$) was aligned directly above the taper to collect light radiating from mode orders $m = 2$ to $m = 5$. Figure 5.9(b) shows the resulting spectrum measured by the commercial spectrometer. The spectral content of the radiated light lies primarily in the $\sim 490 \text{ nm}$ to $\sim 560 \text{ nm}$ range, in agreement with expectations based on the TE-polarized omnidirectional band of the mirrors employed (see Section 5.2).

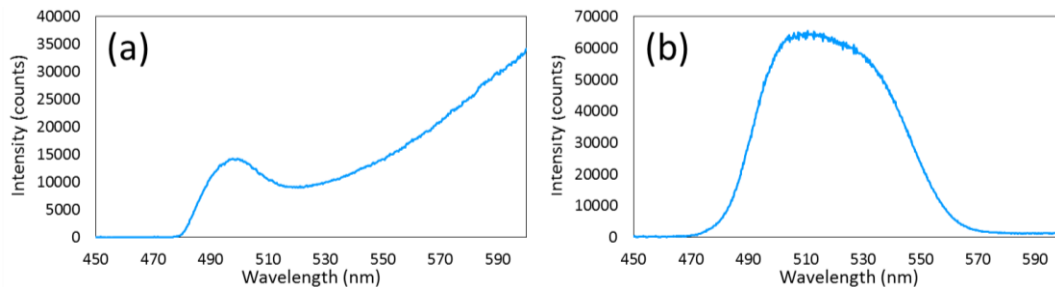


Figure 5.9 – (a) Super continuum white light source (SuperK Red, Koheras) spectrum obtained using a commercial spectrometer. (b) Spectrum of white light radiating from top of taper, contributed by mode orders $m = 2$ to $m = 5$. The light was collected using an optical fiber (core diameter of 1 mm and $\text{NA} = 0.22$) and delivered to the same commercial spectrometer.

Next, a zoom lens (Edmund optics, $0.7\times - 4.5\times$ with $\text{NA} < 0.09$) was used to collect the light radiated from the top surface of the taper and deliver it to the CoolSNAP camera. As discussed earlier, the low-NA zoom lens helps to suppress standing-wave radiation from waveguide modes approaching cutoff. A camera image of radiated light belonging to mode orders $m = 2$ to $m = 5$ is shown in Figure

5.10(a). From the discussion in Section 5.2, the taper provides a spectral to spatial mapping of light within the omnidirectional band of the cladding mirrors. Thus, the spectral content of the light radiated at cutoff (within this omnidirectional band) can be extracted from the spatial intensity profile of light (associated with a particular mode order) captured by the camera. The column-wise averaged pixel intensity of this image was used to extract the spectra for mode orders $m = 2$ and $m = 3$, shown in Fig. 5.10(b) and Fig. 5.10(c), respectively.

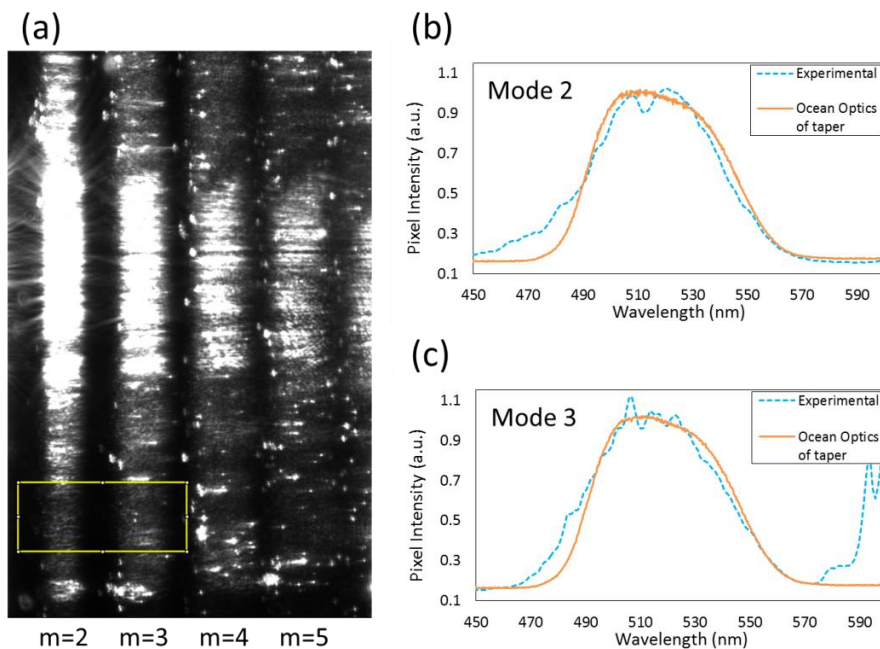


Figure 5.10 – Super continuum white light source coupled into wide end of taper using 20X objective lens. (a) Camera image of light radiating through top of taper. Mode orders $m = 2$ to $m = 5$ are shown, from left to right. (b)-(c) Extracted spectra of white light source for mode orders $m = 2$ and $m = 3$, respectively. These spectra compare well to the spectrum collected by the optical fiber, delivered to the commercial spectrometer.

The extracted spectra for mode orders 2 and 3 shown are both in good agreement with the spectrum collected by the optical fiber and measured by the commercial spectrometer. The bright spots seen in the camera image are due to

defects in the quartz substrate being lit up by stray light from the super continuum source. This leads to signal noise in the extracted spectra, evident in the roughness of the curves. Note that pixel intensity data was mapped to wavelength by using the cutoff lines of the 543 nm and 594 nm laser sources for scaling.

It is important to note that the plots shown in Fig. 5.9 and 5.10 correspond to the spectrum of the light radiated in the (nearly) surface-normal direction from the taper, and not to the spectrum of the input white light source. These results clearly illustrate that, as a spectrometer, the taper has both a fixed operational range (limited by the omnidirectional band of the mirrors) and an ‘instrument response’ (caused by the spectral dependence of the efficiency of vertical radiation at cutoff). To use the taper as a spectrometer, input signals should be restricted to this operational range, and a calibration procedure is necessary to account for the spectral dependence of the taper within this range.

To assess the operating range and spectral ‘instrument response’ of the taper, the spectrum obtained from the taper (i.e. from direct mapping of pixel intensity to wavelength) was compared to a reference spectrum obtained using the commercial spectrometer (and corrected as described above). Analogous to the correction procedure for the commercial spectrometer, we define an ‘instrument response’ correction factor for the taper as follows:

$$C_T(\lambda) = S_C(\lambda) / S_T(\lambda) \quad (5.5)$$

where S_T is the raw spectrum obtained from a plot of the pixel intensity and S_C is the reference spectrum (known, or obtained using the commercial spectrometer). Note that C_T implicitly takes into account both the spectrally dependent quantum efficiency of the camera and the spectrally dependent radiation from the taper. Figure 5.11 shows a plot of the correction factor extracted for a particular taper, using light from a super continuum light source (see Fig. 5.9). From this plot, the taper appears to have an operational bandwidth of ~ 70 nm, centered at ~ 520 nm. The source does not have significant power below ~ 490 nm, however, which makes it difficult to assess the instrument response in that range.

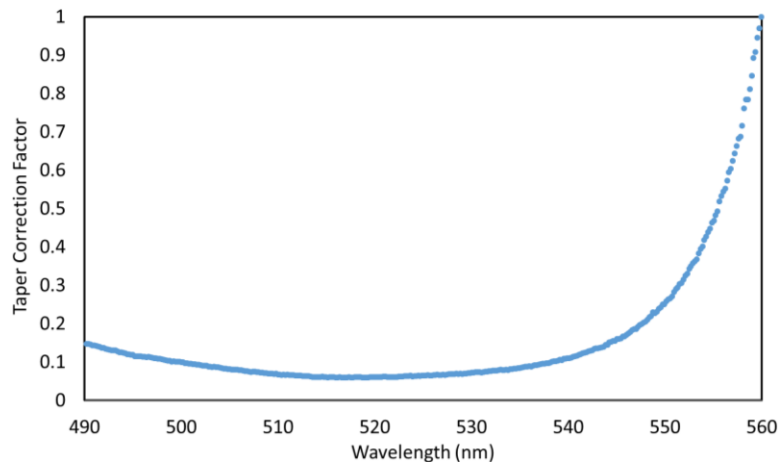


Figure 5.11 – Plot of the correction factor extracted for a particular taper, using light from a super continuum light source. Operating range is centered at ~ 520 nm, with a bandwidth of ~ 70 nm. Data is unreliable below 490 nm due to low signal.

To better determine the operating range of the tapers, a white light source covering the entire operational range of the tapers is required. Using the same taper (sample H4.2) and camera setup as above, a white LED (model # C503B-WAN-CBaDa231, Digikey) was coupled into the wide end of the taper. Data was

extracted from a camera image of the light radiated from the taper, using the same procedure as above (see Fig. 5.10). Figure 5.12 shows the extracted ‘instrument response’ correction function for mode orders $m = 2$ and $m = 3$ of the taper. The operational bandwidth is ~ 70 nm, with peak sensitivity at ~ 520 nm. Since the white LED emission covers the entire operating range of the taper, the correction factor appears to be reasonable for all wavelengths of interest.

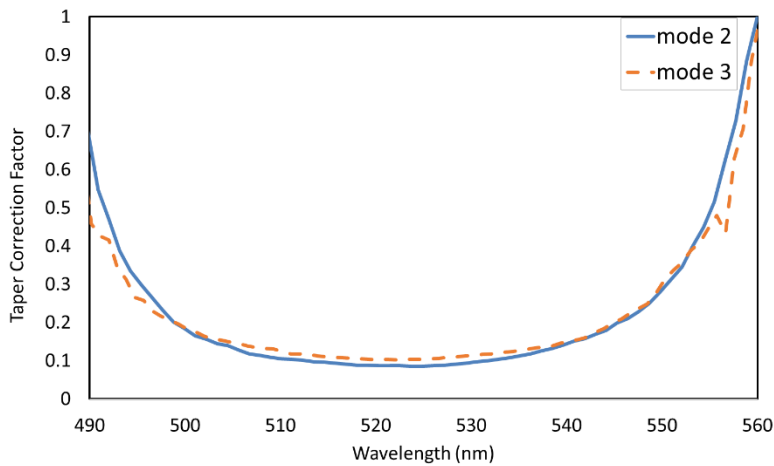


Figure 5.12 – A white LED (model # C503B-WAN-CBaDa231, Digikey) was used to estimate the correction function $C_T(\lambda)$ for mode orders $m = 2$ and $m = 3$ of a taper. Operating range is centered at ~ 520 nm, with a bandwidth of ~ 70 nm. Unlike the case with the super continuum light source, the ratio is reasonable for all wavelengths of interest.

To help validate the experimental results for the operating range of the tapers, the radiated power versus position of the taper was modeled. The optical properties of the evaporated mirrors on silicon and sputtered mirrors on quartz were used (see Chapter 3). For a taper slope of $1.5 \mu\text{m}/\text{mm}$ and for TE-polarized light of mode order $m = 2$, the radiated power versus position along the taper is shown in Fig. 5.13. For wavelengths between ~ 490 nm and ~ 570 nm, light reaches

cutoff and is radiated vertically from the taper. Radiation at cutoff is strongest for light with a wavelength of ~ 520 nm.

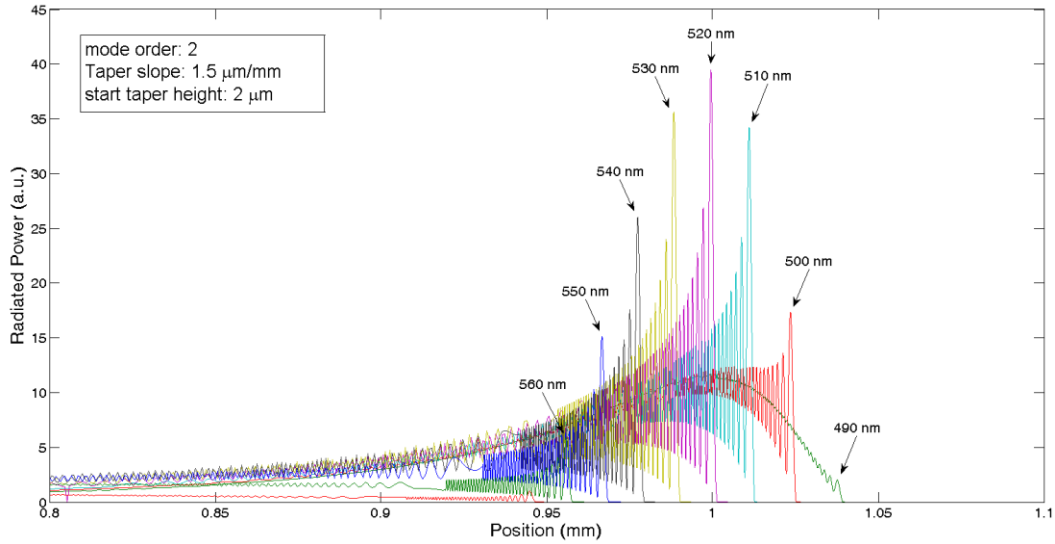


Figure 5.13 – Simulation of radiated power of guided modes versus position, for a taper with a slope of $1.5 \mu\text{m}/\text{mm}$ and TE-polarized light of mode order $m = 2$. Light reaches cutoff for wavelengths between ~ 490 nm and ~ 570 nm, with peak sensitivity at ~ 520 nm.

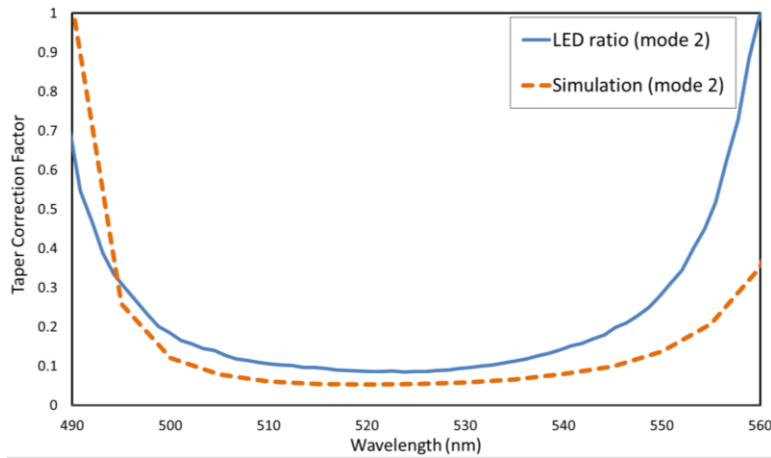


Figure 5.14 – Plot of the correction function $C_T(\lambda)$ for a taper, estimated using the simulated relative power of light radiated at cutoff, for different wavelengths. Also plotted is the correction function obtained using the white LED data. There is good agreement between the experimental and simulated results, confirming the validity of the method for measuring the operating range of the tapers.

By taking the relative power of the radiated light at cutoff for each wavelength, the operating range of the taper may be estimated. Figure 5.14 shows a plot of the correction function $C_T(\lambda)$ for a taper, estimated using the simulated relative power of light radiated at cutoff, for different wavelengths. Also plotted is the correction function obtained using the white LED data, from Fig. 5.12. There is good agreement between the experimental and simulated results, confirming the validity of the method for evaluating the operating range of the tapers and estimating a correction factor to account for the 'instrument response' of the tapers.

5.5 Conclusions

To determine the performance of the slab Bragg waveguide tapers as spectrometers, a variety of experiments were carried out. Lasers of various wavelengths were coupled into the tapers to assess dispersion and resolution. Spacing between cutoff positions was verified to increase with increasing mode order, according to the dispersion relation from Eq. (5.2). For tapers made from evaporated mirrors, most mode orders exhibited resolutions of ~ 2 nm, exhibiting a relative insensitivity regarding mode order. On the other hand, tapers fabricating using mirrors sputtered on quartz had experimental resolutions ranging from ~ 2.2 nm to ~ 0.8 nm, for mode orders $m = 1$ to $m = 8$.

White light radiated from the taper was compared to the spectrum measured using a commercial spectrometer. The ratio of the two spectra gives the

operating range of the taper as well as the correction factor for scaling the spectrum. The operational bandwidth was measured to be ~ 70 nm, with peak sensitivity at ~ 520 nm. A simulation of the radiated power versus position along the taper was in good agreement with the experimental result.

5.6 Works Cited

- [1] M. Gouzman, N. Lifshitz, S. Luryi, O. Semyonov, D. Gavrilov, and V. Kuzminskiy, "Excitation-emission fluorimeter based on linear interference filters.," *Appl. Opt.*, vol. 43, no. 15, pp. 3066–72, May 2004.
- [2] A. Emadi, H. Wu, G. de Graaf, and R. Wolffenbuttel, "Design and implementation of a sub-nm resolution microspectrometer based on a Linear-Variable Optical Filter.," *Opt. Express*, vol. 20, no. 1, pp. 489–507, Jan. 2012.
- [3] M. Dandin, P. Abshire, and E. Smela, "Optical filtering technologies for integrated fluorescence sensors.," *Lab Chip*, vol. 7, no. 8, pp. 955–77, Aug. 2007.
- [4] O. Schmidt, P. Kiesel, and M. Bassler, "Performance of chip-size wavelength detectors.," *Opt. Express*, vol. 15, no. 15, pp. 9701–6, Jul. 2007.
- [5] R. G. DeCorby, N. Ponnampalam, E. Epp, T. Allen, and J. N. McMullin, "Chip-scale spectrometry based on tapered hollow Bragg waveguides.," *Opt. Express*, vol. 17, no. 19, pp. 16632–16645, Sep. 2009.
- [6] M. L. Povinelli, M. Ibanescu, S. G. Johnson, and J. D. Joannopoulos, "Slow-light enhancement of radiation pressure in an omnidirectional-reflector waveguide.," *Appl. Phys. Lett.*, vol. 85, no. 9, p. 1466, 2004.
- [7] N. Ponnampalam and R. G. DeCorby, "Out-of-plane coupling at mode cutoff in tapered hollow waveguides with omnidirectional reflector claddings.," *Opt. Express*, vol. 16, no. 5, pp. 2894–908, Mar. 2008.
- [8] M. Deopura, C. Ullal, B. Temelkuran, and Y. Fink, "Dielectric omnidirectional visible reflector.," *Opt. Lett.*, vol. 26, no. 15, pp. 1197–1199, 2001.

- [9] S. Y. Kim, "Simultaneous determination of refractive index, extinction coefficient, and void distribution of titanium dioxide thin film by optical methods," *Appl. Opt.*, vol. 35, no. 34, pp. 6703–7, Dec. 1996.
- [10] S. Weidong, L. Xiangdong, H. Biqin, Z. Yong, L. Xu, and G. Peifu, "Analysis on the tunable optical properties of MOEMS filter based on Fabry–Perot Cavity," *Opt. Commun.*, vol. 239, no. 1–3, pp. 153–160, Sep. 2004.
- [11] "SpectraSuite Spectrometer Operating Software: Installation and Operation Manual." [Online]. Available: <http://www.oceanoptics.com/technical/SpectraSuite.pdf>.
- [12] Photometrics, "Photometrics Support: CoolSNAP ES." [Online]. Available: <http://www.photometrics.com/support/pdfs/manuals/CoolSNAPcfESManual.pdf>.

6 Fluorescence Experiments¹

6.1 Introduction

This chapter focuses on the implementation of a prototype sensing system based on spectrally-resolved fluorescence detection. Efforts towards integrating air-core waveguide spectrometers with microfluidics are described. Whereas Chapter 5 assessed the capabilities of the tapers as visible-band spectrometers, this chapter explores some of the practical challenges involved in setting up a fluorescence LOC device. The tapers were used in a conventional linear variable filter (LVF) configuration, as well as in a side-coupled LVF configuration. Fluorescent microspheres (FluoSpheres, Invitrogen) were chosen as test particles because they typically suffer minimal photobleaching [1] and are available in various diameters.

6.2 LVF fluorescence experiments

Figure 6.1 shows a schematic illustration of an air-core, slab Bragg waveguide taper in a conventional LVF configuration. The fluorescent microspheres may be held in a glass capillary (Fig. 6.1(a)) or placed in direct contact with the underside of the taper (Fig. 6.1(b)). In this mode of operation, the taper acts as a Fabry-Perot interferometer of varying cavity thickness, sometimes called a Fizeau interferometer [2]. Incoming polychromatic light is spatially filtered, based on the Fabry-Perot modes associated with the cavity thickness at each position. The

¹Portions of this chapter were published in Proc. SPIE 8726, Next-Generation Spectroscopic Technologies VI, 87260V, 2013.

modal condition ($m=1,2,3\dots$) for the cavity, neglecting field penetration into the dielectric mirrors, occurs for cavity thickness $d_{cm}=m\lambda/(2\cos\theta)$, where λ is the free-space wavelength and θ is the angle relative to normal. In order to implement a high-resolution spectrometer, low-NA optics must be used to mitigate the angular dependence of the mode condition. If this condition is satisfied, the spectrum can be mapped directly from the position-dependent, vertical Fabry-Perot resonance.

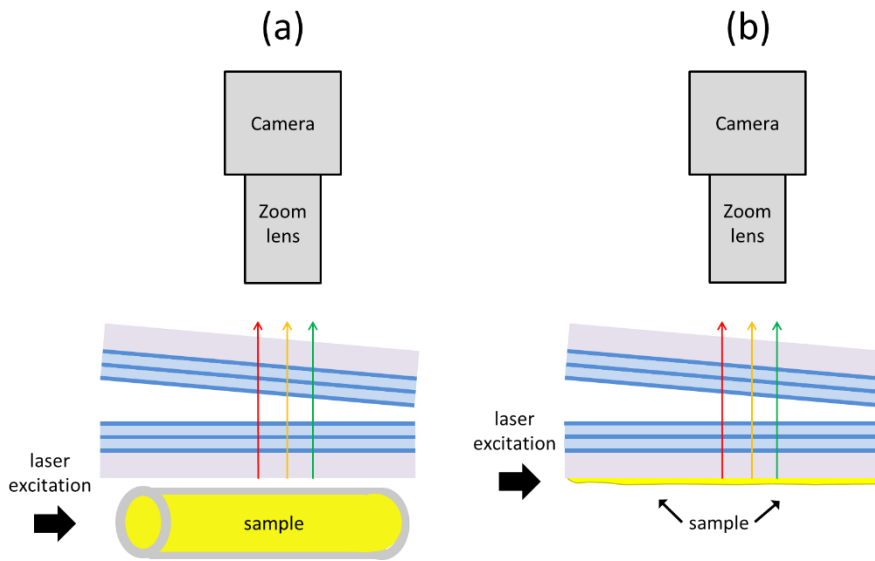


Figure 6.1 – Schematic illustration of a tapered slab Bragg waveguide in a conventional linear variable filter configuration. The taper spatially filters polychromatic light into Fabry-Perot resonant modes. (a) Fluorescent microspheres positioned beneath the taper in a glass capillary. (b) Fluorescent microspheres placed in direct contact with the underside of the taper, forming a thin film between the taper and the PDMS basin.

6.2.1 Fluorescence from a glass capillary

To assess the spectroscopic capabilities of the tapers in a traditional LVF configuration, a capillary filled with a 0.5% solids (8.2×10^{13} particles/mL) solution of ~ 48 nm diameter Orange FluoSpheres (540 nm peak excitation wavelength/560 nm peak emission wavelength) was placed beneath a taper. The taper (sample

6.5) had a starting core height of $\sim 2.1 \mu\text{m}$ and a taper slope of $\sim 0.6 \mu\text{m}/\text{mm}$. Sputtered mirrors on quartz substrates $\sim 5.7 \text{ mm}$ and $\sim 3.7 \text{ mm}$ in length were used to fabricate the taper.

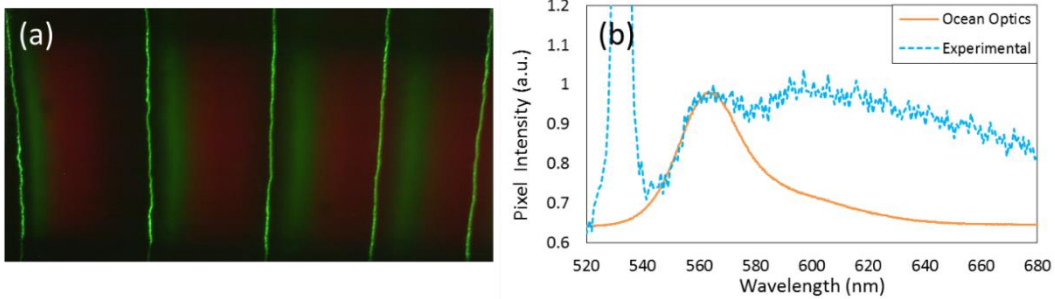


Figure 6.2 – (a) Camera image of spectrally-resolved fluorescence from Orange (540/560) FluoSpheres, for the case of a capillary placed below the taper. Mode orders $m = 1$ to $m = 4$ are shown. The discrete green lines are due to scattered light from the 532 nm excitation laser. (b) The extracted emission spectrum of the Orange FluoSpheres for mode order $m = 1$. Compared to the spectrum collected by a commercial spectrometer (USB4000, Ocean Optics), there is significant discrepancy at longer wavelengths.

The capillary was oriented perpendicular to the axis of the taper, such that it uniformly illuminated multiple modes. A zoom lens (Edmund Optics, 0.7x – 4.5x with $\text{NA} < 0.09$) was used to collect light to the camera (Coolsnap ES, Photometrics). Figure 6.2(a) shows an image of the filtered light, with excitation of the microspheres by a 532 nm laser beam aligned with the capillary. Within each mode order, both the broad emission spectrum of the microspheres and discrete lines associated with scattered light from the excitation laser are visible. Note that an attractive property of LVF filters for fluorescence applications is that the emission spectrum is inherently isolated from the excitation light, reducing the requirement for separate laser line rejection filters. In order to map the pixel positions of the image in Fig. 6.2(a) to specific wavelengths, two or more lasers of

known wavelength (e.g. 532 nm and 543 nm) were coupled simultaneously. Based on such calibration, the extracted emission spectrum of the Orange FluoSpheres is plotted in Fig. 6.2(b).

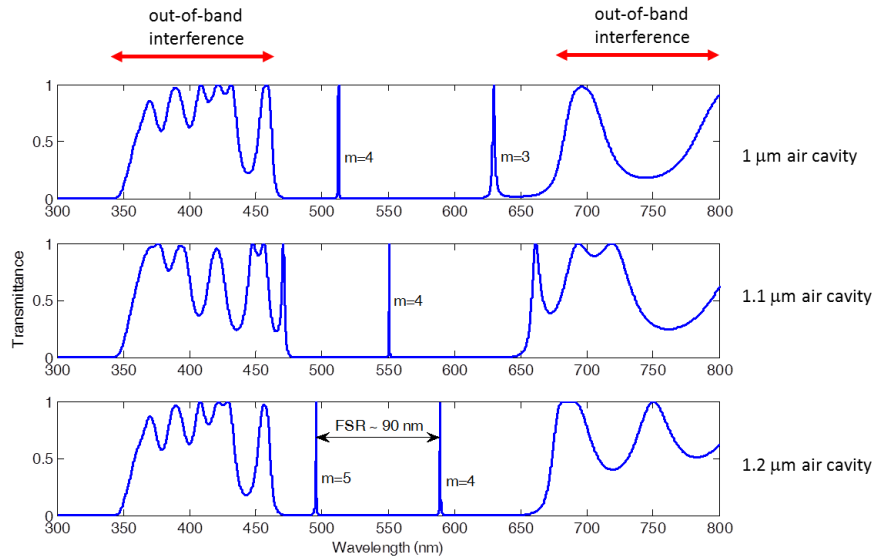


Figure 6.3 – Transfer-matrix simulations of the LVF cavity transmittance. The LVF is relatively transparent outside of the stop-band of the mirrors, and light in that range causes interference at the detector.

While the peak of the emission spectrum is in good agreement with data from a commercial spectrometer (USB4000, Ocean Optics), there is significant discrepancy on the long wavelength side of the spectrum. This can be attributed to the relative transparency of the LVF for wavelengths above ~ 600 nm (i.e. outside the stop-band of the mirrors, see Chapter 3), resulting in weaker filtering of this light. In fact, the transfer-matrix simulations (shown in Fig. 6.3) of the LVF cavity transmittance in this range reveal broad, low Q-factor resonance peaks, with the transmitted wavelengths dependent on position (i.e. on the air-core

height). In simple terms, the LVF is only able to resolve a spectrum within the high-reflectance stop-band of the mirrors.

The relatively low reflectance for wavelengths above ~ 600 nm results in a smearing of the spectrum in that range. To address this limitation, conventional LVF filters either require very complex, high-layer-count mirrors [3] or use separate filters to suppress out-of-band light [2]. A significant advantage of the side-coupled configuration (i.e. waveguide configuration, see Chapter 5) is that it inherently suppresses spectral content outside of the operating range of the taper.

6.3.2 Fluorescence from a thin film of microspheres in solution

In a second experiment, a small volume of a 0.5% solids solution of Orange FluoSpheres was placed in direct contact with a taper. The taper (sample 5.5) had a starting core height of ~ 2.1 μm and a taper slope of ~ 0.5 $\mu\text{m}/\text{mm}$. Sputtered mirrors on quartz substrates ~ 4.7 mm in length were used to fabricate the taper. The FluoSpheres were placed by applying a small volume of solution to the surface of a PDMS holder, and then pressing the taper chip onto this surface. This produced a thin and approximately uniform film of fluorescent microspheres in intimate contact with the LVF. In this geometry, a much smaller volume of microspheres contribute to a particular mode order. Figure 6.4(a) shows an image of the microspheres fluorescing in this configuration, with cutoff positions of a 532 nm laser visible for mode orders $m = 2$ to $m = 6$. The resulting emission spectrum of the microspheres for mode order $m = 4$ is graphed in Fig. 6.4(b).

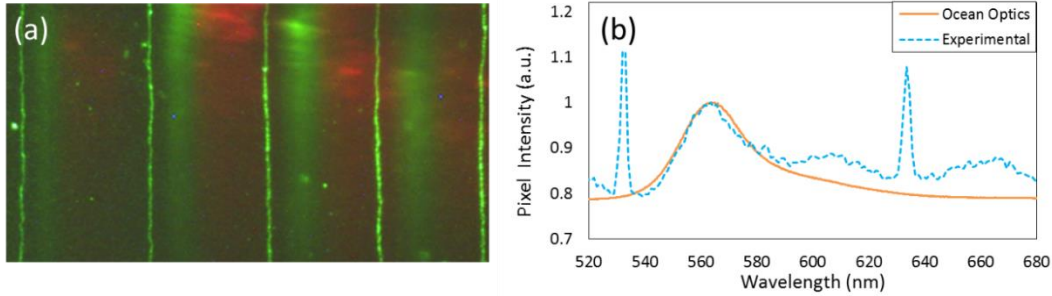


Figure 6.4 – (a) Camera image of fluorescence from a film of Orange (540/560) FluoSpheres placed directly in contact with the underside of the taper. Mode orders $m = 2$ to $m = 5$ are shown. (b) Emission spectrum of Orange FluoSpheres for mode order $m = 4$. Compared to the spectrum collected by a commercial spectrometer, there is significant discrepancy at higher wavelengths.

As above, the peak of the emission spectrum agrees well with the spectrum obtained from a commercial spectrometer. Notably, the spectral deviation at higher wavelengths is much less pronounced here, likely due to the decrease in analyte volume. Even with this improvement in the measured spectrum, the inherent limitations of a LVF configuration are evident.

6.3 Waveguide coupled spectrometer

Fig. 6.5 illustrates the air-core taper operating in a waveguide configuration, where light within the omnidirectional band of the cladding mirrors propagates along the tapered waveguide. The fluorescent microspheres may either be held in a glass capillary aligned near the wide end of the taper (Fig. 6.5(a)) or inserted directly into the taper cavity (Fig. 6.5(b)).

As a guided mode propagates towards the narrow end of the taper, it approaches cutoff, where it is adiabatically transformed into a vertical cavity resonant mode [4]. Neglecting field penetration into the dielectric mirrors, cutoff

for a guided mode occurs at a core thickness $d_{cm} = m\lambda/2$, where m is integer mode ordering ($m=1,2,3\dots$) and λ is the free-space wavelength. Note the intimate relationship between Fabry-Perot modes and guided modes of the waveguide. A guided mode experiences partial back-reflection as it approaches cutoff, creating a standing wave radiation pattern [5]. To realize a high-resolution spectrometer, it is necessary to detect only the near-vertically radiated light. To suppress light radiated into off-normal directions, a low-NA zoom lens ($NA \sim 0.09$) was placed in front of the camera.

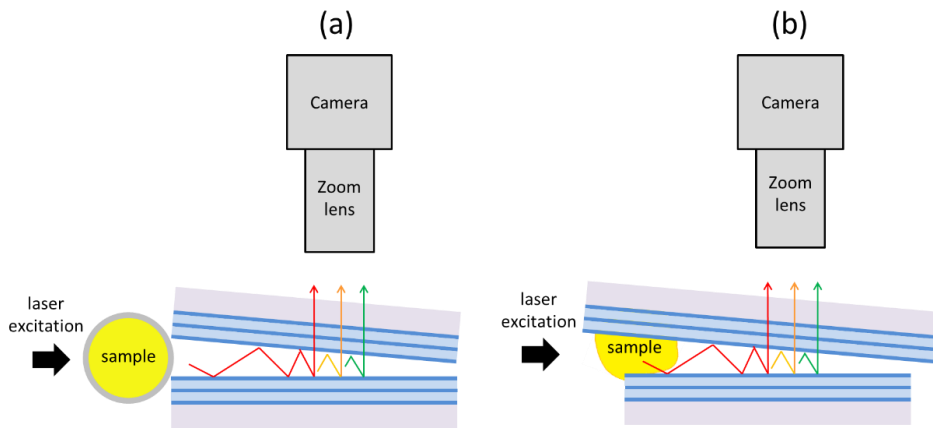


Figure 6.5 – Schematic illustration of ray guidance in a slowly tapered hollow Bragg waveguide. Light within the omnidirectional band of the mirrors is adiabatically transformed from a guided mode to a vertical Fabry-Perot mode at cutoff. (a) Capillary filled with microspheres aligned near wide end of the taper (b) Fluorescent microspheres inserted into the taper cavity.

6.3.1 Fluorescence coupled from a glass capillary

To evaluate the performance of the tapers as waveguide-coupled spectrometers, a capillary filled with a 0.4% solids (6.8×10^{13} particles/mL) solution of ~ 48 nm diameter Yellow-Green (505 Ex/515 Em) FluoSpheres was aligned near the wide end of a taper and excited with a 445 nm laser. The taper (sample H4.2) had a

starting core height of ~5.9 μm and a taper slope of ~1.5 μm/mm. A sputtered mirror on a ~4.7 mm long quartz substrate and an evaporated mirror on a ~4 mm long Si substrate were used to fabricate the taper.

Table 6.1 shows the Fluorescein equivalents for Yellow-Green FluoSpheres of different diameters. Using the tabulated value for the Fluorescein equivalents of the 0.04 μm particles, the approximate molarity of the Yellow-Green FluoSphere solution was calculated:

$$Molarity = \frac{350 \text{ Fluorescein equivs.}}{1 \text{ microsphere}} \cdot \frac{6.8 \times 10^{16} \text{ microspheres}}{L} \cdot \frac{1 \text{ mol}}{6.022 \times 10^{23}}$$

$$Molarity = 0.0395 \text{ mM} \quad (6.1)$$

Table 6.1 – Fluorescein equivalents for yellow-green FluoSpheres of different sizes. Adapted from Ref. [1].

Fluorescein equivalents in our yellow-green fluorescent FluoSpheres® beads.

Microsphere Diameter (μm)	Fluorescein Equivalents per Microsphere
0.02	1.8 × 10 ²
0.04	3.5 × 10 ²
0.1	7.4 × 10 ³
0.2	1.1 × 10 ⁵
0.5	2.0 × 10 ⁶
1.0	1.3 × 10 ⁷
2.0	3.1 × 10 ⁷
10	1.1 × 10 ¹⁰
15	3.7 × 10 ¹⁰

Due to the relatively low coupling efficiency for fluorescence from the capillary into the wide end of the taper, a 500 nm long-pass filter (FELH0500, Thorlabs) was placed in front of the camera to suppress scattered laser light. Figure 6.6(a) shows an image of the guided fluorescence reaching cutoff for mode orders $m = 2$ to $m = 5$. A 543 nm laser was used in conjunction with a 594 nm laser

to map the pixels to their respective wavelengths. The raw taper spectra for these mode orders, taking the QE of the CCD into account, are plotted in Fig. 6.6(b).

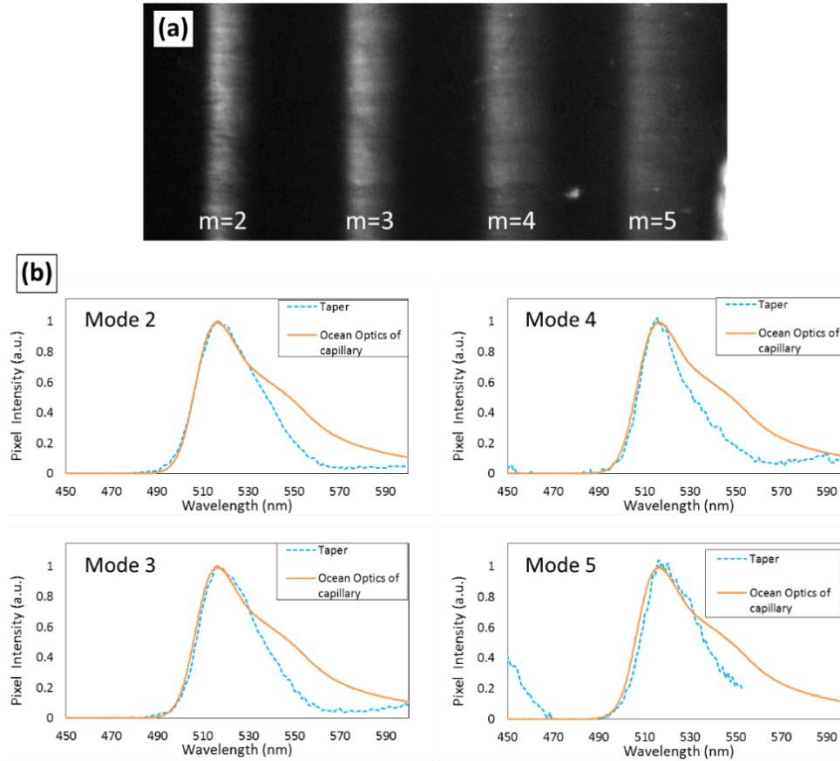


Figure 6.6 – (a) Spectrally-resolved fluorescence from a capillary filled with Yellow-Green (505/515) FluoSpheres, aligned near the wide end of a taper. Fluorescence associated with mode orders $m = 2$ to $m = 5$ are shown. (b) Extracted taper spectra for mode orders $m = 2$ to $m = 5$. Compared to a reference scan of the capillary, the extracted taper spectra are modified by the ‘instrument response’ of the taper.

Compared to the emission spectrum collected by a commercial spectrometer, the raw taper spectrum is missing spectral content for wavelengths above ~ 570 nm. This is due to the inherent suppression of out-of-band light due to very high waveguide loss. Therefore, unlike the conventional LVF configuration above, the spectrum produced by the taper is not affected by out-of-band leakage of light at longer wavelengths.

To reach the cutoff point, (especially for the lower order modes) light must lie within the omnidirectional band of the mirrors. As discussed in Chapter 5, the operating range of the taper spectrometer is defined by the radiated power of the guided modes at cutoff. This creates a pass-band for light delivered to the detection point (and strong suppression of out-of-band light), which is a significant advantage of the waveguide geometry. This pass-band is not flat however, a fact which must be taken into account when comparing the taper spectrum to the commercial spectrometer spectrum. Recall from Chapter 5 that the shape of the pass-band may be accounted for by defining an approximate ‘instrument response’ correction function for the tapers:

$$C_T(\lambda) = S_C(\lambda) / S_T(\lambda) \quad (6.2)$$

Here, S_T is the raw spectrum obtained from a plot of the pixel intensity and S_C is the reference spectrum (known, or obtained using the commercial spectrometer).

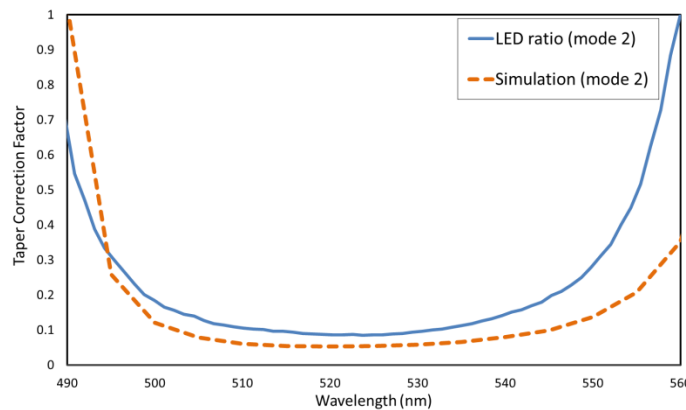


Figure 6.7 – Plot of the correction function $C_T(\lambda)$ for a taper, estimated using the simulated relative power of light radiated at cutoff, for different wavelengths. Also plotted is the correction function obtained using the white LED data.

Figure 6.7 shows an estimate of the correction function for a particular taper (sample H4.2), using light from a white LED (repeated from Fig. 5.14). Also shown is a theoretical estimate of the correction function, using a simulation of the radiated power for a guided mode at cutoff (see Chapter 5). In a completely analogous fashion, raw data collected by a commercial spectrometer is multiplied by a correction factor:

$$C_S(\lambda) = S_C(\lambda)/S_R(\lambda) \quad (6.3)$$

where S_R is the raw (uncorrected) spectral response, S_C is the corrected spectral response, and C_S is the correction factor to be applied to raw spectrometer data.

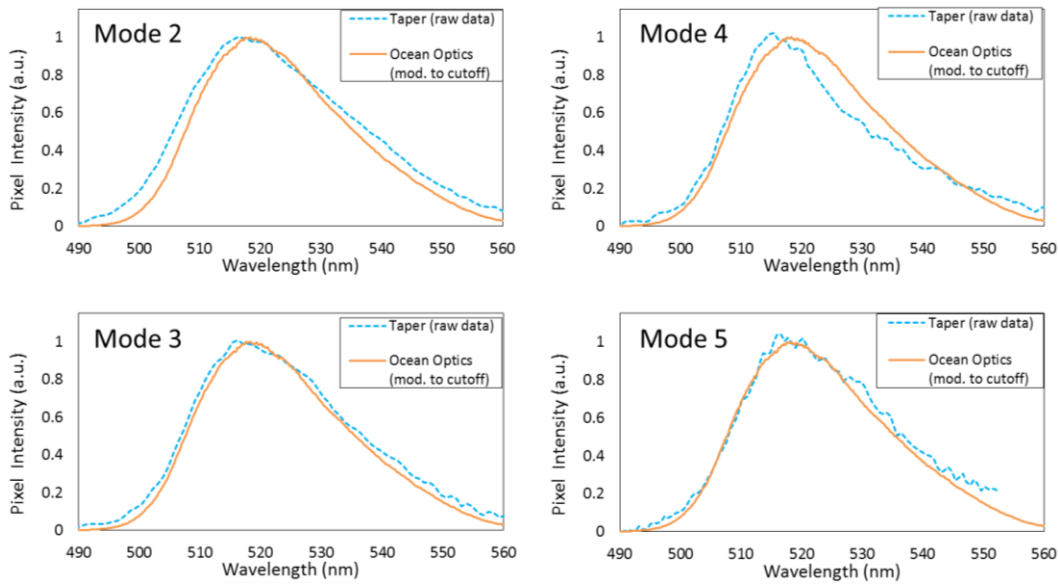


Figure 6.8 – Extracted taper spectra for mode orders $m = 2$ to $m = 5$ (see Fig. 6.6(a)). The reference scan of the capillary was divided by the correction function of the taper to help assess the validity of the results. The modified emission spectrum and experimental data agree well for the mode orders shown.

To first verify that the raw taper spectrum results are reasonable, the reference emission spectrum was divided by the correction function for the taper.

This allows for a direct comparison with the raw taper spectrum. The results for several mode orders are shown in Fig. 6.8. The modified emission spectrum is in good agreement with all of the graphed mode orders.

For practical use of the taper as a spectrometer, it is actually the opposite normalization process that needs to be carried out. In other words, the raw taper spectrum needs to be multiplied by the taper correction function. This removes the ‘instrument response’ of the taper from the spectrum, hopefully providing an accurate representation of the emission spectrum of the FluoSpheres. The results of such a normalization, using the experimentally determined taper correction function from Fig. 6.7, are shown for mode orders $m = 2$ to $m = 5$ in Fig. 6.9.

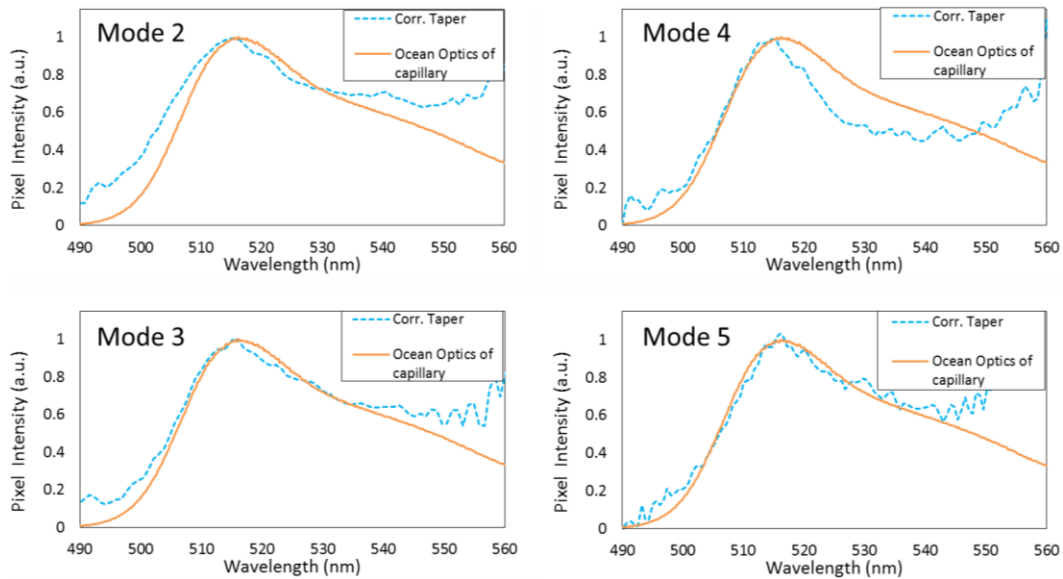


Figure 6.9 – Corrected taper spectra for mode orders $m = 2$ to $m = 5$ (see Fig. 6.6(a)). In this case, the raw taper spectra were multiplied by the experimentally determined correction function of the taper to obtain a more accurate representation of the fluorescence spectrum. Within the operating range of the taper, the extracted spectra agree relatively well with the spectrum measured by a commercial spectrometer. Near the edges of the operating range, decreased detection sensitivity leads to a less accurate representation of the spectra.

Within the operating range of the taper, the emission spectrum collected by the taper mostly agrees well with the spectrum measured by the commercial spectrometer. However, spectral content measured close to the edges of the taper operating range are much less reliable due to the low sensitivity of the taper spectrometer there. Specifically, since the normalization involves the multiplication of the raw data by the taper correction function data (on a point-by-point basis), the result becomes unreliable in the wavelength range where the correction function begins to change rapidly.

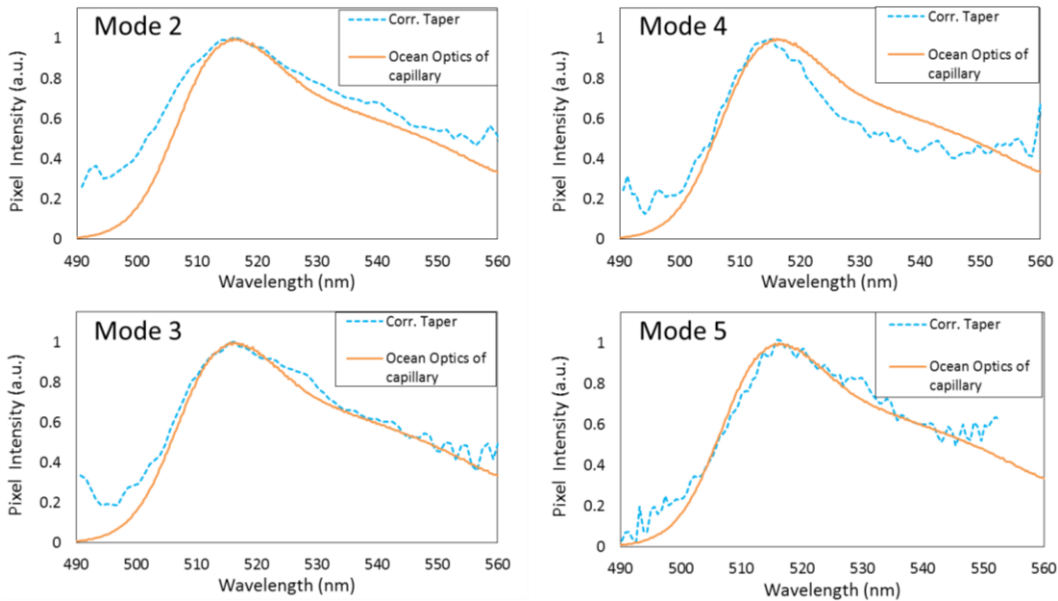


Figure 6.10 – Corrected taper spectra for mode orders $m = 2$ to $m = 5$ (see Fig. 6.6(a)). The raw taper spectra were multiplied by the theoretically determined correction function of the taper. In this case, the extracted spectra are in agreement with the commercial spectrometer measurement over a wider wavelength range compared to the results in Fig. 6.9. Nevertheless, decreased detection sensitivity near the edges of the operating range still hampers the ability to reproduce an accurate spectrum there.

Figure 6.10 shows the extracted taper spectra, this time using the theoretically determined correction function (see Fig. 6.7) to normalize the raw

data. In this case, the extracted spectra are in agreement with the commercial spectrometer measurement over a wider wavelength range. However, decreased detection sensitivity near the edges of the operating range still hampers the ability to reproduce an accurate spectrum there.

6.3.2 Fluorescent microsphere insertion into taper cavity

In an attempt to increase efficiency, rather than collecting fluorescence from a glass capillary, microspheres were inserted directly into a taper cavity. This taper (sample 5.6) had a starting core height of $\sim 2.1 \mu\text{m}$ and a taper slope of $\sim 0.7 \mu\text{m}/\text{mm}$. Sputtered mirrors on quartz substrates $\sim 4.7 \text{ mm}$ and $\sim 3.7 \text{ mm}$ in length were used to fabricate the taper. In a first attempt, a 0.5% solids (8.2×10^{13} particles/mL) solution of $\sim 48 \text{ nm}$ diameter Orange (540 Ex/560 Em) FluoSpheres was inserted into the wide end of the taper, shown in Fig. 6.11.

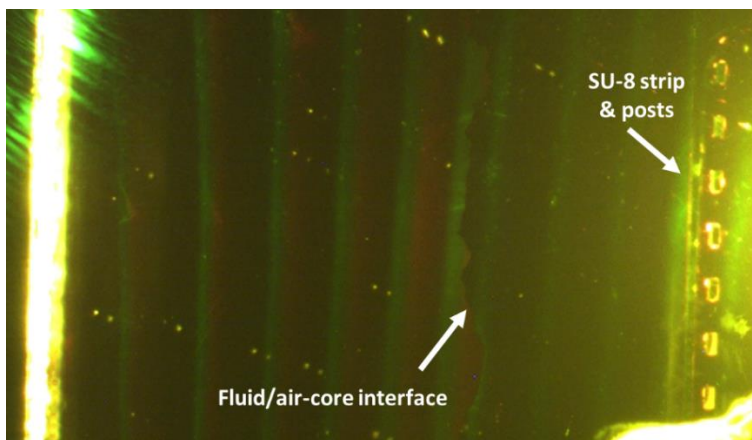


Figure 6.11 – A 0.5% solids (8.2×10^{13} particles/mL) solution of $\sim 48 \text{ nm}$ diameter Orange (540 Ex/560 Em) FluoSpheres was inserted into the wide end of the taper. A long strip of SU-8 and a row of rectangular Su-8 posts are visible on the right side of the image (i.e. the wide end of the taper). The image is filled with a yellow tinge due to stray fluorescence. The FluoSpheres were not confined to the wide end of the taper (as intended), instead collecting towards the narrow end.

Towards the right side of the image, a row of rectangular SU-8 posts and a long SU-8 strip mark the wide end of the taper. A 532 nm laser was used to excite the FluoSpheres and a 550 LP filter was placed in front of the camera to suppress excitation light. This image illustrates some practical challenges associated with using these tapers for a fluorescence LOC device. First, the entire image has a yellow tinge to it. This is due to stray fluorescent light from the edges of the taper chip, as well as from fluorescent microspheres that have not been successfully inserted into the taper core. Subsequent taper chips incorporated an overhang (see Chapter 4, Fig. 4.9) at the wide and narrow ends of the taper to help suppress the stray fluorescence.

Another problem was that the FluoSpheres were not successfully contained to the wide end of the taper cavity by the long SU-8 strip. Over the course of a few minutes, the microsphere solution was slowly drawn in and collected at the narrow end of the taper. This is evident in the change in spacing of the fluorescent bands towards the centre of the image, indicating a change in core refractive index. The boundary between the air- and fluid-filled taper regions is indicated for the particular case shown in Fig. 6.11.

To better confine the fluorescent microspheres to the wide end of the taper a second experiment was conducted. This time, the 0.5% solids solution of Orange FluoSpheres was mixed with an UV-curable optical adhesive (NOA 61, Norland) rather than with distilled water. An image of the resulting fluorescent bands is shown in Fig. 6.12. The taper (sample 6.6) used here was fabricated with

overhangs on both ends to help reduce stray fluorescence, as mentioned above. The taper had a starting core height of $\sim 2.1 \mu\text{m}$ and a taper slope of $\sim 0.6 \mu\text{m}/\text{mm}$. Sputtered mirrors on quartz substrates $\sim 3.7 \text{ mm}$ and $\sim 5.7 \text{ mm}$ in length were used to fabricate the taper.

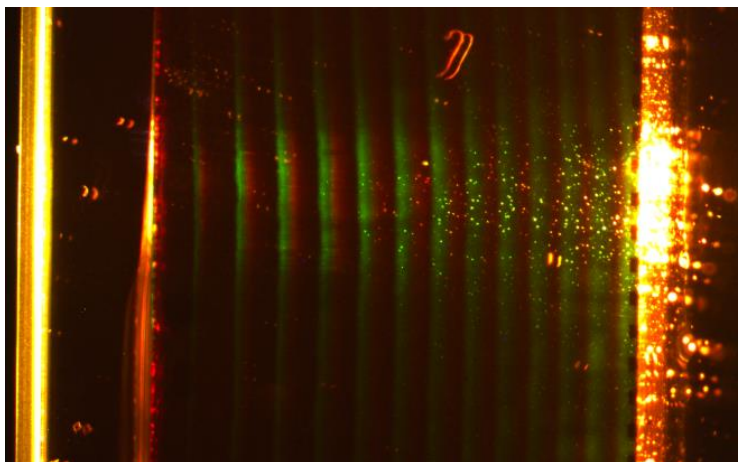


Figure 6.12 – A 0.5% solids solution of $\sim 48 \text{ nm}$ diameter Orange (540 Ex/560 Em) FluoSpheres was mixed with an UV-curable optical adhesive (NOA 61, Norland) instead of distilled water, then inserted into the wide end of a taper (at right). Clumping of the microspheres is made apparent by the presence of bright spots. As well, the microspheres infiltrated farther into the taper cavity than desired.

Clumping of the microspheres in the adhesive-water mixture causes the fluorescing microspheres to appear as bright spots. A more uniform distribution of microspheres may be achieved by letting the water in the mixture evaporate before insertion into the taper cavity. Even with the optical adhesive mixture, the microspheres infiltrated farther than desired into the taper cavity. Curing the optical adhesive faster would help to fix this. Incorporating these improvements, another taper sample (sample 6.5) was prepared and infiltrated with an adhesive-

microsphere mixture. A 532 nm laser and a 550 LP filter were again used in this setup. An image of the resulting fluorescent bands is shown in Fig. 6.13.



Figure 6.13 – A 0.5% solids solution of ~ 48 nm diameter Orange (540 Ex/560 Em) FluoSpheres mixed with optical adhesive, with the water evaporated, was inserted into the wide end of a taper (at right). The result is a much more uniform distribution of microspheres suspended in optical adhesive. The evaporation of the water also helped to increase the viscosity of the mixture, preventing the mixture from infiltrating too far into the taper cavity before being cured.

The adhesive-microsphere mixture was successfully confined to the wide end of the taper in this case, maintaining an air-core cavity for the lowest few mode orders at the left side of the image. This is crucial in order to take advantage of the benefits of a waveguide-coupled spectrometer, such as strong rejection of out-of-band light.

A more straightforward way to keep the microspheres at the wide end of the taper is to simply use microspheres with a large enough diameter so that they get lodged towards the front of the taper cavity. Yellow-green (505 Ex/515 Em) FluoSpheres with a diameter of $4.1 \mu\text{m}$ were chosen for experiments involving

tapers with a starting core height of 5.9 μm . Therefore, the microspheres are expected to be confined to the first third of the cavity.

A solution of the 4.1 μm FluoSpheres was diluted to a concentration of 0.57 particles/ μL , so that only a few individual FluoSpheres would become lodged in the taper cavity. The taper (sample H4.1) used in this experiment had a starting core height of $\sim 5.9 \mu\text{m}$ and a taper slope of $\sim 1.5 \mu\text{m}/\text{mm}$. A sputtered mirror on a $\sim 4.7 \text{ mm}$ long quartz substrate and an evaporated mirror on a $\sim 4 \text{ mm}$ long Si substrate were used to fabricate the taper. Extrapolating the Fluorescein equivalents data from Table 6.1, each 4.1 μm FluoSphere contains at least 2.5×10^8 Fluorescein equivalents (less than 1 femtoMole).

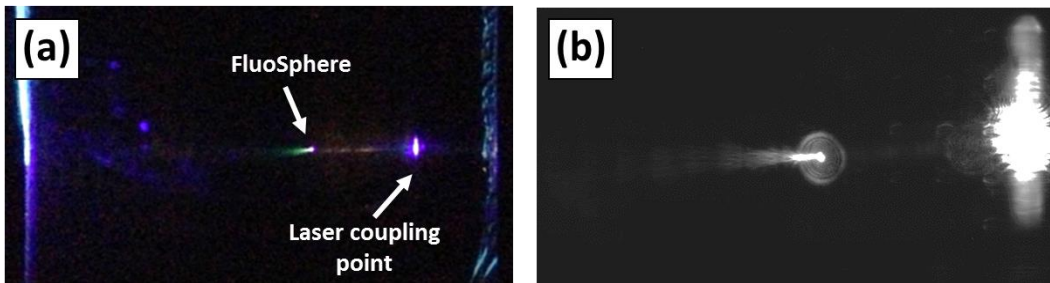


Figure 6.14 – A single 4.1 μm Yellow-Green (505/515) FluoSphere that was lodged in a taper cavity. (a) The coupling point of the 374 nm laser (underneath the overhang), as well as the fluorescence from the microsphere are visible. (b) The fluorescence appears to be coupling into cutoff points for mode orders near where the microsphere is lodged.

Figure 6.14 shows a single FluoSphere being excited by a 374 nm laser. The yellow-green fluorescence from the microsphere, as well as the laser coupling point, is visible in the image in Fig. 6.14(a). In Fig. 6.14(b), it appears that the fluorescence from the microsphere is reaching cutoff for mode orders with cutoff points near where the particle is positioned. Unfortunately, the sensitivity of this

particular setup was not sufficient to extract any fluorescence spectral data from the image.

Another taper (sample H4.2) was prepared, again with a few 4.1 μm Yellow-Green FluoSpheres lodged about a third of the way into the taper cavity. Using a 20x objective lens, a 473 nm laser beam was coupled into the wide end of the taper. The laser was carefully focused onto a pair of closely-spaced FluoSpheres, causing them to fluoresce, shown in Fig. 6.15. The pair of Fluospheres appear as a single bright spot in Fig. 6.15(a), due to a 2-second exposure time. The wide end of the taper is indicated by the illuminated SU-8 posts, which are visible on the right side of the image. Figure 6.15(b) shows an image of the pair of fluorescing FluoSpheres with a shorter exposure time. As mentioned above, these two Fluospheres are estimated to each contain at least 2.5×10^8 Fluorescein equivalents. The known post array dimensions were used to set the scale for the images in Fig. 6.15.

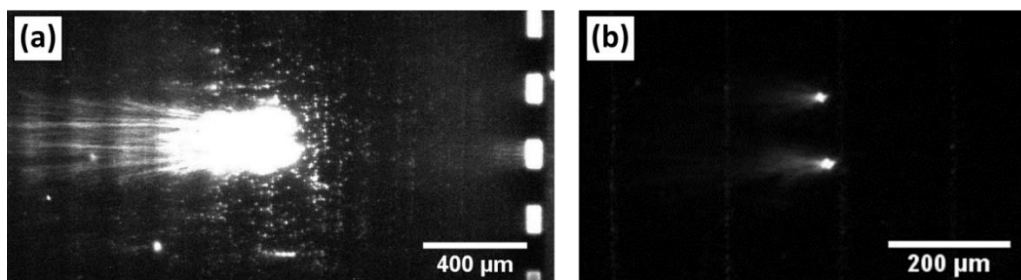


Figure 6.15 – Using a 20x objective lens, a 473 nm laser beam was coupled into the wide end of the taper. The laser was carefully focused onto a pair of closely-spaced 4.1 μm Yellow-Green FluoSpheres, causing them to fluoresce. (a) A 2-second exposure time causes the pair of FluoSpheres to appear as a single bright spot. The wide end of the taper is indicated by the illuminated SU-8 posts on the right side of the image. (b) An image of the pair of fluorescing FluoSpheres with a shorter exposure time. These two FluoSpheres are estimated to each contain at least 2.5×10^8 Fluorescein equivalents.

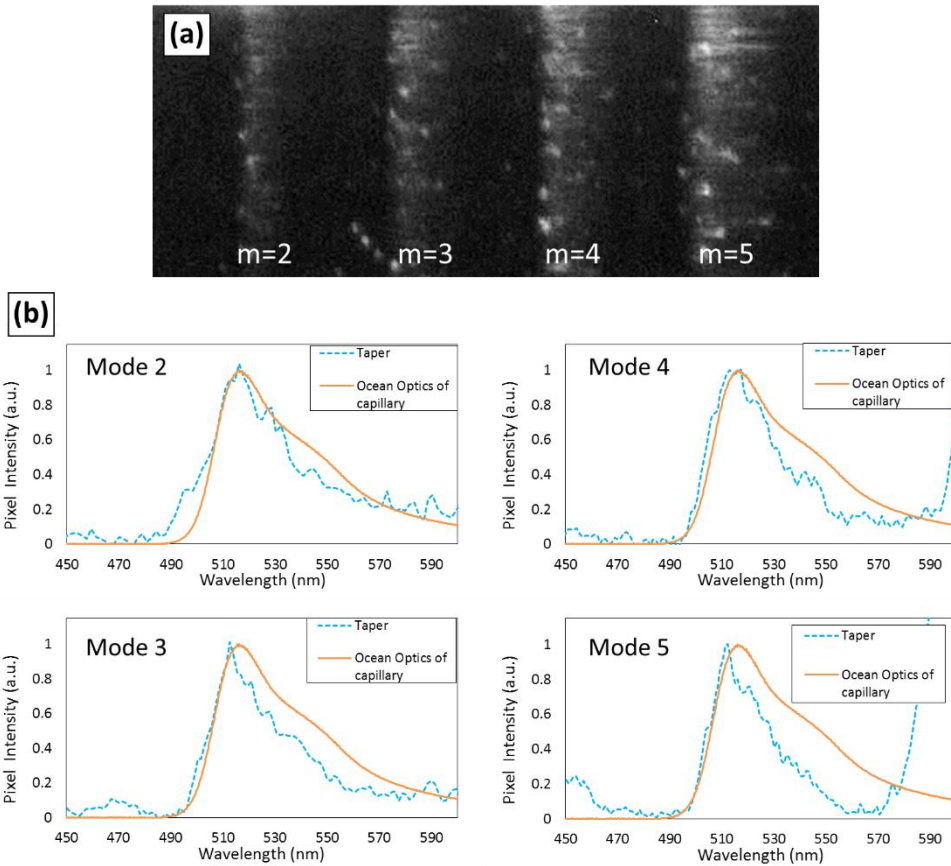


Figure 6.16 – Spectrally-resolved fluorescence from a pair of Yellow-Green (505/515) FluoSpheres of 4.1 μm diameter, lodged part-way into the taper cavity. Fluorescence associated with mode orders $m = 2$ to $m = 5$ is shown. Bright spots are likely due to scattering of stray light (b) Extracted raw taper spectra for mode orders $m = 2$ to $m = 5$.

The microsphere fluorescence coupled into guiding modes of the tapered waveguide, reaching cutoff for modes towards the narrow end of the taper. Using a 500 nm long-pass filter to block excitation light, Fig. 6.16(a) shows an image of fluorescence associated with mode orders $m = 2$ to $m = 5$. The bright spots are most likely due to stray light scattering in the quartz substrate. These will cause noise in the extracted spectra. Figure 6.16(b) shows the extracted taper spectra for mode orders $m = 2$ to $m = 5$. As before, the extracted taper spectra are modulated by the correction function of the taper. Successfully removing this

'instrument response' from the data should provide a more accurate representation of the fluorescence spectra.

Figure 6.17 shows the corrected taper spectra for mode orders $m = 2$ to $m = 5$, where the extracted spectra were multiplied by the theoretically determined correction function (see Fig. 6.7). In this case, the correction function has actually decreased the quality of the extracted spectra. As before (see Fig. 6.10), decreased sensitivity on the edges of the operating range results in a poor reproduction of the fluorescence spectrum there. In addition, a lower signal-to-noise ratio (SNR) and low amplitude of the detected signal further decreased the reliability of using the correction factor. Collecting a cleaner fluorescence spectrum (i.e. eliminating scattering centres in the quartz) and increasing collection efficiency would help to improve the quality of the measured spectra.

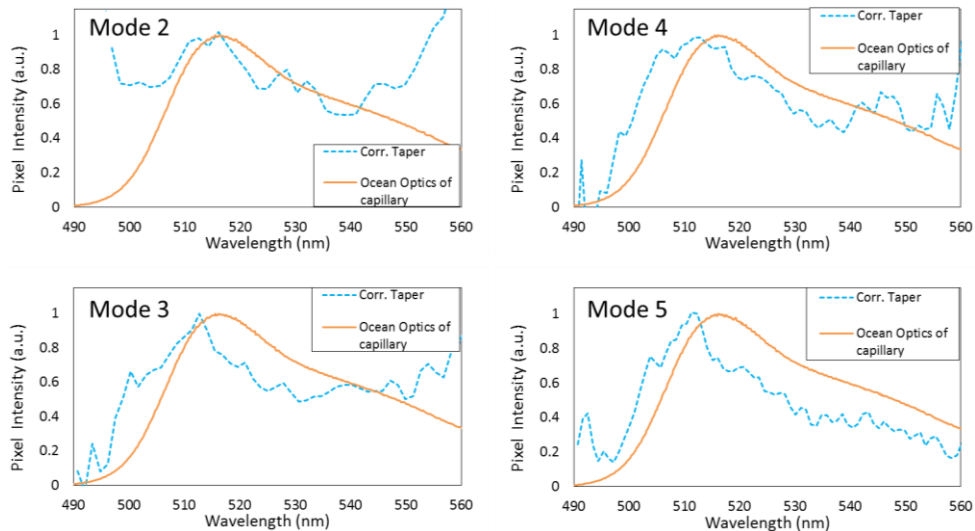


Figure 6.17 – Corrected taper spectra for mode orders $m = 2$ to $m = 5$ (see Fig. 6.15(a)). The raw taper spectra were multiplied by the theoretically determined correction function of the taper. Decreased sensitivity on the edges of the operating range results in a poor reproduction of the fluorescence spectrum in there. As well, the correction process is hampered by a low signal-to-noise ratio and roughness in the measured spectra.

6.4 Conclusions

The air-core waveguide taper spectrometers described in Chapter 5 were implemented in a prototype fluorescence sensing system. The tapers were employed in both a conventional LVF spectrometer configuration and a waveguide-coupled spectrometer configuration. In both cases, low-NA collection optics are required in order to optimize resolution. As a LVF, the tapers are able to reproduce a reasonably accurate emission spectrum within the normal-incidence high-reflectance band of the mirrors. However, without external filters, leakage of out-of-band light is a major issue. In the waveguide configuration, out-of-band light is not well guided, and is thus inherently suppressed prior to the detection point, without the need for external filters. Using waveguide-coupled fluorescence from a capillary, the spectrum measured within the operating range of the taper agreed reasonably well with that collected by a commercial spectrometer. Additionally, methods were developed for infiltrating solutions of microspheres into the taper cavity, as well as lodging individual microspheres near the front of the cavity. Using waveguide-coupled fluorescence from a pair of microspheres lodged in the taper cavity, raw extracted spectra within the taper's operating range agreed fairly well with the spectrum from a commercial spectrometer. However, due to low SNR, the correction function of the taper did not help to improve the accuracy of the extracted spectra. Additionally, there is significant scope for the implementation of mirrors with a wider omnidirectional band, as well as the use of more sophisticated fluidics and improved collection

optics. Future work should focus on exploring some of these details and also to further quantify the detection limit of the taper LOC setup.

6.5 Works Cited

- [1] "FluoSpheres Fluorescent Microspheres," *Molecular Probes, Invitrogen detection technologies*. [Online]. Available: <http://tools.lifetechnologies.com/content/sfs/manuals/mp05000.pdf>.
- [2] A. Emadi, H. Wu, G. de Graaf, and R. Wolffenbuttel, "Design and implementation of a sub-nm resolution microspectrometer based on a Linear-Variable Optical Filter.," *Opt. Express*, vol. 20, no. 1, pp. 489–507, Jan. 2012.
- [3] O. Schmidt, P. Kiesel, and M. Bassler, "Performance of chip-size wavelength detectors.," *Opt. Express*, vol. 15, no. 15, pp. 9701–6, Jul. 2007.
- [4] N. Ponnampalam and R. G. DeCorby, "Out-of-plane coupling at mode cutoff in tapered hollow waveguides with omnidirectional reflector claddings.," *Opt. Express*, vol. 16, no. 5, pp. 2894–908, Mar. 2008.
- [5] R. G. DeCorby, N. Ponnampalam, E. Epp, T. Allen, and J. N. McMullin, "Chip-scale spectrometry based on tapered hollow Bragg waveguides," *Opt. Express*, vol. 17, no. 19, pp. 16632–16645, 2009.

7 Conclusions

7.1 Summary

The goal of this thesis was to develop tapered air-core Bragg waveguides for use as integrated micro-spectrometers in lab-on-a-chip systems. This project resulted in several relevant contributions to the future development of these systems, including:

- Adapting the hollow waveguide buckling technique previously reported by our group [1] to use $\text{TiO}_2/\text{SiO}_2$ multilayers for operation in the visible range;
- The fabrication of novel tapered air-core waveguides using a versatile wafer-bonding process; and
- Integrating the tapered air-core Bragg waveguides into a prototype fluorescence sensing system, where the fluorescent spectrum of individual FluoSpheres was successfully measured within the operational band of the tapers.

7.1.1 Fabrication process for tapered air-core waveguides

Tapered waveguides were fabricated for operation in the visible range. $\text{TiO}_2/\text{SiO}_2$ cladding mirrors were deposited using both e-beam evaporation and reactive sputter deposition, outlined in Chapter 3. Both deposition methods resulted in films of good optical quality; however, the sputtering recipe was tailored to grow compressively stressed films for waveguides fabricated by buckling self-assembly.

These sputtered films showed promise in buckling experiments, but current samples have insufficient compressive stress to produce fully-buckled, usable hollow waveguides.

We also developed a taper fabrication process by manually assembling slab Bragg waveguide tapers by wafer-bonding. This process is both versatile and reliable, allowing for the use of evaporated or sputtered cladding mirrors, deposited onto glass, quartz, or silicon substrates. Additionally, the taper dimensions are easy to change, allowing for optimal tailoring to the omnidirectional band of the Bragg mirrors.

By bonding two cladding mirrors with substrates of differing length, a fluid-insertion platform was formed at the wide end of the taper. By simply placing a droplet of solution containing fluorescent microspheres here, the fluorescent sample is drawn inside the taper cavity. The sample may be confined to the wide end of the taper cavity either by defining a barrier with a long strip of SU-8 or by choosing microspheres large enough to become lodged in the cavity.

Fluidics platforms were also developed for the buckled hollow waveguide chips, summarized in Chapter 4. Although the buckled hollow waveguides offer unique functionality for lab-on-a-chip systems, developing an appropriate microfluidics platform has proven difficult. Two PDMS wells were fabricated directly on a buckled waveguide chip, with one positioned at each open end of a buckled waveguide. By placing a syringe in one well, fluid was successfully

transported through the hollow waveguide channel into the other well. However, the applied force required to do so was enough to cause non-trivial leakage problems between the Si and PDMS substrates. Further improvements in the fabrication of this PDMS platform are required.

7.1.2 Tapered air-core waveguide spectrometers for lab-on-a-chip devices

There are a variety of optical sensing methods available to use in lab-on-a-chip systems, but fluorescence detection is by far the most ubiquitous. The Bragg claddings of our tapered air-core waveguides were designed for operation in the visible range for this reason. By using a $\text{TiO}_2/\text{SiO}_2$ periodic multilayer and a quarter-wave-stack condition, these mirrors provide an omnidirectional reflection band for TE-polarized light, covering the wavelength range from ~ 490 nm to ~ 570 nm. For tapers made from evaporated mirrors, most mode orders exhibited wavelength resolutions of ~ 2 nm, with a relative insensitivity regarding mode order. On the other hand, tapers fabricated using mirrors sputtered on quartz had experimental resolutions ranging from ~ 2.2 nm to ~ 0.8 nm, for mode orders $m = 1$ to $m = 8$, respectively. Subsequent experiments with white light sources determined a usable operational bandwidth of ~ 70 nm, with peak sensitivity centred at ~ 520 nm. Simulations of radiated power of guided modes versus position along the taper corroborated these results. These resolutions and range of operation are in line with, and sometimes better than, similar chip-size spectrometers this author found in the literature [2], [3].

The air-core waveguide taper spectrometers were implemented in a prototype fluorescence sensing system. The tapers were first used in a conventional LVF configuration, where some of the drawbacks of this setup became apparent. Interference from out-of-band light caused a large discrepancy in the measured spectrum for longer wavelengths. A short-pass filter to suppress the out-of-band light would help to improve the measured fluorescence spectrum.

The tapers were also used as side-coupled LVFs. In this configuration, out-of-band light is inherently suppressed and is not significantly present in the collected fluorescence spectrum. Using waveguide-coupled fluorescence from a capillary, the measured spectra agreed well with the reference spectrum within the operating range of the taper. As well, using the fluorescence from a pair of 4.1 μm FluoSpheres lodged inside the taper cavity, fluorescence spectra were successfully measured. In this case, lower SNR resulted in slightly poorer agreement with the reference spectrum.

7.2 Future work

7.2.1 Improvements in operating range and taper fabrication processes

There is significant scope for improving the operating range of the tapers, as well as refining both the wafer-bonding and the buckling self-assembly taper fabrication processes. Firstly, SiO_2 and TiO_2 were used for the cladding layers because they were the best choices readily available. A different pairing, such as SiO_2 and GaP has a higher index contrast [4] and could help create an operational

band spanning nearly the entire visible range. In the same vein, a quarter-wave-stack design was chosen for its relative simplicity. A wider operational band may be achieved by choosing a more complex multilayer design with more layers.

For future work, our research group may want to focus on improving the buckling yield of the visible band hollow waveguides, namely by increasing the compressive film stress. One potential way to do this would be to increase the deposition temperature or to thermally anneal the films [5]. Alternatively, we have had limited success with increasing film stress in the $\text{TiO}_2/\text{SiO}_2$ multilayers by depositing a thin W layer on top. Experimenting with the type of metal used and the layer thickness could lead to improved buckling results. There is also merit to exploring alternatives to the fluorocarbon low-adhesion layer, such as patterning a thin photoresist layer to define the waveguides, then performing sacrificial etching to induce buckling.

Some fluorescence experiment results suffered from scattering of stray light in the glass or quartz layers. The addition of an aperture at the wide end of the taper would help to prevent light from coupling into the glass and quartz substrates. One possible method for accomplishing this would be to deposit a patterned metal film on the side edges of the glass and quartz substrates

7.2.2 Fluorescence experiments

There are still a number of interesting experiments that could be done with the prototype fluorescence sensing device. For example, the mainly TE-polarized

nature of these tapers could be exploited to isolate excitation and emission light [6]. As well, detection limit experiments should be done to quantify the sensitivity of the fluorescence detection setup. There would also be some utility in setting up an experiment to try to distinguish two different fluorescent signals.

7.3 Works cited

- [1] E. Epp, N. Ponnampalam, W. Newman, B. Drobot, J. N. McMullin, A. F. Meldrum, and R. G. DeCorby, "Hollow Bragg waveguides fabricated by controlled buckling of Si/SiO₂ multilayers," *Opt. Express*, vol. 18, no. 24, pp. 24917–24925, Nov. 2010.
- [2] A. Emadi, H. Wu, G. de Graaf, and R. Wolffenbuttel, "Design and implementation of a sub-nm resolution microspectrometer based on a Linear-Variable Optical Filter.," *Opt. Express*, vol. 20, no. 1, pp. 489–507, Jan. 2012.
- [3] Z. Hu, A. Glidle, C. N. Ironside, M. Sorel, M. J. Strain, J. Cooper, and H. Yin, "Integrated microspectrometer for fluorescence based analysis in a microfluidic format.," *Lab Chip*, vol. 12, no. 16, pp. 2850–7, Aug. 2012.
- [4] J. Gao, A. M. Sarangan, and Q. Zhan, "Experimental confirmation of strong fluorescence enhancement using one-dimensional GaP/SiO₂ photonic band gap structure," *Opt. Mater. Express*, vol. 1, no. 7, p. 1216, Oct. 2011.
- [5] H.-C. Chen, K.-S. Lee, and C.-C. Lee, "Annealing dependence of residual stress and optical properties of TiO₂ thin film deposited by different deposition methods.," *Appl. Opt.*, vol. 47, no. 13, pp. C284–7, May 2008.
- [6] A. Banerjee, A. Pais, I. Papautsky, and D. Klotzkin, "A Polarization Isolation Method for High-Sensitivity, Low-Cost On-Chip Fluorescence Detection for Microfluidic Lab-on-a-Chip," *IEEE Sens. J.*, vol. 8, no. 5, pp. 621–627, May 2008.

Appendix A: MATLAB code

Shown below is the MATLAB code used to simulate the radiated power versus position along a tapered hollow Bragg waveguide, using an effective-index transfer matrix model:

```
1 % An m-file to plot the power loss per unit length versus length of a
2 % tapered hollow Bragg waveguide
3 %
4 % Definitions / Inputs
5 % daVc=vector of core height imported from a previously executed file such
6 %     as TiO2BraggRadTE0.m, which calculates the loss of hollow waveguide as a
7 %     function of core height.
8 % neffTEv=vector of effective indices from previous file
9 % Ate2v=vector of intensity attenuation coefficients from previous file
10 % ST=taper slope, assumed constant (ie. linear taper) and defined positive
11 % in terms of change in taper height divided by distance along taper
12 %
13 %
14 % Define vector of points along the taper, based on the core height vector
15 clear all
16 lambda=[485e-9:10e-9:585e-9];
17 lengthlambda=length(lambda);
18
19 for qy=1:lengthlambda
20
21     clearvars -except lambda lengthlambda qy
22     TiO2BraggRadTE2_mismatch;
23
24     ST=0.0015; % taper slope (core height divided by waveguide length)
25     daVmax=daVc(1);
26     k0=2*pi/lambda0;
27     daVz=daVc;
28     ld=length(daVc);
29     zz=length(daVz);
30     zt=(daVmax-daVz)./ST; %vector of position points along the taper
31     ztmm=1e3*zt;
32     tz(1)=zt(2)-zt(1);
33     for qt=2:length(zt)
34         tz(qt)=zt(qt)-zt(qt-1); %vector of effective 'layer' thicknesses
35     end
36 %
37     kz=Ate2v.*lambda0./(4.*pi);%vector of effective extinction coefficients along taper
38     nz=neffTEv; %vector of effective indices along taper
39     Nz=nz-i.*kz;
40 %
41 % calculate transfer matrix for the last layer and interface
42 %
43     nL=Nz(zz);
44     mtaper=[exp(i*k0*Nz(zz)*tz(zz)) 0; 0 exp(-i*k0*Nz(zz)*tz(zz))]*(1/(2*Nz(zz)))*[Nz(
45     zz)+nL Nz(zz)-nL; Nz(zz)-nL Nz(zz)+nL];
46     mp11(zz)=mtaper(1,1);
47     mp21(zz)=mtaper(2,1);
48 %
```

```

49 % calculate transfer matrix for middle section
50 %
51 for qz=zz-1:-1:2
52 mtaper=[exp(i*k0*Nz(qz)*tz(qz)) 0; 0 exp(-i*k0*Nz(qz)*tz(qz))]*(1/(2*Nz(qz)))*[Nz(k
(qz)+Nz(qz+1) Nz(qz)-Nz(qz+1); Nz(qz)-Nz(qz+1) Nz(qz)+Nz(qz+1)]*mtaper;
53 mp11(qz)=mtaper(1,1);
54 mp21(qz)=mtaper(2,1);
55 end
56 %
57 % calculate transfer matrix for the first interface and layer and interface
58 %
59 n0=Nz(1);
60 mtaper=[exp(i*k0*Nz(1)*tz(1)) 0; 0 exp(-i*k0*Nz(1)*tz(1))]*(1/(2*Nz(1)))*[Nz(1)+Nz(k
(2) Nz(1)-Nz(2); Nz(1)-Nz(2) Nz(1)+Nz(2)]*mtaper;
61 mp11(1)=mtaper(1,1);
62 mp21(1)=mtaper(2,1);
63 mtaper=(1/(2*n0))*[n0+Nz(1) n0-Nz(1); n0-Nz(1) n0+Nz(1)]*mtaper;
64 m11=mtaper(1,1);
65 m21=mtaper(2,1);
66 %
67 % CALCULATE SIGNAL FIELD from transfer matrices
68 for qq=1:zz
69 Ep(qq)=mp11(qq)/m11;
70 Em(qq)=mp21(qq)/m11;
71 Etot(qq)=Ep(qq)+Em(qq);
72 end
73 %
74 Ip=Ep.*conj(Ep);%vector of forward traveling intensity
75 Im=Em.*conj(Em);%vector of backward traveling intensity
76 Itot=Etot.*conj(Etot); %vector of intensity (photon density) inside taper
77 Rad=0.5.*8.85e-12.*3e8.*nz.*Ate2v.*Itot;%vector of photon loss (radiation) from k
taper
78 ref=m21/m11;
79 Ref=ref*conj(ref)%reflectance from the taper (percentage of input light reflected)
80 %
81 %
82 subplot(2,1,1)
83 hold all
84 plot(ztmm,Itot),xlabel('ztmm'),ylabel('Itot')
85 subplot(2,1,2)
86 hold all
87 plot(ztmm,Rad),xlabel('ztmm'),ylabel('Rad')
88 end
89
90 %subplot(2,1,1), legend k
('480','490','500','510','520','530','540','550','560','570','580','590');
91 %subplot(2,1,2), legend k
('480','490','500','510','520','530','540','550','560','570','580','590');
92
93 subplot(2,1,1), legend k
('485','495','505','515','525','535','545','555','565','575','585');
94 subplot(2,1,2), legend k
('485','495','505','515','525','535','545','555','565','575','585');

```

This main MATLAB script calls upon other scripts to perform the simulation. The script names as well as brief descriptions of what each piece of code does, are commented in the scripts themselves, shown below:

```

1 %TiO2BraggInputs_mismatch.m
2
3 % An m-file that specifies the layer thicknesses, etc., of a slab Bragg
4 % waveguide with air core and TiO2/SiO2 claddings
5 dair=2e-6; %air-core thickness
6 dtiT=59e-9;%TiO2 layers thickness, set to be approx. quarter wave layer at 550 nm
wavelength
7 dtiB=60e-9;
8 doxT=90e-9; %SiO2 layers thickness, etc.
9 doxB=91.5e-9;
10 %kti=0; %extinction coefficient of TiO2 layers (set to zero because loss
neglected).
11 %kox=0; %extinction coefficient of SiO2 layers, etc.
12 zot=5; %number of periods in top Bragg mirror (if zot=5, works for 5.5p mirror,
etc.)
13 zob=6; %number of periods in bottom Bragg mirror

```

```

1 %TiO2BraggRadTE2_mismatch.m
2
3 % an m-file to plot the loss, GVD, etc. of a hollow slab bragg waveguide
4 % (with TiO2/SiO2 claddings) as
5 % a function of core thickness, at a single wavelength;
6 %
7 TiO2BraggInputs_mismatch; %a file that defines the layer thicknesses and number of
periods in each cladding mirror.
8 lambda0=lambda(qy);%lambda0=570e-9; %wavelength for the solution. Should lie in
the omnidirectional reflection band of the mirrors.
9 lam=lambda0;
10 mc=1;
11 %
12 %
13 qd=1;
14 daV(1)=2e-6; %starting core thickness at wide end of taper
15 dair=daV(1);
16 TiO2BraggModesVsAng_mismatch;
17     for qq=2:length(thetain)-1
18         if TcoreTE(qq)>TcoreTE(qq-1)
19             if TcoreTE(qq)>TcoreTE(qq+1)
20                 if TcoreTE(qq)>0.01
21                     modeang(mc)=thetain(qq);
22                     mc=mc+1;
23                 end
24             end
25         end
26     end
27     angM=modeang(2);
28     thetainC=[(angM-0.04):0.0001:(angM+0.04)];
29     TiO2BraggModeSolver_mismatch;
30     neffTEv(1)=neffTE;
31     Ate1v(1)=Ate1;
32     Ate2v(1)=Ate2;
33     clear modeang
34 %
35 lastang=RayangteV(1);
36 %
37 while neffTE>0.4;%at wide end of taper, relatively coarse step size in core height
is used, so that simulation time is not excessively long.
38     qd=qd+1;
39     daV(qd)=daV(qd-1)-0.01e-7;% you can play with this step size (smaller step
size will improve resolution but take longer to simulate)
40     dair=daV(qd);
41     if (lastang-0.1)>0
42         thetainC=[lastang-0.1:0.0001:lastang+0.1];

```

```

43     else
44         thetainC=[0:0.0001:lastang+0.1];
45     end
46     TiO2BraggModeSolver_mismatch;
47     neffTEv(qd)=neffTE;
48     Ate1v(qd)=Ate1;
49     Ate2v(qd)=Ate2;
50     lastang=RayangteV(1);
51     %qd
52 end
53 %
54 while neffTE>0.02;%reduced step size at small end of taper
55     qd=qd+1;
56     daV(qd)=daV(qd-1)-0.0005e-7;%you can also vary this step size, although it is
probably sufficiently small as is.
57     dair=daV(qd);
58     if (lastang-0.1)>0
59         thetainC=[lastang-0.1:0.0001:lastang+0.1];
60     else
61         thetainC=[0:0.0001:lastang+0.1];
62     end
63     %
64     TiO2BraggModeSolver_mismatch;
65     neffTEv(qd)=neffTE;
66     Ate1v(qd)=Ate1;
67     Ate2v(qd)=Ate2;
68     lastang=RayangteV(1);
69     %qd
70 end
71 %
72 daVf(1)=dair;
73 qdf=1;
74 while neffTE>0.0001;%very small step size used near cutoff point to properly
resolve rapidly varying fields in this region.
75     qdf=qdf+1;
76     daVf(qdf)=daVf(qdf-1)-0.00001e-7;
77     dair=daVf(qdf);
78     if (lastang-0.1)>0
79         thetainC=[lastang-0.1:0.0001:lastang+0.1];
80     else
81         thetainC=[0:0.0001:lastang+0.1];
82     end
83     %
84     TiO2BraggModeSolver_mismatch;
85     neffTEvf(qdf)=neffTE;
86     %if neffTE>1e-10;
87     %    QD=qd;
88     %end
89     Ate1vf(qdf)=Ate1;
90     Ate2vf(qdf)=Ate2;
91     lastang=RayangteV(1);
92     %qd
93 end
94 %
95 %
96 QD=qd+1;
97 %this file is modified to simulate the cutoff point with greater accuracy,
98 %by approximating that the waveguide has a fixed effective index and
99 %extinction coefficient beyond the cutoff point(assumed to be the value
100 %calculated at the cutoff point above.
101 QD2=QD+100;
102 neffTEv(QD)=neffTEvf(qdf-1);
103 Ate1v(QD)=Ate1vf(qdf-1);
104 Ate2v(QD)=Ate2vf(qdf-1);
105 daV(QD)=daV(qd)-qdf*0.00001e-7;
106 for qdz=QD:QD2
107     daV(qdz+1)=daV(qdz)-0.002e-7;
108 end

```

```

109 daVc=daV(1:QD2);
110 Ate1v(QD+1:QD2)=Ate1v(QD);
111 Ate2v(QD+1:QD2)=Ate2v(QD);
112 neffTEv(QD+1:QD2)=neffTEv(QD);
113 Ate1vdBcm=Ate1v*0.04343;
114 Ate2vdBcm=Ate2v*0.04343;
115 daVm=daVc*1e6;
116 % subplot(2,1,1)
117 % hold on
118 % plot(daVm,neffTEv)
119 % subplot(2,1,2)
120 % hold on
121 % plot(daVm,Ate1vdBcm,'g--',daVm,Ate2vdBcm,'r:')

```

```

1 %TiO2BraggModesVsAng_mismatch.m
2
3 % This m-file to calculate the reflectance and transmittance of a Fabry-Perot
4 % cavity clad by TiO2/SiO2 Bragg mirrors, versus incident angle.
5 % Note that this structure can also be viewed as a leaky Bragg waveguide.
6 %
7 %
8 % inputs
9 % lambda0=lam - wavelength provided by the file that calls this one.
10 % dair - hollow core thickness, provided by the file that calls this one.
11 % dti - thickness of TiO2 layers, provided ...
12 % dox - thickness of SiO2 layers, provided ...
13 % zot - number of periods in the top mirror, provided ...
14 % zob - number of periods in the bottom mirror, provided ...
15 %
16 %
17 imp=376.8; %impedance of free space
18 thetain=1.55:-0.00005:0.17; %vector of incident angles from normal to near-
glancing incidence (in radians)
19 thetainD=thetain*180/pi;
20 lambdanm=1e9*lambda0;
21 Ephoton=(6.626e-34*3e8/1.602e-19)./lambda0; %photon energy in eV
22 lambdam=1e6*lambda0;
23 %"fits" for refractive index of TiO2 and SiO2:
24 TiO2OpCon;%b;
25 ntiT=ntio2+0.11;%-i*ktio2;%0.02;% assumed higher than predicted by TiO2OpCon.m, as
per our measured results
26 ntiB=ntio2+0.02;
27 noxT=1.50;
28 noxB=1.46;
29 %
30 nsub=3.5;%5; %assume fixed index for a silicon substrate
31 %
32 for qt=1:length(thetain)
33     angin=thetain(qt);
34     % use Snell's law to calculate angle of propagation in each type of
35     % layer:
36     angOT=asin(sin(angin)/noxT);
37     angIT=asin(sin(angOT)*noxT/ntiT);
38
39     angOB=asin(sin(angin)/noxB);
40     angIB=asin(sin(angOB)*noxB/ntiB);
41
42     angS=asin(sin(angIB)*ntiB/nsub);
43
44     % calculate parameters that go into the Hecht T-matrices:
45     kohair=(2*pi/lam)*dair*cos(angin);
46     kohoT=(2*pi/lam)*noxT*doxT*cos(angOT);
47     kohiT=(2*pi/lam)*ntiT*dtiT*cos(angIT);
48     yote=cos(angin)/imp; %effective admittance of air, for TE, etc.

```

```

49     yotm=1/(cos(angin)*imp);
50     yoxteT=noxT*cos(angOT)/imp;
51     yoxtmT=noxT/(cos(angOT)*imp);
52     yiteT=ntiT*cos(angIT)/imp;
53     yitmT=ntiT/(cos(angIT)*imp);
54
55     yste=nsub*cos(angS)/imp;
56     ystm=nsub/(cos(angS)*imp);
57
58     kohair=(2*pi/lam)*dair*cos(angin);
59     kohoB=(2*pi/lam)*noxB*doxB*cos(angOB);
60     kohiB=(2*pi/lam)*ntiB*dtiB*cos(angIB);
61     yote=cos(angin)/imp; %effective admittance of air, for TE, etc.
62     yotm=1/(cos(angin)*imp);
63     yoxteB=noxB*cos(angOB)/imp;
64     yoxtmB=noxB/(cos(angOB)*imp);
65     yiteB=ntiB*cos(angIB)/imp;
66     yitmB=ntiB/(cos(angIB)*imp);
67
68     % Calculate transfer matrices for each type of layer:
69     % air 'core':
70     mairte=[cos(kohair) i*sin(kohair)/yote; i*yote*sin(kohair) cos(kohair)];
71     mairtm=[cos(kohair) i*sin(kohair)/yotm; i*yotm*sin(kohair) cos(kohair)];
72     % SiO2 layers:
73     moteT=[cos(kohoT) i*sin(kohoT)/yoxteT; i*yoxteT*sin(kohoT) cos(kohoT)];
74     motmT=[cos(kohoT) i*sin(kohoT)/yoxtmT; i*yoxtmT*sin(kohoT) cos(kohoT)];
75
76     moteB=[cos(kohoB) i*sin(kohoB)/yoxteB; i*yoxteB*sin(kohoB) cos(kohoB)];
77     motmB=[cos(kohoB) i*sin(kohoB)/yoxtmB; i*yoxtmB*sin(kohoB) cos(kohoB)];
78
79     % TiO2 layers:
80     miteT=[cos(kohiT) i*sin(kohiT)/yiteT; i*yiteT*sin(kohiT) cos(kohiT)];
81     mitmT=[cos(kohiT) i*sin(kohiT)/yitmT; i*yitmT*sin(kohiT) cos(kohiT)];
82
83     miteB=[cos(kohiB) i*sin(kohiB)/yiteB; i*yiteB*sin(kohiB) cos(kohiB)];
84     mitmB=[cos(kohiB) i*sin(kohiB)/yitmB; i*yitmB*sin(kohiB) cos(kohiB)];
85
86     % Calculate overall transfer matrix at current incident angle, for
87     % both TE and TM polarization:
88     mte=miteT*(moteT*miteT)^(zot)*mairte*(miteB*moteB)^zob*miteB;
89     mtm=mitmT*(motmT*mitmT)^(zot)*mairtm*(mitmB*motmB)^zob*mitmB;
90     %Calculate transfer matrices for bottom mirror alone:
91     mbmte=(miteB*moteB)^zob*miteB;
92     mbmtm=(mitmB*motmB)^zob*mitmB;
93     %Calculate transfer matrices for top mirror alone:
94     mtmte=miteT*(moteT*miteT)^(zot);
95     mtmtm=mitmT*(motmT*mitmT)^(zot);
96     % calculate reflection and transmission coefficients at
97     % current incident angle
98     rte=(yote*mte(1,1)+yote*yste*mte(1,2)-mte(2,1)-yste*mte(2,2))/(yote*mte(
99     (1,1)+yote*yste*mte(1,2)+mte(2,1)+yste*mte(2,2));
100     rbmte=(yote*mbmte(1,1)+yote*yste*mbmte(1,2)-mbmte(2,1)-yste*mbmte(2,2))/(
101     (yote*mbmte(1,1)+yote*yste*mbmte(1,2)+mbmte(2,1)+yste*mbmte(2,2));
102     rtm=(yotm*mtm(1,1)+yotm*ystm*mtm(1,2)-mtm(2,1)-ystm*mtm(2,2))/(yotm*mtm(
103     (1,1)+yotm*ystm*mtm(1,2)+mtm(2,1)+ystm*mtm(2,2));
104     rbmtm=(yotm*mbmtm(1,1)+yotm*ystm*mbmtm(1,2)-mbmtm(2,1)-ystm*mbmtm(2,2))/(
105     (yotm*mbmtm(1,1)+yotm*ystm*mbmtm(1,2)+mbmtm(2,1)+ystm*mbmtm(2,2));
106     tte=(2*yote)/(yote*mte(1,1)+yote*yste*mte(1,2)+mte(2,1)+yste*mte(2,2));
107     ttm=(2*yotm)/(yotm*mtm(1,1)+yotm*ystm*mtm(1,2)+mtm(2,1)+ystm*mtm(2,2));
108     tcoreTE=(1+rte)/(mtmte(1,1)*(1+rbmte*exp(-i*2*kohair))+mtmte(1,2)*yote*(1-
109     rbmte*exp(-i*2*kohair)));
110     tcoreTM=(1+rtm)/(mtmtm(1,1)*(1+rbmtm*exp(-i*2*kohair))+mtmtm(1,2)*yotm*(1-
111     rbmtm*exp(-i*2*kohair)));
112     % calculate reflectance and transmittance at current incident
113     % angle:
114     Rte(qt)=rte*conj(rte);
115     Rtm(qt)=rtm*conj(rtm);

```

```

110     Tte(qt)=tte*conj(tte)*nsub*cos(angS)/cos(angin);
111     Ttm(qt)=ttm*conj(ttm)*nsub*cos(angS)/cos(angin);
112     TcoreTE(qt)=tcoreTE*conj(tcoreTE);
113     TcoreTM(qt)=tcoreTM*conj(tcoreTM);
114 end
115 % Plot the reflectances and transmittances versus incidence angle
116 %subplot(4,1,1)
117 %hold on
118 %plot(thetainD,Rtm(:,1));
119 %subplot(4,1,2)
120 %hold on
121 %plot(thetainD,Ttm(:,1));
122 %subplot(2,1,1)
123 %hold on
124 %plot(thetainD,Rte);
125 %subplot(2,1,2)
126 %hold on
127 %plot(thetainD,Tte);

```

```

1 %TiO2BraggModeSolver_mismatch.m
2
3 % an m-file to calculate the response of a hollow slab waveguide with TiO2/
4 % SiO2 claddings to
5 % an external plane wave excitation, and thus to determine the propagation
6 % constants, etc. of the leaky guided modes.
7 % As provided, the file only calculates for TE polarized modes (the TM
8 % polarized modes have been 'commented' out using the % symbol).
9 %
10 %
11 % inputs
12 % lambda0 - vector of free-space wavelengths
13 % dair - hollow core thickness
14 % dox - thickness of the SiO2 layers
15 % dti - thickness of the TiO2 layers
16 % kti - extinction coefficient of TiO2 layers
17 % kox - extinction coefficient of SiO2 layers
18 % zot - number of periods in the top mirror
19 % zob - number of periods in the bottom mirror
20 %
21 %
22 imp=376.8; %impedance of free space
23 dcorecm=dair*1e2;
24 lambdanm=1e9*lambda0;
25 lamcm=lam*1e2;
26 Ephoton=(6.626e-34*3e8/1.602e-19)./lambda0; %photon energy in eV
27 lambdam=1e6*lambda0;
28 %
29 TiO2OpCon;%
30 nti=ntio2+0.11;%-i*kti2;%0.02;%based on measurements.
31 ntiB=ntio2+0.02;
32 noxT=1.50;
33 noxB=1.46;
34 %
35 % calculate a coarse approx. for the mode parameters
36 for qt=1:length(thetainC)
37     angin=thetainC(qt);
38     % use Snell's law to calculate angle of propagation in each type of
39     % layer:
40     angOT=asin(sin(angin)/noxT);
41     angIT=asin(sin(angOT)*noxT/ntiT);
42
43     angOB=asin(sin(angin)/noxB);
44     angIB=asin(sin(angOB)*noxB/ntiB);
45

```

```

44     angIB=asin(sin(angOB)*noxB/ntiB);
45
46     angS=asin(sin(angIB)*ntiB/nsub);
47
48     % calculate parameters that go into the Hecht T-matrices:
49     kohair=(2*pi/lam)*dair*cos(angin);
50     kohoT=(2*pi/lam)*noxT*doxT*cos(angOT);
51     kohiT=(2*pi/lam)*ntiT*dtiT*cos(angIT);
52     yote=cos(angin)/imp; %effective admittance of air, for TE, etc.
53     yotm=1/(cos(angin)*imp);
54     yoxteT=noxT*cos(angOT)/imp;
55     yoxtmT=noxT/(cos(angOT)*imp);
56     yiteT=ntiT*cos(angIT)/imp;
57     yitmT=ntiT/(cos(angIT)*imp);
58
59     yste=nsub*cos(angS)/imp;
60     ystm=nsub/(cos(angS)*imp);
61
62     kohair=(2*pi/lam)*dair*cos(angin);
63     kohoB=(2*pi/lam)*noxB*doxB*cos(angOB);
64     kohiB=(2*pi/lam)*ntiB*dtiB*cos(angIB);
65     yote=cos(angin)/imp; %effective admittance of air, for TE, etc.
66     yotm=1/(cos(angin)*imp);
67     yoxteB=noxB*cos(angOB)/imp;
68     yoxtmB=noxB/(cos(angOB)*imp);
69     yiteB=ntiB*cos(angIB)/imp;
70     yitmB=ntiB/(cos(angIB)*imp);
71
72     % Calculate transfer matrices for each type of layer:
73     % air 'core':
74     mairte=[cos(kohair) i*sin(kohair)/yote; i*yote*sin(kohair) cos(kohair)];
75     mairtm=[cos(kohair) i*sin(kohair)/yotm; i*yotm*sin(kohair) cos(kohair)];
76     % SiO2 layers:
77     moteT=[cos(kohoT) i*sin(kohoT)/yoxteT; i*yoxteT*sin(kohoT) cos(kohoT)];
78     motmT=[cos(kohoT) i*sin(kohoT)/yoxtmT; i*yoxtmT*sin(kohoT) cos(kohoT)];
79
80     moteB=[cos(kohoB) i*sin(kohoB)/yoxteB; i*yoxteB*sin(kohoB) cos(kohoB)];
81     motmB=[cos(kohoB) i*sin(kohoB)/yoxtmB; i*yoxtmB*sin(kohoB) cos(kohoB)];
82
83     % TiO2 layers:
84     miteT=[cos(kohiT) i*sin(kohiT)/yiteT; i*yiteT*sin(kohiT) cos(kohiT)];
85     mitmT=[cos(kohiT) i*sin(kohiT)/yitmT; i*yitmT*sin(kohiT) cos(kohiT)];
86
87     miteB=[cos(kohiB) i*sin(kohiB)/yiteB; i*yiteB*sin(kohiB) cos(kohiB)];
88     mitmB=[cos(kohiB) i*sin(kohiB)/yitmB; i*yitmB*sin(kohiB) cos(kohiB)];
89
90     % Calculate overall transfer matrix at current incident angle, for
91     % both TE and TM polarization:
92     mte=miteT*(moteT*miteT)^(zot)*mairte*(miteB*moteB)^zob*miteB;
93     mtm=mitmT*(motmT*mitmT)^(zot)*mairtm*(mitmB*motmB)^zob*mitmB;
94     %Calculate transfer matrices for bottom mirror alone:
95     mbmte=(miteB*moteB)^zob*miteB;
96     mbmtm=(mitmB*motmB)^zob*mitmB;
97     %Calculate transfer matrices for top mirror alone:
98     mtmte=miteT*(moteT*miteT)^(zot);
99     mtmtm=mitmT*(motmT*mitmT)^(zot);
100    % calculate reflection and transmission coefficients at
101    % current angle
102    rte=(yote*mte(1,1)+yote*yste*mte(1,2)-mte(2,1)-yste*mte(2,2))/(yote*mte(
103    1,1)+yote*yste*mte(1,2)+mte(2,1)+yste*mte(2,2));
104    rbtmte=(yote*mbmte(1,1)+yote*yste*mbmte(1,2)-mbmte(2,1)-yste*mbmte(2,2))/
105    (yote*mbmte(1,1)+yote*yste*mbmte(1,2)+mbmte(2,1)+yste*mbmte(2,2));
106    rbtmtm=(yotm*mtm(1,1)+yotm*ystm*mtm(1,2)-mtm(2,1)-ystm*mtm(2,2))/(yotm*mtm(
107    1,1)+yotm*ystm*mtm(1,2)+mtm(2,1)+ystm*mtm(2,2));
108    tte=(2*yote)/(yote*mte(1,1)+yote*yste*mte(1,2)+mte(2,1)+yste*mte(2,2));
109    ttm=(2*yotm)/(yotm*mtm(1,1)+yotm*ystm*mtm(1,2)+mtm(2,1)+ystm*mtm(2,2));

```

```

108     tcoreTE=(1+rte)/(mtmte(1,1)*(1+rbmte*exp(-i*2*kohair))+mtmte(1,2)*yote*(1-  
rbmte*exp(-i*2*kohair)));
109     tcoreTM=(1+rtm)/(mtmtm(1,1)*(1+rbmtm*exp(-i*2*kohair))+mtmtm(1,2)*yotm*(1-  
rbmtm*exp(-i*2*kohair)));
110     % calculate reflectance and transmittance at current incident
111     % angle:
112     RteC(qt)=rte*conj(rte);
113     RtmC(qt)=rtm*conj(rtm);
114     TteC(qt)=tte*conj(tte)*nsub*cos(angS)/cos(angin);
115     TtmC(qt)=ttm*conj(ttm)*nsub*cos(angS)/cos(angin);
116     TcoreTEC(qt)=tcoreTE*conj(tcoreTE);
117     TcoreTMC(qt)=tcoreTM*conj(tcoreTM);
118 end
119 [Rminte, Iminte]=min(RteC);
120 [Tcmaxte, Imaxte]=max(TcoreTEC);
121 [%Rmintm, Imintm]=min(Rtm);
122 [%Tcmaxtm, Imaxtm]=max(TcoreTM);
123 Tcte2=abs(TcoreTEC-Tcmaxte/2);
124 [TcLhalfte, ILhalfte]=min(Tcte2(1:Imaxte));
125 [TcUhalfte, IUhalfte]=min(Tcte2(Imaxte+1:length(thetainC)));
126 %Tctm2=abs(TcoreTM-Tcmaxtm/2);
127 [%TcLhalfm, ILhalfm]=min(Tctm2(1:Imaxtm));
128 [%TcUhalfm, IUhalfm]=min(Tctm2(Imaxtm+1:length(thetainC)));
129 RayangTEC=thetainC(Imaxte); %coarse estimate for TE bounce angle
130 %RayangTMC=thetainC(Imaxtm); %coarse estimate for TM bounce angle
131 %finestepTE=IUhalfte/10000000;
132 if Imaxte-2*IUhalfte>0
133     Ilow=Imaxte-2*IUhalfte;
134 else
135     Ilow=1;
136 end
137 thetaFL=thetainC(Ilow);
138 if Imaxte+2*IUhalfte<length(thetainC)
139     Ihigh=Imaxte+2*IUhalfte;
140 else
141     Ihigh=length(thetainC);
142 end
143 thetaFU=thetainC(Ihigh);
144 finestepTE=(thetaFU-thetaFL)/10000;
145 %finestepTM=IUhalfm/10000;
146 thetainFte=thetaFL:finestepTE:thetaFU;
147 thetainFteD=thetainFte*180/pi;
148 clear RteC;
149 clear TcoreTEC;
150 %Ate1=(2*pi/lam)*(sin(thetain(IUhalfte+Imaxte))-sin(thetain(ILhalfte)));
151 %Atm1=(2*pi/lam)*(sin(thetain(IUhalfm+Imaxtm))-sin(thetain(ILhalfm)));
152 %
153 % Calculate the mode properties with higher accuracy
154 for qf=1:length(thetainFte)
155     angin=thetainFte(qf);
156     % use Snell's law to calculate angle of propagaation in each type of
157     % layer:
158     angOT=asin(sin(angin)/noxT);
159     angIT=asin(sin(angOT)*noxT/ntiT);
160
161     angOB=asin(sin(angin)/noxB);
162     angIB=asin(sin(angOB)*noxB/ntiB);
163
164     angS=asin(sin(angIB)*ntiB/nsub);
165
166     % calculate parameters that go into the Hecht T-matrices:
167     kohair=(2*pi/lam)*dair*cos(angin);
168     kohoT=(2*pi/lam)*noxT*doxT*cos(angOT);
169     kohiT=(2*pi/lam)*ntiT*dtiT*cos(angIT);
170     yote=cos(angin)/imp; %effective admittance of air, for TE, etc.
171     yotm=1/(cos(angin)*imp);
172     yoxteT=noxT*cos(angOT)/imp;
173     yoxtmT=noxT/(cos(angOT)*imp);

```

```

174     yiteT=ntiT*cos(angIT)/imp;
175     yitmT=ntiT/(cos(angIT)*imp);
176
177     yste=nsub*cos(angS)/imp;
178     ystm=nsub/(cos(angS)*imp);
179
180     kohair=(2*pi/lam)*dair*cos(angin);
181     kohoB=(2*pi/lam)*noxB*doxB*cos(angOB);
182     kohiB=(2*pi/lam)*ntiB*dtiB*cos(angIB);
183     yote=cos(angin)/imp; %effective admittance of air, for TE, etc.
184     yotm=1/(cos(angin)*imp);
185     yoxteB=noxB*cos(angOB)/imp;
186     yoxtmB=noxB/(cos(angOB)*imp);
187     yiteB=ntiB*cos(angIB)/imp;
188     yitmB=ntiB/(cos(angIB)*imp);
189
190     % Calculate transfer matrices for each type of layer:
191     % air 'core':
192     mairte=[cos(kohair) i*sin(kohair)/yote; i*yote*sin(kohair) cos(kohair)];
193     mairtm=[cos(kohair) i*sin(kohair)/yotm; i*yotm*sin(kohair) cos(kohair)];
194     % SiO2 layers:
195     moteT=[cos(kohoT) i*sin(kohoT)/yoxteT; i*yoxteT*sin(kohoT) cos(kohoT)];
196     motmT=[cos(kohoT) i*sin(kohoT)/yoxtmT; i*yoxtmT*sin(kohoT) cos(kohoT)];
197
198     moteB=[cos(kohoB) i*sin(kohoB)/yoxteB; i*yoxteB*sin(kohoB) cos(kohoB)];
199     motmB=[cos(kohoB) i*sin(kohoB)/yoxtmB; i*yoxtmB*sin(kohoB) cos(kohoB)];
200
201     % TiO2 layers:
202     miteT=[cos(kohiT) i*sin(kohiT)/yiteT; i*yiteT*sin(kohiT) cos(kohiT)];
203     mitmT=[cos(kohiT) i*sin(kohiT)/yitmT; i*yitmT*sin(kohiT) cos(kohiT)];
204
205     miteB=[cos(kohiB) i*sin(kohiB)/yiteB; i*yiteB*sin(kohiB) cos(kohiB)];
206     mitmB=[cos(kohiB) i*sin(kohiB)/yitmB; i*yitmB*sin(kohiB) cos(kohiB)];
207
208     % Calculate overall transfer matrix at current incident angle, for
209     % both TE and TM polarization:
210     mte=miteT*(moteT*miteT)^(zot)*mairte*(miteB*moteB)^zob*miteB;
211     mtm=mitmT*(motmT*mitmT)^(zot)*mairtm*(mitmB*motmB)^zob*mitmB;
212     %Calculate transfer matrices for bottom mirror alone:
213     mbmte=(miteB*moteB)^zob*miteB;
214     mbmtm=(mitmB*motmB)^zob*mitmB;
215     %Calculate transfer matrices for top mirror alone:
216     mtmte=miteT*(moteT*miteT)^(zot);
217     mtmtm=mitmT*(motmT*mitmT)^(zot);
218     % calculate reflection and transmission coefficients at
219     % current angle
220     rte=(yote*mte(1,1)+yote*yste*mte(1,2)-mte(2,1)-yste*mte(2,2))/(yote*mte(
221     (1,1)+yote*yste*mte(1,2)+mte(2,1)+yste*mte(2,2));
222     rbmte=(yote*mbmte(1,1)+yote*yste*mbmte(1,2)-mbmte(2,1)-yste*mbmte(2,2))/κ
223     (yote*mbmte(1,1)+yote*yste*mbmte(1,2)+mbmte(2,1)+yste*mbmte(2,2));
224     rtm=(yotm*mtm(1,1)+yotm*ystm*mtm(1,2)-mtm(2,1)-ystm*mtm(2,2))/(yotm*mtm(
225     (1,1)+yotm*ystm*mtm(1,2)+mtm(2,1)+ystm*mtm(2,2));
226     rbmtm=(yotm*mbmtm(1,1)+yotm*ystm*mbmtm(1,2)-mbmtm(2,1)-ystm*mbmtm(2,2))/κ
227     (yotm*mbmtm(1,1)+yotm*ystm*mbmtm(1,2)+mbmtm(2,1)+ystm*mbmtm(2,2));
228     tte=(2*yote)/(yote*mte(1,1)+yote*yste*mte(1,2)+mte(2,1)+yste*mte(2,2));
229     ttm=(2*yotm)/(yotm*mtm(1,1)+yotm*ystm*mtm(1,2)+mtm(2,1)+ystm*mtm(2,2));
230     tcoreTE=(1+rte)/(mtmte(1,1)*(1+rbmte*exp(-i*2*kohair))+mtmte(1,2)*yote*(1-κ
231     rbmte*exp(-i*2*kohair)));
232     tcoreTM=(1+rtm)/(mtmtm(1,1)*(1+rbmtm*exp(-i*2*kohair))+mtmtm(1,2)*yotm*(1-κ
233     rbmtm*exp(-i*2*kohair)));
234     % calculate reflectance and transmittance at current incident
235     % angle:
236     RteF(qf)=rte*conj(rte);
237     RtmF(qf)=rtm*conj(rtm);
238     TteF(qf)=tte*conj(tte)*nsub*cos(angS)/cos(angin);
239     TtmF(qf)=ttm*conj(ttm)*nsub*cos(angS)/cos(angin);
240     TcoreTEF(qf)=tcoreTE*conj(tcoreTE);
241     TcoreTMF(qf)=tcoreTM*conj(tcoreTM);

```

```

236 end
237 [Rminte, Iminfte]=min(RteF);
238 [Tcmaxte, Imaxfte]=max(TcoreTEF);
239 [Rmintm, Imintm]=min(Rtm);
240 [%Tcmaxtm, Imaxtm]=max(TcoreTM);
241 Tcte2=abs(TcoreTEF-Tcmaxte/2);
242 [TcLhalfte, ILhalfte]=min(Tcte2(1:Imaxfte));
243 [TcUhalfte, IUhalfte]=min(Tcte2(Imaxfte+1:length(thetainFte)));
244 %Tctm2=abs(TcoreTM-Tcmaxtm/2);
245 [%TcLhalfm, ILhalfm]=min(Tctm2(1:Imaxtm));
246 [%TcUhalfm, IUhalfm]=min(Tctm2(Imaxtm+1:length(thetain)));
247 Ate1=(2*pi/lam)*(sin(thetainFte(IUhalfte+Imaxfte))-sin(thetainFte(ILhalfte)));
248 if IUhalfte<2*Imaxfte
249     Ate1=(2*pi/lam)*(sin(thetainFte(IUhalfte+Imaxfte))-sin(thetainFte(ILhalfte)));
250 else
251     Ate1=(4*pi/lam)*(sin(thetainFte(IUhalfte+Imaxfte))-sin(thetainFte(Imaxfte)));
252 end
253 %Atm1=(2*pi/lam)*(sin(thetain(IUhalfm+Imaxtm))-sin(thetain(ILhalfm)));
254 RayangteV=[thetainFte(Imaxfte) thetainFte(Imaxfte)+0.00001];
255 %RayangtmV=[thetain(Imaxtm) thetain(Imaxtm)+0.00001];
256 for qr=1:2
257     %lam=lambda0(q1); %current free space wavelength
258     Ravanqte=RavanqteV(qr);
259     % Rayangtm=RayangtmV(qr);
260     %angin=acos(lam/(2*dcore)); %approximate bounce angle based on lambda/2*
transverse wavelength condition.
261
262     angOteT=asin(sin(Rayangte)/noxT);
263 %     angOtmT=asin(sin(Rayangtm)/noxT);
264     angOteB=asin(sin(Rayangte)/noxB);
265 %     angOtmB=asin(sin(Rayangtm)/noxB);
266
267     angIteT=asin(sin(Rayangte)/ntiT);
268 %     angItmT=asin(sin(Rayangtm)/nsiT);
269     angIteB=asin(sin(Rayangte)/ntiB);
270 %     angItmB=asin(sin(Rayangtm)/nsiB);
271
272     angSte=asin(sin(Rayangte)/nsub);
273 %     angStm=asin(sin(Rayangtm)/nsub);
274
275     kohoteT=(2*pi/lam)*noxT*doxT*cos(angOteT);
276 %     kohotmT=(2*pi/lam)*noxT*doxT*cos(angOtmT);
277     kohiteT=(2*pi/lam)*ntiT*dtiT*cos(angIteT);
278 %     kohitmT=(2*pi/lam)*ntiT*dtiT*cos(angItmT);
279     yote=cos(Rayangte)/imp;
280 %     yotm=1/(cos(Rayangtm)*imp);
281     yoxteT=noxT*cos(angOteT)/imp;
282 %     yoxtmT=noxT/(cos(angOtmT)*imp);
283     yiteT=ntiT*cos(angIteT)/imp;
284 %     yitmT=ntiT/(cos(angItmT)*imp);
285
286     kohoteB=(2*pi/lam)*noxB*doxB*cos(angOteB);
287 %     kohotmB=(2*pi/lam)*noxB*doxB*cos(angOtmB);
288     kohiteB=(2*pi/lam)*ntiB*dtiB*cos(angIteB);
289 %     kohitmB=(2*pi/lam)*ntiB*dtiB*cos(angItmB);
290     yote=cos(Rayangte)/imp;
291 %     yotm=1/(cos(Rayangtm)*imp);
292     yoxteB=noxB*cos(angOteB)/imp;
293 %     yoxtmB=noxB/(cos(angOtmB)*imp);
294     yiteB=ntiB*cos(angIteB)/imp;
295 %     yitmB=ntiB/(cos(angItmB)*imp);
296
297     yste=nsub*cos(angSte)/imp;
298 %     ystm=nsub/(cos(angStm)*imp);
299
300     moteT=[cos(kohoteT) i*sin(kohoteT)/yoxteT; i*yoxteT*sin(kohoteT) cos*
(kohoteT)];

```

```

301 %      motmT=[cos(kohotmT) i*sin(kohotmT)/yoxtmT; i*yoxtmT*sin(kohotmT) cosκ
(kohotmT)];
302      miteT=[cos(kohiteT) i*sin(kohiteT)/yiteT; i*yiteT*sin(kohiteT) cosκ
(kohiteT)];
303 %      mitmT=[cos(kohitmT) i*sin(kohitmT)/yitmT; i*yitmT*sin(kohitmT) cosκ
(kohitmT)];
304
305      moteB=[cos(kohoteB) i*sin(kohoteB)/yoxteB; i*yoxteB*sin(kohoteB) cosκ
(kohoteB)];
306 %      motmB=[cos(kohotmB) i*sin(kohotmB)/yoxtmB; i*yoxtmB*sin(kohotmB) cosκ
(kohotmB)];
307      miteB=[cos(kohiteB) i*sin(kohiteB)/yiteB; i*yiteB*sin(kohiteB) cosκ
(kohiteB)];
308 %      mitmB=[cos(kohitmB) i*sin(kohitmB)/yitmB; i*yitmB*sin(kohitmB) cosκ
(kohitmB)];
309
310
311      mbte=(miteB*moteB)^zob*miteB;
312      mtte=(miteT*moteT)^(zot)*miteT;
313 %      mbtm=(mitmB*motmB)^zob;
314 %      mttm=(motmT*mitmT)^(zot);
315 %
316 %      calculate reflection and transmission coefficients at
317 %      current wavelength, for each top and bottom mirror
318      rtte(qr)=(yote*mtte(1,1)+yote*yote*mtte(1,2)-mtte(2,1)-yote*mtte(2,2))/κ
(yote*mtte(1,1)+yote*yote*mtte(1,2)+mtte(2,1)+yote*mtte(2,2));
319      rbte(qr)=(yote*mbte(1,1)+yote*yote*mbte(1,2)-mbte(2,1)-yote*mbte(2,2))/κ
(yote*mbte(1,1)+yote*yote*mbte(1,2)+mbte(2,1)+yote*mbte(2,2));
320 %      rttm(qr)=(yotm*mttm(1,1)+yotm*yotm*mttm(1,2)-mttm(2,1)-yotm*mttm(2,2))/κ
(yotm*mttm(1,1)+yotm*yotm*mttm(1,2)+mttm(2,1)+yotm*mttm(2,2));
321 %      rbtm(qr)=(yotm*mbtm(1,1)+yotm*yotm*mbtm(1,2)-mbtm(2,1)-yotm*mbtm(2,2))/κ
(yotm*mbtm(1,1)+yotm*yotm*mbtm(1,2)+mbtm(2,1)+yotm*mbtm(2,2));
322      Rtte(qr)=rtte(qr)*conj(rtte(qr));
323      angRtte(qr)=angle(Rtte(qr));
324      Rbte(qr)=rbte(qr)*conj(rbte(qr));
325      angRbte(qr)=angle(Rbte(qr));
326 %      Rttm(qr)=rttm(qr)*conj(rttm(qr));
327 %      angRttm(qr)=angle(Rttm(qr));
328 %      Rbtm(qr)=rbtm(qr)*conj(rbtm(qr));
329 %      angRbtm(qr)=angle(Rbtm(qr));
330 end
331      dpennte=-(lam/(4*pi))*(angRtte(2)-angRtte(1))/(cos(RayangteV(2))-cosκ
(RayangteV(1)));
332      dpenbte=-(lam/(4*pi))*(angRbte(2)-angRbte(1))/(cos(RayangteV(2))-cosκ
(RayangteV(1)));
333 %      dpenttm=-(lam/(4*pi))*(angRttm(2)-angRttm(1))/(cos(RayangtmV(2))-cosκ
(RayangtmV(1)));
334 %      dpenbtm=-(lam/(4*pi))*(angRbtm(2)-angRbtm(1))/(cos(RayangtmV(2))-cosκ
(RayangtmV(1)));
335      deffte=dair+dpente+dpenbte;
336 %      defftm=dair+dpenttm+dpenbtm;
337 %      Ate=(2.5*lamcm/dcorecm^2)*log10(Rtte(1)*Rbte(1));
338      Ate2=-log(Rtte(1)*Rbte(1))/(2*deffte*tan(RayangteV(1)));
339      neffTE=sin(RayangteV(1));
340      BetaTE1=(2*pi/lam)*neffTE-i*Ate1/2;
341      BetaTE2=(2*pi/lam)*neffTE-i*Ate2/2;
342      %BetaTE2=(2*pi/lam)*neffTE+i*(100*Ate(ql)/(2*4.343));
343      k0=2*pi/lam;
344      ktranTE1=sqrt(k0^2-BetaTE1^2);
345      ktranTE2=sqrt(k0^2-BetaTE2^2);
346      CheckModete1=rtte(1)*rbte(1)*exp(-i*2*ktranTE1*dair);
347      CheckModete2=rtte(1)*rbte(1)*exp(-i*2*ktranTE2*dair);
348      %CheckModete=(4*pi/lam)*cos(Rayangte)*dair+angRbte+angRtte;
349 %      Atm=(2.5*lamcm/dcorecm^2)*log10(Rttm(1)*Rbtm(1));
350 %      Atm2=-log(Rttm(1)*Rbtm(1))/(2*defftm*tan(RayangtmV(1)));
351 %      neffTM=sin(RayangtmV(1));
352 %      BetaTM1=(2*pi/lam)*neffTM-i*Atm1/2;
353 %      BetaTM2=(2*pi/lam)*neffTM-i*Atm2/2;

```

```

354 %BetaTM2=(2*pi/lam)*neffTM+i*(100*Atm(ql)/(2*4.343));
355 % ktranTM1=sqrt(k0^2-BetaTM1^2);
356 % ktranTM2=sqrt(k0^2-BetaTM2^2);
357 % CheckModetm1=rctm(1)*rbtm(1)*exp(-i*2*ktranTM1*dair);
358 % CheckModetm2=rctm(1)*rbtm(1)*exp(-i*2*ktranTM2*dair);
359 %CheckModetm=(4*pi/lam)*cos(Rayangtm)*dair+angRbtm+angRttm;
360 %end
361 %Rtte
362 %Rbte
363 %angRtte
364 %angRbte
365 %Ate1
366 %Ate2
367 %Atm1
368 %Atm2
369 %
370 %subplot(2,1,1)
371 %hold on
372 %plot(thetainD,Rtm(:,1));
373 %
374 %subplot(2,1,2)
375 %hold on
376 %plot(thetainD,Rte(:,1));
377 %subplot(2,1,1)
378 %hold on
379 %plot(thetainFteD,Rte);
380 %subplot(2,1,1)
381 %hold on
382 %plot(thetainFteD,TcoreTE);
383 clear RteF
384 clear TcoreTEF

```

```

1 %TiO2OpCon.m
2
3 % m-file that encodes a closed-form expression for the optical constants of
4 % e-beam evaporated TiO2 in the visible to near IR region, per the
5 % Forouhi-Bloomer model of S.Y. Kim (Appl. Opt. 35, 6703, 1996).
6 %
7 %Inputs
8 %lambda0 - vector of free-space wavelengths
9 %
10 % Fitting parameters
11 At=0.7737; % unitless
12 Bt=7.9401; % eV
13 Ct=16.444; % eV^2
14 Egt=3.3137; % eV
15 ninf=2.191; % unitless
16 % lambda0=550*1e-9
17
18 hvV=6.626e-34.*3e8./(lambda0.*1.602e-19); %vector of photon energy in eV
19 lambdaNM=lambda0*1e9;
20 %
21 ktio2=At.*(hvV-Egt).^2./(hvV.^2-Bt.*hvV+Ct); %only valid for lambda0<360 nm
22 %
23 Btp=At.*(-Bt.^2+2.*Egt.*Bt-2.*Egt.^2+2.*Ct)./(4.*Ct-Bt.^2).^0.5;
24 Ctp=At.*(Bt.*(Egt.^2+Ct)-4.*Egt.*Ct)./(4.*Ct-Bt.^2).^0.5;
25 %
26 ntio2=ninf+(Btp.*hvV+Ctp)./(hvV.^2-Bt.*hvV+Ct);
27 %
28 %plot(lambdaNM,ntio2)

```

Appendix B: Electron beam evaporator procedure

The following is the deposition procedure used for the 6-pocket electron beam evaporation system housed in CCIS:

To vent system:

- Check that cryopump temp is less than 12 K idle, 14 K running (Regenerate if above 20-25 K).
- Make sure cryopump gate valve closed, scroll pump off, roughing valve closed.
- Open vent switch to vent. Wait until sound dies down.
- Before opening bell jar, break seal. Turn power to hoist on. Start at 20% speed, then full speed. Steady bell jar when raising.

Loading the system:

- When loading system, work top down. Chamber & chamber tools are glove clean.
- Use grounding wand to ground hearth, filament, anode, cathode, etc.
- Check xtal monitors for life. Might replace if at 87% or less. May change each time for oxide films.
- Clean hearth & crucibles if necessary. (Further instructions in *Unloading the system* section).
- Mount substrate onto holder in laminar flow hood. Briefly clean with N₂ gun.
- Screw in substrate holder, insert thermocouple. Water cooler may be attached to side.
- Make sure shutter positioned correctly.
- Refill target liners if necessary, insert into pockets and label.
- Wipe down metal where O-ring meets. Lower bell jar at 100%, then 20% for last part. Position windows facing forward.

Pumping down:

- Make sure vent switch closed. Turn scroll pump on, then wait 30 sec. Open roughing valve fully (upwards of 10 min to see pressure on TC controller).
- Pump to 100-300 mTorr. Close roughing valve and turn off scroll pump.

- Open gate valve slowly. When belljar pressure starts dropping, stop. Let pressure drop slowly to 1 mTorr, then fully open gate valve.
- After a few min, turn on ion gauge by pressing “ion”. Once below 5×10^{-5} Torr, press “Degas” (takes ~25 min) to degas ion gauge. May want to degas 2x. Ion gauge must cool to read properly.
- Pump down for ~4 hours or overnight until in 10^{-7} readings. 1.2×10^{-6} highest acceptable base press.

Deposition (requires 2 people):

- Water cooling: open return (top) then supply (bottom) valves for belljar, e-gun, 2 xtal monitors:
 __ | | | | __
- For oxide films, 1×10^{-5} Torr (ion gauge), no more than 5×10^{-5} Torr O_2 needed, tank at “5”.
- Flip voltage and control breakers up. Turn power key, then turn on main power. Wait 30 sec.
- Press “reset” to reset interlocks. All lights should be on.
- Turn high voltage on (wait 10 min before turning on source 1)
- Zero xtal monitors. Right monitor main monitor, left backup.
- Turn on e-beam sweep controller. Turn DC on. Set X,Y offset at 0,0. Sweep settings may be adjusted.

(Sample settings for SiO_2 : 1.2 sweep ampl., spiral, 0 phase, fast, profile 1).

- Check monitors & settings: Verify film density, z-factor, 100% tooling for films. For STC-2000A press “start” to activate next film.
- Turn filament control to 0. Press “on” (under source 1 panel).
 - Change X,Y offset until beam centered.
 - If “cutback” flashes, turn down filament a little.
 - Make sure pressure never above 1×10^{-5} Torr.
 - For Cu, adjust filament control until blue/sparks. Wait for dep. rate to incr. Melts all at once.
 - For SiO_2 , turn spiral sweep on. Slowly increase filament current until rate reached.
- Once dep. rate stabilized, open shutter & zero xtal monitors. Close shutter when thickness reached.

- Decrease filament current to 0 (quickly for SiO₂, slowly for copper). Turn filament off.

After Deposition:

- Turn sweep off. Turn Dc off. Turn off sweep control.
- Turn off high voltage. Wait 5 min, then turn main power off.
- Turn key, pull out, put on top of X,Y. Flip down high voltage and control breakers.
- Close O₂ tank. Close cryopump.
- Let system cool to near room temp. or overnight.

Removing the sample:

- Water cooling: close supply (bottom) then return (top) valves.
- Turn off ion gauge. Then close gate valve (snap!).
- Open vent valve, wait until sound stops. Tip bell jar to break seal.
- Slowly raise bell jar. Use grounding wand.
- Start at bottom of system, work your way up.
- Remove sources. Use Allan key to remove holder. Place holder in laminar flow hood.
- Use dremel with steel brush (use goggles, gloves, and mask) to abrade hearth & pockets. Dremel not glove clean. Don't push too hard. Use scotch-brite afterwards.
- Use handheld vacuum to remove particles. Then use 40 psi N₂ gas to remove particles from cracks, near filament, feed through, anode, cathode, etc.
- Wipe down abraded area with acetone, then methanol. Final N₂ blowout.
- Change xtals if failed/bad. Can use Al or Ag coated (instead of Au).
- Wipe sealing surface, lower bell jar until chains slack.
- Turn off vent valve. Turn off joist. Turn on scroll pump. Wait 10 sec, open roughing valve fast.
- Pump to 500 mTorr, close roughing valve, turn off scroll pump. (Empty system held at rough vacuum).

Appendix C: Sputter System Procedure

The following is a customised procedure for reactively sputtering films with Sputtering System #2 (Doug) in the nanoFAB:

Opening and loading an empty system:

- Press “emis” on multi gauge controller to turn off the ion gauge then press “channel” until TC1 is shown and nothing on the bottom right.
- Close the Baratron valve, then close the cryo gate valve. Make sure the cryo temperature is below 20K before proceeding.
- Flip up the chamber vent switch, close when 7.6×10^2 Torr is reached (1 atm).
- Press the button on the hoist to lift top of chamber and swing top away when substrate holder is high enough.
- Use gloves for inside of chamber; chamber is glove clean.
- N₂ gun, then load desired targets. Gun 3 is prone to mechanically damaging fragile Si targets. Switch power supply cables to guns as necessary (cable 3 for built-in pulsed supply, ext. cable for external pulsed supply, cable 1 & 2 for DC supplies 1 & 2).
- Check inside of chamber for flaking and debris; vacuum if required.
- If glass view port is coated with metal, pull out and replace with fully IPA-cleaned glass slides.
- Make sure dark space shield is spaced properly. Keep out of notches for ¼” thick targets and in shallowest notch for 1/8” targets. Verify an open circuit between target & shield using voltmeter.
- Test and close the shutters.
- MARK SUBSTRATE(S) WITH SHARPIE, then load.
- If system will be heated, replace mount ring with cryo heat shield ring.
- Lower the top of the chamber.

Pump down:

- Open chamber roughing valve one full turn and rough until 3.5×10^2 Torr is reached, then open roughing valve all the way. Rough until **3.0×10^{-1} Torr** is reached, then close the roughing valve.
- Open the cryo gate valve.

- Open the Baratron valve.
- Press “**channel**” on the multi gauge controller until BA1 is shown in the lower right of the display, then press “**emis**” to turn on ion gauge.
- If heating, turn on heater 5 minutes into cryo pumpdown. It will take at least 90 minutes for system to reach 2×10^{-6} Torr.

Deposition setup:

- Press “**emis**” on the multi gauge to turn off ion gauge filament, then press “**channel**” until aux1 (Baratron gauge) is shown in the lower section of the display.
- If display on the gas control panel is dark press any button to activate it. Press “**ON 1**” to activate Ar (50 sccm). If using O₂, set flow rate but do not turn on yet.
- Close the cryo gate valve about 3.75 turns to reach 7.0×10^{-3} Torr.
- If using pulsed power supply, set parameters. Verify correct cables are connected to guns. If using external pulsed supply, plug in power, gun cable, and interlock cable. Flip breaker on back & set parameters.
- If using power supply 1 or 2, flip up the appropriate light switch & set parameters.
- Turn on substrate rotation using switch on right side, to “3”.

Deposition:

- Press “**on**” or “**start**” on power supply and ramp/burn-in for specified time. In last 1 or 2 minutes of burn-in (if voltage stable), change pressure to specified deposition pressure & turn on O₂ by pressing “**ON 3**” if using it.
- Open shutter for specified deposition time, then close.
- If ramping down, change power set point to 0. Otherwise, press “**off**” or “**stop**” on power supply.
- If O₂ is on, turn off by pressing “**OFF 3**”. Change pressure to 7.0×10^{-3} Torr.
- If depositing SiO₂/Si multilayer, Ti getter during SiO₂ ramp-down and during Si ramp-up. Make sure O₂ is off while gettering. Turn off Ti getter before lowering pressure for Si deposition.
- Ext. power supply ramp-down does not work, so use for Si (instead of for SiO₂).

After last layer:

- Turn off heater. Turn off substrate rotation.
- Turn off Ar flow. Zero O₂ flow setpoint.
- Zero pulsed power supply settings, return ramp-time to 20s.
- Open cryo gate valve all the way and pump for 5 minutes.
- Close the Baratron valve.
- Close the cryo gate valve.
- Flip up chamber vent switch for a split second, letting in a few Torr of N₂. Wait 5 minutes.
- Flip chamber vent switch and vent to atm. pressure. Hoist top of chamber & swing away.

Removing the sample & targets:

- Put on gloves.
- Use cleanroom wipe to remove hot dark space shield. Remove targets, N₂ gun, and inspect before placing into storage container. Place target ring and shield back onto gun.
- Carefully remove (hot) substrate(s). If cryo heat shield was used, replace with normal substrate mount ring.
- Check chamber for particulates, test shutters, double-check for parts not placed back in system.
- Lower the top of the chamber & rough to 3×10^{-1} Torr, with valve fully open immediately.
- Close roughing valve.
- Open cryo gate valve.
- Open Baratron valve.
- Press “**channel**” on the multi gauge controller until BA1 (ion gauge) is shown in the lower right of the display, then press “**emis**”.
- Record parameters in logbook & log out.